5-2013

HYDRAULIC PROPERTIES OF VARIABLY-SATURATED POROUS MEDIA DETERMINED USING QUANTITATIVE NEUTRON RADIOGRAPHY

Misun Kang
University of Tennessee - Knoxville, mkang9@utk.edu

To the Graduate Council:

I am submitting herewith a dissertation written by Misun Kang entitled "HYDRAULIC PROPERTIES OF VARIABLY-SATURATED POROUS MEDIA DETERMINED USING QUANTITATIVE NEUTRON RADIOGRAPHY." I have examined the final electronic copy of this dissertation for form and content and recommend that it be accepted in partial fulfillment of the requirements for the degree of Doctor of Philosophy, with a major in Geology.

Edmund Perfect, Major Professor

We have read this dissertation and recommend its acceptance:

Larry D. McKay, Hassina Bilheux, Jaehoon Lee

Accepted for the Council:

Carolyn R. Hodges

Vice Provost and Dean of the Graduate School

(Original signatures are on file with official student records.)

HYDRAULIC PROPERTIES OF VARIABLY-SATURATED POROUS MEDIA DETERMINED USING QUANTITATIVE NEUTRON RADIOGRAPHY

A Dissertation Presented for the

Doctor of Philosophy

Degree

The University of Tennessee, Knoxville

Misun Kang

May 2013

ACKNOWLEDGEMENTS

This research project would not have been possible without the support of many people. I would like to express my profound gratitude and regards to my advisor Dr. Ed Perfect for his timely guidance, help and constant encouragement throughout the course of my graduate studies. I also wish to express a deep gratitude to Dr. Hassina Bilheux for her kind guidance, financial support, and for teaching me the principles of neutron imaging, which enabled me to complete this dissertation. I would also like to thank my other committee members Dr. Larry McKay and Dr. Jaehoon Lee for their invaluable lessons and support along the way. I have gained valuable knowledge from their teachings and guidance. I am also obliged to other members of the Laboratory Directed Research and Development (LDRD) project, Juske Horita, Chu-Lin Cheng, Sophie Voisin, and Jeff Warren for sharing their knowledge and for their cooperation over the course of this project. I would also like to thank Dan Hussey at National Institute of Standards and Technology (NIST) for valuable suggestions in the project and Keely Willis for her contributions made at an early stage of the image analyses. I am also thankful for contributions from the High Flux Isotope Reactor (HFIR) support groups, the Instrument Development Group, and the HFIR Machine Shop, Brent Taylor for making sample holders, Jaimie Werner for assistance in the chemistry lab, and Lakeisha Walker for beam line assistance. I am thankful for the financial support of the Laboratory Directed Research and Development (LDRD) Program of Oak Ridge National Laboratory and the Joint Directed Research and Development (JDRD) Program of the University of Tennessee UT-ORNL Science Alliance. Special thanks to the National Institute of Standards and Technology and Oak Ridge National Laboratory for providing the neutron research facilities. Lastly, I wish to express my love and gratitude to my family and friends for their constant encouragement and love throughout the duration of my studies.

ABSTRACT

The theoretical understanding of fluids in unsaturated porous media has improved substantially over the last several decades. Water retention curves remain a central pillar in the theoretical framework for modeling of water flow in unsaturated porous media. Use of the average water retention function in models to simulate water flow in porous media can result in inaccurate predictions due to the variations in water content and matric potential with elevation within the medium. As a result, point water retention curve data are needed for testing existing numerical and analytical models and for improving our ability to predict unsaturated water flow. Traditionally point water retention functions have been derived from average water retention curve data. The main objective of this research was to directly measure point water retention functions using neutron imaging. Neutron imaging provides a non-destructive tool for visualizing water flow in porous media due to its high sensitivity to hydrogen, and relative insensitivity to mineral solids. Using neutron imaging techniques I have explored the following research topics: (1) quantitative measurements of the equilibrium water content distribution in porous media, (2) measurement of average and point water retention functions using neutron radiography, (3) assessment of analytical models relating average and point water retention curves, and (4) investigation of the dynamics of unsaturated water flow.

In the first two chapters of this dissertation I developed quantitative neutron imaging techniques to measure the 2-dimensional distribution of water in porous media and obtain the average water retention function for Flint sand by neutron radiography. In chapter III, point water retention functions were directly measured by neutron radiography and the resulting point functions were parameterized using the Brooks & Corey equation. The point water retention function constructed from the median values of the fitted Brooks and Corey parameters corresponded closely with the point curve for Flint sand obtained by inverse modeling of the average water retention curve data. In the final chapter of this dissertation we investigated capillary uptake of water in Berea Sandstone and estimated the sorptivity and unsaturated diffusivity function from analyses of the neutron radiographs.

TABLE OF CONTENTS

LIST OF TABLES

CHAPTER III

CHAPTER IV

CHAPTER V

LIST OF FIGURES

CHAPTER I

CHAPTER II

CHAPTER III

CHAPTER IV

CHAPTER V

MAIN APPENDIX

CHAPTER I
INTRODUCTION

Overview

Water movement in partially-saturated porous media has received considerable attention from the agricultural, environmental, and oil industry sectors focused on crop production, remediation of subsurface contamination, carbon sequestration, and oil recovery. In the vadose zone, soil water content and soil water potential govern many subsurface processes such as gas (air, CO_2), water, and solute movements, runoff, infiltration, and plant root water uptake. The relationship between soil water content and soil water potential is represented as a soil water retention curve. A number of equations have been developed to describe laboratory and field water retention curve data. The most popular water retention functions are those developed by Brooks and Corey (1964) and van Genuchten (1980). These water retention functions were coupled with the pore-size distribution models of Burdine (1953) or Mualem (1976) to predict water flow in the unsaturated zone. Hydraulic conductivity is much less under unsaturated conditions than under saturated conditions. Due to the dependency of the unsaturated hydraulic conductivity on water content, modeling of water flow in the vadose zone needs information on the water retention curve. Obtaining accurate parameters describing the water retention function is very important for predicting water flow in variably-saturated porous media.

Neutron imaging has been developed as a non-destructive tool for many applications due to its transparency to heavy elements and high sensitivity to light elements (Anderson et al., 2009; Strobl et al., 2009). Because neutrons interact with the nucleus of the atom rather than the electron cloud, the interaction forces between neutrons and nuclei are not correlated with the atomic number of the element and also depend on a particular isotope of the element. Neutron imaging is a particularly powerful tool with respect to soil water due to its high contrast between H and SiO_2, and high spatial and temporal resolutions. The first paper on neutron imaging of water in soil was a feasibility study conducted in two dimensions by Lewis and Krinitzsky (1976). Since then neutron imaging has been employed to study both the statics and dynamics of soil water, either in two dimensions (radiography) or three dimensions (tomography), mostly using thermal neutrons. Lopes et al. (1999) first applied neutron tomography to observe

differences in soil compaction, and the static distribution of water inside compacted soil. Neutron tomography has also been applied to visualize and quantify of the static distribution of water in glass beads (Lehmann et al. 2006) and sand (Tumlinson et al., 2008). More recently, neutron radiography has been used to study the static water distribution of a partially-saturated sand column (Kim et al., 2012).

Neutron imaging has also been applied to study the dynamics of water flows in soil. Clarke et al. (1987) visualized the movement of water and development of ice lenses in frozen soil using neutron radiography combined with a psychrometer and thermocouples. Tullis (1994) used neutron radiography to study unstable finger flow in layered soil (fine over coarse sand) and later Hincapié and Germann (2010) investigated finger flow during gravity driven infiltration in unsaturated sand boxes. Neutron radiography has also been used for studies of water infiltration in homogeneous sand (Deinert et al., 2004) and soil aggregates (Carminati et al., 2009). The pore scale three dimensional spatial water distribution at quasi-steady state was visualized and quantified using neutron tomography with artificial heterogeneous sand columns (Kaestner et al .,2007; Schaap et al., 2008; Papafotiou et al., 2008; Vasin, 2008) and natural heterogeneous mine soils (Badorreck et al., 2010).

Quantitative Neutron Imaging Techniques

Quantification of water in samples using gray scale images, which depend on the transmitted neutron intensity, was enabled after the development of digital image detector systems (Lehmann et al, 2004a). Recently neutron imaging has been used for quantitative analysis in many applications such as fuel cells (Heller et al., 2009), roots of plants (Oswald et al., 2008), and water in porous media (Tumlinson et al., 2008). For neutron imaging, considerable effort must be made to achieve a parallel and uniform beam, with limited background scattering sources, using variable collimators providing balance between the neutron flux and image resolution. The spatial resolution achieved can be quantified in terms of the geometric unsharpness ($U_g = l / (L / D)$), where l is the distance between the sample and the detector, D is the aperture diameter, and L is

the distance between the aperture and the detector (Fig. 1-1). The geometric unsharpness increases as the sample-to- detector distance increases and as the L/D ratio decreases.

However, the polychromatic neutron beam at a neutron imaging beamline is not only non-uniform but also unstable over time in the sample area. As a result, it is almost impossible to assign some energy-dependent range values to each pixel of the transmitted sample image. Moreover, Lehmann et al (2004b) and Hassanein et al. (2005) observed the nonlinearity of the relationship between the attenuated beam intensity and the thickness of the water. This deviation occurs mainly due to beam hardening and increased neutron scattering. Beam hardening occurs if the neutron beam is polychromatic; low energy neutrons are attenuated more readily than higher energy neutrons, which results in differential attenuation. Scattering is most problematic for large water thicknesses and small detector distances. The deviation increases as the water content of the sample increases and as the sample to detector distance decreases, resulting in underestimation of the water content for thick samples with high water contents placed close to the detector.

Different approaches have been proposed to remove these effects. One is to restrict measurements to very thin sections of water (Lehmann et al., 2004b; Hussey et al., 2010; Kim et al., 2012). Another approach is to correct for scattering effects using Monte Carlo modeling of point scattered functions (Hassanein et al., 2005). However, modeling does not provide a universal fix and experimental determination of other scattering components needs to be further investigated (Hassanein et al., 2006). As an alternative, an empirical water thickness calibration equation can be developed for a specific instrumentation configuration (Tumlinson et al., 2008, Hussey and Jacobson, 2012). In chapter II, we investigate scattering effects according to the distance between the sample and detector and introduce an empirical calibration method to correct these effects to accurately quantify water content in unsaturated sand columns at the HFIR CG-1D beamline.

Average and Point Water Retention Functions

Traditionally average water retention functions have been measured due to the limitations of “black box” experimental methods such as the hanging water column and pressure plate setups (Dane and Hopmans, 2002). However, use of the average water retention function in models to simulate water flow in porous media can result in inaccurate predictions due to the variations in water content and matric potential with elevation within the medium at quasi-static equilibrium, especially for coarse porous media and tall column experiments (Dane et al., 1992). To improve the prediction of the hydraulic properties in unsaturated porous media, computational procedures have been developed to inversely estimate the point retention function from the measured average water retention function (Liu and Dane, 1995a; Schroth et al., 1996; Peters and Durner, 2006; Cropper et al., 2011). TrueCell (Jalbert et al., 1999), a Windows interface based on Liu and Dane’s (1995b) FORTRAN program, is available to extract point functions using the Brooks and Corey (1964) equation from measured average water retention curve data.

Direct measurements of point water retention data are needed for testing existing numerical and analytical models and for improving our ability to predict water flow in unsaturated porous media (Sakaki and Illangasekare, 2007). Neutron imaging offers the possibility of visualizing the distribution of water in porous media and determining both the average and point water retention functions. In Chapter III, average soil water retention curves are measured by thermal neutron radiography at BT-2, NIST. The resulting average functions are parameterized using the van Genuchten equation (van Genuchten, 1980). The parameters are then compared with those from hanging water column data independently measured in the laboratory. In chapter IV, point water retention functions are directly measured by neutron radiography and the resulting point functions are parameterized using the Brooks and Corey equation (Brooks and Corey, 1964). The point Brooks-Corey parameters are then compared with those obtained inversely using TrueCell (Jalbert et al., 1999) applied to average water retention data. The HYDRUS 1-D numerical model (Šimůnek, 1998) is also used to compare the predicted and observed cumulative outflows.

Unsaturated Water Flow Dynamics

Over the past 25 years, neutron imaging has been applied to visualize the dynamics of water imbibition in both natural and engineered materials, including soil (Carminati and Flühler, 2009), rock (Cnudde et al., 2008), brick (El Abd et al. 2009), and concrete (de Beer et al., 2005). The sorptivity and unsaturated diffusivity function are important for describing transient water movement under partially-saturated conditions. These parameters are well established in soil physics for quantifying the movement of a capillary wetting front into partially-saturated soil (Philip, 1957; Bruce and Klute, 1956). They can also be used in the geology and petroleum engineering fields (oil and gas industry) to evaluate wettability of rock cores and in studies of spontaneous imbibitions (Handy, 1960; Standnes, 2004). In chapter V, the dynamics of capillary uptake of water in Berea Sandstone are investigated and the sorptivity and diffusivity function determined by analysis of neutron radiographic images.

References

Anderson, I.S., R. McGreevy, and H. Bilheux. 2009. Neutron Imaging and Applications: A Reference for the Imaging Community. Springer, New York.

Badorreck, A., H.H. Gerke, and P. Vontobel. 2010. Noninvasive observations of flow patterns in locally heterogeneous mine soils using neutron radiation. Vadose Zone J. 9:362–372. doi:10.2136/vzj2009.0100

Brooks, R.H. and A.T. Corey. 1964. Hydraulic properties of porous media. Hydrol. Pap.#3., Colorado State Univ., Fort Collins, CO.

Bruce, R. R. and A. Klute, 1956. The measurement of soil moisture diffusivity. Soil Sci. Soc. Amer. Proc. 20:458-462. doi:10.2136/sssaj1956.03615995002000040004x

Burdine, N.T. 1953. Relative permeability calculations from pore-size distribution data. Petr Trans, Am Inst Mining Metall Eng, 198: 71–77.

Carminati , A., and H. Flühler. 2009. Water infiltration and redistribution in soil aggregate packings. Vadose Zone J. 8:150–157. doi:10.2136/vzj2008.0077

Clarke M. A., Kettle R. J., D'Souza. 1987. Developments in the use of thermal neutron radiography for studying mass transfer in a partially frozen soil. Proceedings of the Second World Conference on Neutron Radiography, Paris, France, June 16–20, 1986, Barton, G.Farny, J. Person, H.RÖttger, D. Reidel, eds. Pub. Co., Dordrecht, Holland 1987. pp. 271–279.

Cnudde, V., M. Dierick, J. Vlassenbroeck, B. Masschaele, E. Lehmann, P. Jacob, L. Van Hoorebeke. 2008. High-speed neutron radiography for monitoring the water absorption by capillarity in porous materials. Nucl. Instrum. Methods Phys. Res., Sect. B. 266: 155–163.

Cropper, S.C., E. Perfect, E.H. van den Berg, and M.A. Mayes. 2011. Comparison of average and point capillary pressure-saturation functions determined by steady-state centrifugation. Soil Sci. Soc. Am. J. 75:17-25

Dane, J.H., and J.W. Hopmans. 2002. Hanging water column, in Methods of Soil Analysis, part 4, Physical Methods, edited by J. H. Dane and G. C. Topp, pp. 680–683, Soil Science Society of America, Madison, Wis.

Dane, J.H., M. Oostrom, and B.C. Missildine. 1992. An improved method for the determination of capillary pressure-saturation curves involving TCE, water and air, Journal of Contaminant Hydrology, 11: 69–81.

de Beer, F. C., le Roux, J. J., and Kearsley, E. P. 2005. Testing the durability of concrete with neutron radiography. Nucl. Instr. Meth. Phys. Res. A 542: 226-231.

Deinert, M.R., J.-Y. Parlange, T. Steenhuis, J. Throop, K. Ünlü, and K.B. Cady. 2004. Measurement of fluid contents and wetting front profiles by real-time neutron radiography, Journal of Hydrology, 290: 192-201.

El Abd, A. Czachor, A., and Milczarek, J. 2009. Neutron radiography determination of water diffusivity in fired clay brick. Appl. Radiation Isotopes. 47: 556-559

Handy, L.L., 1960. Determination of effective capillary pressures for porous media from imbibition data. Petrol. Trans. AIME 219: 75-80.

Hassanein, R., E. Lehmann, and P. Vontobel. 2005. Methods of scattering corrections for quantitative neutron radiography. Nuclear instruments and methods in physics research section A. 542: 353-360.

Hassanein, R., F. de Beer, N. Kardjilov, and E. Lehmann. 2006. Scattering correction algorithm for neutron radiography and tomography tested at facilities with different beam characteristics. Physica B, 385-386 (2): 1194-1196.

Heller, A.K., L. Shi, J.S. Brenizer, and M.M Mench. 2009. Initial water quantification results using neutron computed tomography, Nuclear Instruments and Methods in Physics Research A, 605 (1-2): 99-102.

Hincapié, I. and P. Germann. 2010. Water content wave approach applied to neutron radiographs of finger flow. Vadose Zone Journal, 9(2): 278-284.

Hussey, D.S., D.L. Jacobson, K.J. Coakley, D.F. Vecchia and M. Arif. 2010. In situ fuel cell water metrology at the NIST-NCNR neutron imaging facility. Journal of Fuel Cell Science and Technology, 7(2): 22-22.

Hussey D.S., D.L. Jacobson, "Neutron radiography for PEMFCs: High resolution studies", in: C. Hartnig, C. Roth (Eds.) Polymer electrolyte membrane and direct methanol fuel cell technology, Vol. 2 in situ characterization of PEMFCs and DMFCs, Woodhead, Cambridge, U.K., 2012.

Jalbert, M., J.H. Dane, and J.H. Liu. 1999. TrueCell: Physical point Brooks–Corey parameters using pressure cell data. Users guide for version 1.2. Spec.Rep. Dep. of Agron. and Soils, Auburn Univ., Auburn, AL.

Kaestner A, Hassanein R, Vontobel P, Lehmann P, Schaap J, Lehmann E, 2006. Mapping the 3D water dynamics in heterogeneous sands using thermal neutrons. Chem. Eng. J. doi:10.1016/j.cej.06.013

Kim F., D. Penumadu, and D.S. Hussey. 2012. Water distribution variation in partially saturated granular materials using neutron imaging. J. Geotech. Geoenviron. Eng. 138(2), 147-154, doi: 10.1061/ (ASCE) GT.1943-5606.0000583

Lehmann E.H., P. Vontobel, G. Frei, and C. Bronnimann. 2004a. Neutron imaging — Detector options and practical results. Nucl. Instrum. Meth. A 531: 228–237.

Lehmann E.H., P. Vontobel and N. Kardjilov. 2004b. Hydrogen distribution measurements by neutrons Appl. Radiat. Isotopes, 61: 503-509.

Lehmann P., Wyss P., Flisch A., Lehmann E., Vontobel P., Krafczyk M., 2006. Tomographical imaging and mathematical description of porous media used for the prediction of fluid distribution. Vadose Zone J; 5:80–97.

Lewis, J.T. and Krinitzsky, E.E., 1976. Neutron radiation in the study of soil and rock, Berger, H., Editor, "Practical Applications of Neutron Radiography and Gaging," ASTM STP 586, American Society for Testing and Materials, West Conshohocken, PA, 1976., pp. 241-251

Liu, H.H., and J.H. Dane. 1995a. Improved computational procedure for retention relations of immiscible fluids using pressure cells. Soil Sci. Soc. Am. J. 59:1520–1524.

Liu, H.H., and J.H. Dane. 1995b. Computation of the Brooks–Corey parameters at a physical point based on pressure cell data. Spec. Rep. Dep. of Agron.and Soils, Auburn Univ., Auburn, AL.

Lopes, R.T., Bessa, A.P., Braz, D., de Jesus, E.F.O., 1999. Neutron computerized tomography in compacted soil. Appl. Radiat. Isot. 50: 451–458.

Mualem, Y. 1976. A new model for predicting the hydraulic conductivity of unsaturated porous media. Water Resour Res, 12: 513–522.

Oswald, S.E., M. Menon, A. Carminati, P. Vontobel, E. Lehmann, and R. Schulin. 2008. Quantitative imaging of infiltration, root growth, and root water uptake via neutron radiography. Vadose Zone Journal. 7(3): 1035-1047.

Papafotiou A., Helmig R., Schaap J., Lehmann P., Kaestner A., Flühler H. 2008. From the pore scale to the lab scale: 3D lab experiment and numerical simulation of drainage in heterogeneous porous media. Adv Water Resour 31: 1253-1268

Peters, A., and W. Durner. 2006. Improved estimation of soil water retention characteristics from hydrostatic column experiments. Water Resour. Res. 42:W11401, doi:10.1029/2006WR004952.

Philip, J. R. 1957. The theory of infiltration: 4. Sorptivity and algebraic infiltration equations. Soil Sci. 84: 257-264

Sakaki, T., and T. H. Illangasekare. 2007. Comparison of height-averaged and point-measured capillary pressure – saturation relations for sands using a modified Tempe cell, Water Resour. Res., 43, W12502, doi: 10.1029/2006WR005814.

Schaap J, Lehmann P, Frei G, Vontobel P, Kaestner A, Hassanein R. 2008. Measuring the effect of structure on water dynamics in heterogeneous porous media using fast neutron tomography. Adv Water Resour 31(9): 1233–41.

Schroth, M.H., S.J. Ahearn, J.S. Selker, and J.D. Istok. 1996. Characterization of Miller-similar silica sands for laboratory hydrologic studies. Soil Sci. Soc. Am. J. 60:1331–1339

Šimůnek, J., K. Huang, M. Šejna, and M. Th. van Genuchten, The Hydrus-1D software package for simulating the one-dimensional movement of water, heat, and multiple solutes in variably-saturated media. Version 1.0, IGWMC - TPS - 70, International Ground Water Modeling Center, Colorado School of Mines, Golden, Colorado, 186 pp., 1998.

Standnes, D.C. 2004. Analysis of oil recovery rates for spontaneous imbibition of aqueous solutions into preferential oil-wet carbonates by estimation of capillary diffusivity coefficients. Colloids and Surfaces A 251: 93-101.

Strobl, M., A. Hilger, N. Kardjilov, O. Ebrahimi, S. Keil, and I. Manke. 2009. Differential phase contrast and dark field neutron imaging. ITMNR 08 - Proceedings of the sixth Topical Meeting on Neutron Radiography, 605(1-2): 9-12.

Tullis, B.P., J.T. Lindsay, and S.J. Wright. 1994. The imaging of wetting front instabilities in porous media using neutron radioscopy. Nondestructive Testing and Evaluation 11: 97-106

Tumlinson, L.G., H. Liu, W.K. Silk, and J.W. Hopmans. 2008. Thermal neutron computed tomography of soil water and plant roots. Soil Science Society of America Journal. 72: 1234-1242.

van Genuchten, M. T. 1980. A closed form equation for predicting the hydraulic conductivity of unsaturated soils. Soil Science Society of America Journal, 44: 892-898.

Vasin, M., P. Lehmann, A. Kaestner, R. Hassanein, W. Nowak, R. Helmig, and I. Neuweiler. 2008. Drainage in heterogeneous sand columns with diff erent geometric structures. Adv. Water Resour. 31: 1205–1220. doi:10.1016/j. advwatres.2008.01.004

Appendix A

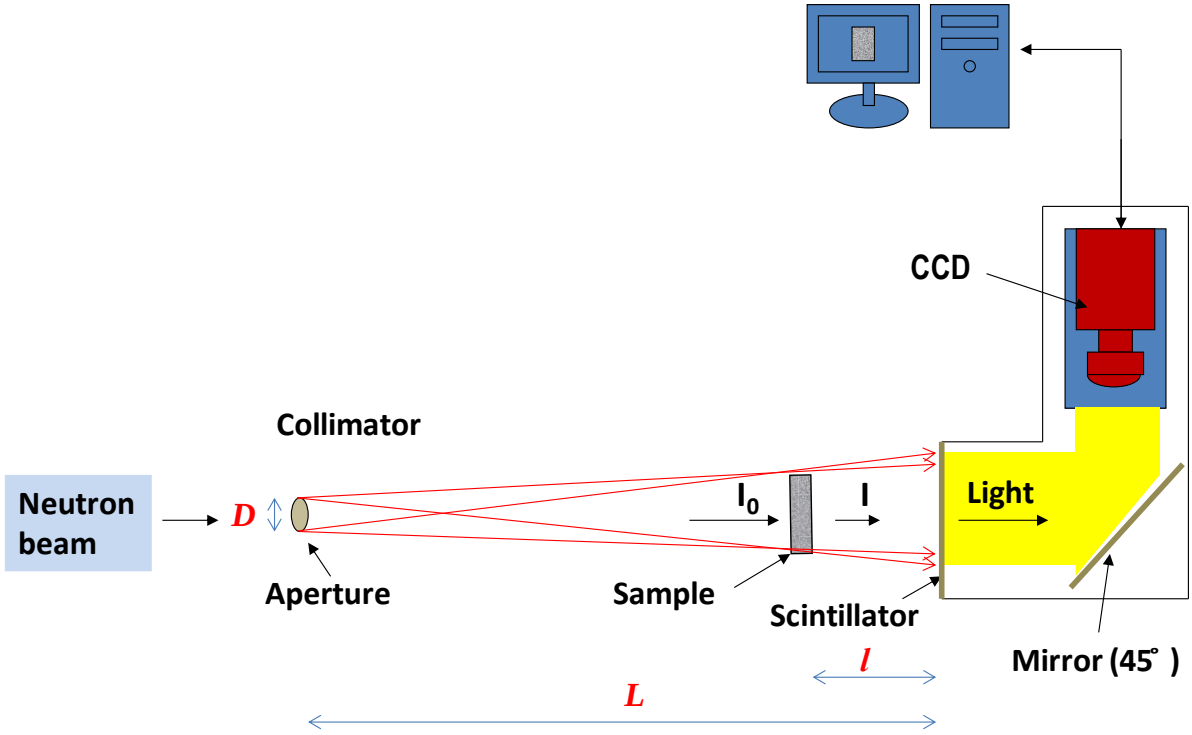

Figure 1- 1 Layout of a neutron imaging to achieve a parallel and uniform beam, with limited background scattering sources, using a collimator providing balance between the neutron flux and image resolution.

CHAPTER II

WATER CALIBRATION MEASUREMENTS FOR NEUTRON RADIOGRAPHY: APPLICATION TO WATER CONTENT QUANTIFICATION IN POROUS MEDIA

This chapter is a reformatted version of a paper originally published in Nuclear Instruments and Methods in Physics Research Section A in 2013 by Kang et al. Misun Kang participated in the experiments, performed data analyses, and wrote the paper. Other co-authors contributed to the data acquisition, data analyses, and revision of the manuscript.

Kang M., H.Z. Bilheux, S. Voisin, C.L. Cheng, E. Perfect, J. Horita, and J.M. Warren,2013. Water calibration measurements for neutron radiography: application to water content quantification in porous media. Nucl. Instr. Meth. Phys. Res. A. DOI: 10.1016/j.nima.2012.12.112.

Abstract

Using neutron radiography, the measurement of water thickness was performed using aluminum (Al) water calibration cells at the High Flux Isotope Reactor (HFIR) Cold-Guide (CG) 1D neutron imaging facility at Oak Ridge National Laboratory, Oak Ridge, TN, USA. Calibration of water thickness is an important step to accurately measure water contents in samples of interest. Neutron attenuation by water does not vary linearly with thickness mainly due to beam hardening and scattering effects. Transmission measurements for known water thicknesses in water calibration cells allow proper correction of the underestimation of water content due to these effects.

As anticipated, strong scattering effects were observed for water thicknesses greater than 0.2 cm when the water calibration cells were positioned close to the face of the detector / scintillator (0 and 2.4 cm away, respectively). The water calibration cells were also positioned 24 cm away from the detector face. These measurements resulted in less scattering and this position (designated as the sample position) was used for the subsequent experimental determination of the neutron attenuation coefficient for water.

Neutron radiographic images of moist Flint sand in rectangular and cylindrical containers acquired at the sample position were used to demonstrate the applicability of the water calibration. Cumulative changes in the water volumes within the sand columns

during monotonic drainage determined by neutron radiography were compared with those recorded by direct reading from a burette connected to a hanging water column. In general, the neutron radiography data showed very good agreement with those obtained volumetrically using the hanging water-column method. These results allow extension of the calibration equation to the quantification of unknown water contents within other samples of porous media.

1. Introduction

Neutron imaging is a complementary technique to X-ray imaging and is used in many applications in various fields such as materials science, physics, biology, geology, and archaeology (Strobl et al., 2009; Anderson et al., 2009). Neutrons interact with atomic nuclei and this interaction does not show periodic regularity with the atomic number. Neutrons are particularly sensitive to light elements such as hydrogen (H), lithium (Li), and boron (B), while being relatively insensitive to metals such as Al (Strobl et al., 2009; Anderson et al., 2009). Thus, neutrons are well suited for the investigation of water movement in natural and engineered porous media. X-rays and magnetic resonance imaging (MRI) have also been used in the past to study water in porous media (Bayer et al., 2004; Basavaraj and Gupta, 2004; Oswald et al, 1997). X-ray imaging uses tracers to enhance contrast since X-rays are not as sensitive to light elements, such as H, as neutrons (Basavaraj and Gupta, 2004). The quantitative study of water in porous media using MRI is limited by the range of pore sizes that can be imaged and the presence of paramagnetic elements in the sample (Hall et al., 1997). Quantitative measurements of water thickness using neutron imaging have been used in a variety of research areas, such as fuel cells (Turhan et al., 2006; Trabold et al., 2009), plant roots (Oswald et al, 2008; Moradi et al., 2009), and rocks and soils (Cnudde et al., 2008; Tumlinson et al., 2008; Hincapié and Germann, 2009 and 2010; Cheng et al., 2012). Transmission of a polychromatic neutron beam through a heterogeneous sample is given by:

$$I = \int I_0\,(\mathrm{E})\,\exp[\,-\textstyle\sum_{i=1}^{n}\left(\tau_i\,\Sigma_i(E)\right)\,]\,dE \qquad [1]$$

where I and I_0 are the transmitted and incident beam intensity, respectively, τ_i is the thickness of each element i, and $\Sigma_i(E) = \frac{\sigma_i(E) m \rho N_A}{M}$, where $\sigma_i(E)$ is the total cross section of an element (barns), m is the number of moles of an element in a molecule, ρ is the density (g/cm^3), N_A is Avogadro's number (6.022×10^{23} mol^{-1}), and M is the

molecular weight (g/mol) of the sample over the range of the effective neutron energy spectrum.

Experimental determination of water thickness in a sample requires careful measurement of the attenuation coefficient of the sample container (if any) and other parts of the sample that do not contain water. The effects of the container and other materials can be experimentally removed by dividing the image of the sample containing water (called the “wet” sample in this publication) by the image of the dry sample in the same container (called the “dry” sample in this publication):

$$I_w / I_d = \int \exp[\, -\tau_w \, \Sigma_w(E) \,]\, dE \qquad [2]$$

where I_w is the transmitted intensity of the “wet” sample, I_d is the transmitted intensity of the “dry” sample, τ_w is the water thickness, and $\Sigma_w(E)$ is the attenuation coefficient of water. In polychromatic beam measurements, only the average value of $\Sigma_w(E)$ can be obtained rather than its value at different wavelengths. Wavelength-discrete $\Sigma_w(E)$ values can be achieved by neutron monochromatization using a double-crystal monochromator device (Treimer et al., 2006) or a velocity selector/ chopper system (Kardjilov et al., 2003 and 2004) for continuous sources.

For neutron imaging, considerable effort must be made to achieve a parallel and uniform beam, with limited background scattering sources, using variable collimators providing balance between the neutron flux and image resolution. The spatial resolution achieved can be quantified in terms of the geometric unsharpness (U_g):

$$U_g = l \,/\, (L \,/\, D) \qquad [3]$$

where l is the distance between the sample and the detector, D is the aperture diameter, and L is the distance between the aperture and the detector. The geometric

unsharpness increases as the sample-to- detector distance increases and as the L/D ratio decreases.

Optimization of the sample position in relation to the detector (scintillator) position has proven to be critical for water thickness measurements of samples (Lehmann et al., 2004; Hassanein et al., 2005; Kardjilov et al., 2005). The relationship between the attenuated beam intensity and water thickness is not linear and this non-linearity increases as the water content of the sample increases and/or as the distance between sample and detector decreases, resulting in the underestimation of water content in thick samples with high water contents. Lehmann et al. (2004) observed deviations from the exponential law, Eq. [2], for water thicknesses greater than 0.2 cm even at a 15 cm sample to detector distance. The non-linearity is due to beam hardening and neutron scattering effects. Beam hardening occurs if the neutron beam is polychromatic; low energy neutrons are more attenuated than high energy neutrons, which results in variations in the measured attenuation. The scattering effects can be more problematic for water because the attenuation occurs due to incoherent scattering. The scattered neutrons can reach the detector and result in the increase of the transmission, which leads to a less water content estimation in the sample.

Different approaches have been proposed to quantify water content in samples using polychromatic neutron imaging. One is to restrict measurements to sections of the sample with a total water thickness less than 0.1 or 0.2 cm (Hussey et al., 2010; Kim et al., 2011) in order to minimize beam hardening and scattering effects. Another approach is to correct these effects using the point scattered functions based on Monte Carlo simulations after considering the sample and the experimental set-up (i.e. energy spectrum, detector type, distance between sample and detector) (Hassanein et al., 2005). The latter correction does not provide a universal solution as it relies on a specific experimental set-up (Hassanein et al., 2006). As an alternative, an empirical water thickness calibration equation can be developed for a specific instrumentation configuration (Tumlinson et al., 2008; Hussey et al., 2012).

The specific objectives of this research were to: 1) investigate scattering effects at different calibration sample locations (i.e. varying distance between the sample and

detector); 2) obtain water attenuation coefficients for the High Flux Isotope Reactor (HFIR) Cold Guide (CG) 1D neutron imaging facility using water calibration cells positioned at the optimal sample location for a sample with high water content; and 3) apply this calibration equation to quantify water content within a partially-saturated porous medium and compare the results with conventional hanging water column experiments.

2. Methodology

The HFIR CG-1D Neutron Prototype Imaging Instrument

Neutron radiography of water calibration cells and Flint sand were performed at the HFIR CG-1D neutron imaging facility at the Oak Ridge National Laboratory (ORNL). For polychromatic neutron imaging, apertures with variable diameter sizes (pinhole geometry) can be used at the entrance of the He-filled flight path with a maximum L of 5.5 m. For this experiment, D and L are equal to 8 mm and 5 m respectively, resulting in a L/D of 625. A higher L/D ratio, i.e. smaller apertures and longer aperture to detector distances, reduces blur in an image and limits background scattering sources. The spectrum measured using a micro-channel plate (MCP) detector (Tremsin et al., 2005) with a flight path of approximately 5.5 m is shown in Fig. 2-1[1]. The facility provides most neutrons between approximately 0.8 and 6 Å (with a peak at ~ 2.6 Å) (Bilheux et al., 2012). The detector set-up is equipped with a 25 µm thick LiF/ZnS scintillator and DW936 IkonL ANDOR^{TM} charge coupled device (CCD) camera system. In order to reduce dark current, the CCD camera is equipped with a Peltier cooling system and is routinely cooled down to -60°C. For these measurements, the neutron flux is 5×10^5 $cm^{-2}s^{-1}$, the field of view is approximately 7 cm × 7 cm, and the full width at half maximum (FWHM) at 24 cm is 212 µm. As indicated in Eq. 2, the attenuation of

[1] Note: All tables and figures are located in Appendix B.

neutrons by water is neutron-energy dependent. Reported attenuation coefficients for ≤ 0.2 cm thick water layers are 6.45 cm^{-1} for cold neutrons and 3.38 cm^{-1} for thermal neutrons (Arif et al., 2009). Since cold neutrons are more sensitive to the H atoms in water than thermal neutrons, the neutron sensitivity is greater for thinner water thicknesses at the HFIR CG-1D beamline.

Calibration Cells

One cylindrical and two different rectangular aluminum (Al) calibration cell types (#1 and #2) were used to obtain water attenuation coefficients at the HFIR CG-1D. The engineering accuracy of the calibration cells was $\pm$ 0.01 mm. All of the cells were cleaned with detergent and rinsed with deionized water before use.

The #1 rectangular type cell had a cross-section of 1.9 cm × 10.5 cm, with a 0.01 cm thickness step increment. Radiographic images of the wet (i.e. filled with deionized water) and dry (i.e. no water) cell were measured using for water thickness ranging from 0.005 – 0.205 cm, 0.2 – 0.6 cm, 0.6 − 1 cm at two different sample positions: 2.4 and 24 cm away from the detector with 600 s exposure time.

For replication, another series of measurements was performed with a #2 rectangular cell type. The dimensions of the cell were 6 cm × 4.2 cm, with incremental thickness steps of 0.005 cm for less than 0.15 cm water thickness measurement, and incremental thickness steps of 0.01 cm for above 0.15 cm water thickness measurement. The wet and dry cells were imaged for the 0.005 − 0.05 cm, 0.105 – 0.15 cm, 0.2 – 0.3 cm, and 0.41 – 0.5 cm water thickness ranges. All of these measurements were made at two different sample positions: against the detector (0 cm) and 24 cm away from the detector with 300 s exposure time.

The cylindrical water calibration cell with an inner diameter of 0.909 cm was also imaged at a distance of 24 cm from the detector with 60 s and 120 s exposure time. For the cylindrical cell geometry, the known water thickness of the cell is equivalent to the chord length of a circle (C_{ij}):

$$C_{ij} = 2\sqrt{r^2 - a_{(i,j)}^2} \quad [4]$$

where r is the radius of the cylindrical cell (cm) and $a_{(i,j)}$ is the distance from the center of the cell to the pixel (i,j) (cm). Since most neutron radiographic images of our porous media samples were acquired using a cylindrical Al chamber, any effects on the attenuation and scattering of neutrons due to the geometry of the sample are of particular interest.

Image Analysis

All image processing and quantitative analyses were performed using the MATLAB (Version 7.11, R2010b-SP1, MathWorks, Inc., 2011) and ImageJ (Version 1.43m, National Institutes of Health, 2009) software packages. The measured transmitted neutron intensity in the sample depends on the incident neutron beam intensity and the detector efficiency at detecting and converting neutrons. Each pixel value of the image ranged from ~ 900 (CCD default offset) to 65,535 according to the transmitted neutron intensity. Background scattering coming from the beamline equipment has been measured to be less than 1% and thus can be ignored during the image processing. Images of the water calibration cells were analyzed by the following procedures.

First, the collected raw images of the wet and dry calibration cells were normalized (to correct for background noises, inhomogeneties of beam and detector, and fluctuations of neutron flux) with respect to reference images of the open beam and dark field using the following expression:

$$I_{wet} = f_r \frac{I_{(Wet\ Sample\ Image)} - I_{(Dark\ Field)}}{I_{(Open\ Beam)} - I_{(Dark\ Field)}},\ I_{dry} = f_r \frac{I_{(Dry\ Sample\ Image)} - I_{(Dark\ Field)}}{I_{(Open\ Beam)} - I_{(Dark\ Field)}} \quad [5]$$

where f_r is the rescale factor to correct the neutron beam fluctuations and is based on the differences in the mean intensity values between the selected open beam area (i.e. no object) in the sample images and the mean of the same area in the open beam images.

The normalized images, I_{wet} and I_{dry}, were despeckled using a median filter (5 pixels × 5 pixels) to remove bright pixels mainly due to scattered γ-rays. The normalized wet

images (I_{wet}) were then divided by the normalized dry images (I_{dry}). Examples of the resulting images and their intensity profiles are shown in Fig. 2-2. The longer exposure time provides a higher neutron flux, resulting in less variation in the data and better resolution of the image. However, the different exposure times did not cause any differences in measuring the water thickness. The plot profiles for the cylindrical cell (Fig. 2-2c) with different exposure times are very similar. We selected a region of interest (ROI) for each water thickness from these images while adjusting to exclude any trapped air bubbles and computed the average transmission values of the selected ROIs. The average transmission values were then plotted according to the known water thickness steps for each calibration cell.

Porous Medium and Hanging Water Column Set-Up

Flint sand (Flint #13, U.S. Silica Company, Berkeley Springs, WV) was used as a model porous medium because it is mainly composed of quartz (99.8 %) with grain diameters ranging from 0.11 mm to 0.60 mm, and a median grain diameter of 0.56 mm. Flint sand was passed through a 2 mm sieve, washed with distilled water to remove any soluble contaminants, and oven-dried before use. The quantification of water content by neutron imaging of this sand column was thus minimally affected by other water-containing materials such as organic matter or clay minerals. To set up a hanging water column an outlet at the base of the Al container was connected via Tygon tubing to a burette filled with distilled water as illustrated in Fig.2-3a. Two kinds of Al sample containers were used for the study; a rectangular (2.40 cm width × 2.62 cm thickness × 6.35 cm height) and a cylindrical container with an inner diameter 2.56 cm and a height of 10 cm. The bottom of the Al container was covered with several layers of moist Whatman #4 filter paper after removing any air bubbles in the hanging water column by suction. The oven-dried sand was then incrementally moist-packed into the Al container to minimize particle segregation and air entrapment. The heights of the packed columns were ~5 cm to fit the entire porous medium within the field of view of the HFIR CG-1D. The sand columns were fully-saturated overnight prior to each experiment. At the facility, the top of the Al container was attached to the sample holder while allowing air to flow into the Al container through small holes. The sand columns were drained under

quasi-equilibrium conditions by adjusting the height of the hanging water column to give various basal suction values, as illustrated schematically in Fig. 2-3b. A photograph of the experimental set up is shown in Fig. 2-4.

Multiple radiographic images were acquired at each quasi-equilibrium state during the main drainage process with an exposure time of 60 s. The water level in the burette was recorded simultaneously and later used to compare the measurements of total water volumes determined by the neutron radiography and hanging water column methods.

3. Results and Discussion

Effect of Sample to Detector Distance

Figure 2-5 illustrates that the transmission values when the water calibration cells were placed close to the detector (0 cm or 2.4 cm) were more scattered along the exponentially declining trend line than the corresponding values for the water calibration cell placed 24 cm away from the detector. As expected, the shorter the distance between sample and detector, the higher the transmission values. The differences in the transmission values at the different sample positions became larger as the water thickness increased, mainly due to beam hardening and scattering effects (Lehmann et al., 2004; Hassanein et al., 2005; Kardjilov et al., 2005), which increase with water thickness and decreasing distance to the detector.

Placing samples with high water contents against the detector creates severe and directional scattering that cannot be corrected for during image processing, as referenced in the literature (Lehmann et al., 2004; Hassanein et al., 2005; Kardjilov et al., 2005). However, for the HFIR CG-1D, when samples were positioned 24 cm away from the face of the detector, water thickness could be quantified since scattering effects became an offset that could be managed during image processing and analysis.

Determination of Attenuation Coefficients

Because the distance between the sample and detector influences the recorded transmission values of neutrons through the sample, attenuation coefficients were determined at the same location (24 cm from the detector) for the calibration cells and porous media images. We chose this location specifically for thick water samples to minimize the scattering effect at the sacrifice of image resolution. Kim et al. (2011) estimated the effect of sample scattering on image formation of the sample by assuming that there is an infinite line charge of neutron scattering from water with a square cross section.

$$I_S/I_T = (e^{-\Sigma\tau} - 1)\tau \,/\, (2\pi d) \qquad [6]$$

where I_S is scattering intensity, I_T is transmitted intensity, Σ is the attenuation coefficient, τ is water thickness, d is the sample to detector distance.

The net result of increasing the distance between the sample and the detector is a balance between increased unsharpness and decreased scattering. As shown by Fig.2-6 increasing the sample-to-image detector distance results in a decrease in scattering. To compare the unsharpness at different sample to detector distances a Gd straight edge from the Paul Scherrer Institute resolution mask was placed at 5 cm and 24 cm from the detector. The edge spread function (ESF) was derived by vertical averaging along the edge of the straight Gd line image. The line spread function (LSF) was obtained by taking the numerical derivative of the ESF and the full width at half maximum (FWHM) of each of the LSF's was determined. The ESF's and LSF's for both locations are shown in Fig. 2-7. The FWHM values at 5 cm and 24 cm were 131 μm and 212 μm, respectively. Moving the sample from 24 cm to 5 cm from the detector resulted in ~38% decrease in measured unsharpness and ~380% increase in predicted scattering. Even though the unsharpness decreased as the sample to detector distance decreased, the percentage decrease was an order of magnitude less than the percentage increase due to scattering. For our thick water-rich samples we opted to

reduce scattering effects at the expense of image resolution. For thinner, less water-rich samples, a smaller object to detector distance could be chosen to decrease unsharpness.

The data from each calibration cell showed little variation due to neutron beam fluctuations, different acquisition times, and other variables caused by neighboring beam lines or natural and fluorescent lights during data acquisition. To minimize statistical variations, data from all three calibration cells were pooled. Data for the cylindrical cells were restricted to chord lengths > 1.5 mm to eliminate edge effects.

To determine the attenuation coefficient for water at the HFIR CG-1D, calibration data from known water thickness were fitted to the transmission data for two different ranges of water calibration data sets (≤ 0.2 cm and ≤ 1 cm), using SAS 9.2 non-linear regression method. The predicted water thickness values using the simple Beer-Lambert law with only one attenuation coefficient without any correction factor (Σ = 5.30 cm^{-1} for ≤ 0.2 cm or 4.77 cm^{-1} for ≤ 1 cm water calibration data set) show significant deviations from the known water thickness values as the water thickness increased (Fig. 2-8). Both attenuation coefficients significantly underestimated the known values beyond 0.5 cm of water thickness and the deviation was larger for the ≤ 0.2 cm calibration data set selected to obtain the water attenuation coefficient than for the ≤ 1 cm water data set. The deviation occurs when a polychromatic beam passing through a section of water preferentially loses the lower-energy parts of its spectrum, which results in underestimation of water thickness. In addition, the deviation is increased due to strong incoherent scattering of water depending on the water thickness.

In order to empirically correct for beam hardening and scattering effects, a correction parameter β was introduced to fit the calibration data by assuming $\Sigma_w = \Sigma + \beta\tau$ (Cheng et al., 2012; Hussey and Jacobson, 2012):

$$\ln\left(\frac{I_{dry}}{I_{wet}}\right)_{(i,j)} = \Sigma\tau_{(i,j)} + \beta{\tau_{(i,j)}}^2 \qquad [7]$$

where I_{wet} and I_{dry} are the normalized wet and dry images, respectively. $\tau_{(i,j)}$ is the water thickness, Σ_w is the attenuation coefficient of water.

The attenuation coefficient Σ and correction coefficient β were obtained by fitting Eq. [7] in SAS 9.2 using the Marquardt non-linear regression method to neutron data up to 10 mm of water thickness. The fitted curve for all of the transmission data measured at HFIR CG-1D (including all three calibration cell types) shows a very good fit to the water calibration data (Fig. 2-9).

The estimated Σ and β values were implemented in MATLAB code to calculate the water thickness of the sample and applied to the cylindrical and rectangular water calibration cells and sand column images for validation of the calibration method. The water thickness of each pixel in the neutron radiographs of the rectangular and cylindrical water calibration cells was calculated using the following expression derived by solving Eq. [7] for $\tau_{(i,j)}$:

$$\tau_{(i,j)} = -\frac{\Sigma}{2\beta} - \sqrt{\left(\frac{\Sigma}{2\beta}\right)^2 - \frac{1}{\beta}\ln\left(\frac{I_{wet}}{I_{dry}}\right)_{(i,j)}} \quad [8]$$

where, $\tau_{(i,j)}$ is water thickness in cm, Σ = 5.542 cm^{-1}, β = -2.140 cm^{-2}, and I_{wet} and I_{dry} are the normalized wet and dry images, respectively.

The water thicknesses of all the calibration data were predicted by transmission images using Eq. [8] (number of observations = 289, root mean square error (RMSE) = 0.2184, R^2 = 0.9942) with an accuracy of $\pm$ 0.022 cm. The measured water thickness values from the neutron radiography were compared with those of the known water thickness from the water calibration cells (Fig. 2-10). The measured water thickness values for both the cylindrical and rectangular cells were close to the known water thickness values (from the engineering design) in the range between 0.15 cm to 0.8 cm. The results from the rectangular cells show some deviations from the 1 to 1 line at high water thicknesses (> 0.8 cm) possibly because the empirical attenuation coefficients could not account sufficiently for the scattering and beam hardening effects.

Application to a Porous Medium

Images of Flint sand packed into rectangular and cylindrical containers were used to check the empirical attenuation coefficients determined by fitting Eq. [4] to the calibration cell images. All of the porous media images were processed using the same steps as described for the calibration cells. Pore water thickness τ_{ij} (cm) was then calculated on a pixel by pixel basis (i,j) using Eq. [8].

To compute the volumetric water content (θ_{ij}, cm^3cm^{-3}) at a pixel(i,j) from neutron radiography of a rectangular container, the measured water thickness was divided by the beam path length (l_{ij}) , (= 2.62 cm), i.e.

$$\theta_{ij} = \frac{\tau_{ij}}{l_{ij}} \times \frac{pixel\ area}{pixel\ area} = \frac{\tau_{ij}}{l_{ij}} \quad [9]$$

To compute the volumetric water content (θ_{ij}) from neutron radiography of a cylindrical container, the measured water thicknesses were corrected for variations in the transmission path length of neutrons based on the chord length (C_{ij}) for a circle (Eq. 4).

The volumetric water content at the pixel(i,j), θ_{ij} (cm^3cm^{-3}) is then the ratio of the measured water thickness to the chord length:

$$\theta_{ij} = \frac{\tau_{ij}}{C_{ij}} \times \frac{pixel\ area}{pixel\ area} = \frac{\tau_{ij}}{C_{ij}} \quad [10]$$

In order to compare changes in total water volume obtained by neutron radiography with those obtained independently from the hanging water column method, the total water volume using neutron radiography was calculated from the average volumetric water content. To obtain the average volumetric water content ($< \theta_v >$) for each suction applied, the individual θ_{ij} values from the neutron radiographs were arithmetically averaged over the imaged area, i.e.

$$< \theta_v > = \frac{\sum_1^n \theta_{ij}}{n} \quad [11]$$

where n is the total number of pixels in the ROI.

The expressions used to compute the total water volumes in the rectangular and cylindrical containers are given below:

$$V_w(cm^3) = < \theta_v > \times \ n \ \times \ l_{ij} \ \times pixel\ area$$
$$V_w(cm^3) = < \theta_v > \times \ \sum_1^n \ (C_{ij} \ \times pixel\ area) \quad [12]$$

where V_w is total volume of water in the column, $< \theta_v >$ is the average volumetric water content at a given suction, n is the total number of pixels in the ROI, l_{ij} is the beam path length for the rectangular container, C_{ij} is the chord length for the cylindrical container. 95% confidence intervals were calculated by varying the ROI; 4 different ROIs were selected for these calculations.

The cumulative water volume changes were calculated by subtracting the water volume of the driest image during the drainage process. The cumulative water volume changes in the porous media determined by neutron radiography were compared with those recorded by direct reading from the burette connected to a hanging water column. Fig. 2-11 shows the results of cumulative average water volume changes in Flint sand measured in rectangular and cylindrical containers at quasi-equilibrium during monotonic drying. The changes in total water volumes measured in the rectangular and cylindrical containers were very similar showing no significant effect on the quantification in relation to sample geometry. Neutron radiography slightly overestimates the water volume changes relative to the results from the hanging water column, especially at high water volumes (> ~8 cm^3) contrary to the water calibration data in Fig. 2-10. This contrast result might be due to summation of errors since we used cumulative changes in water volume for the porous medium. However, data from both the rectangular and cylindrical containers are generally in good agreement with the hanging water column measurements (i.e., close to the 1:1 line).

4. Conclusions

Data from each calibration cell type (rectangular and cylindrical) showed little variation in transmission for the same water thickness. There was no significant effect due to geometry or cell designs for the water calibration experiments. Strong scattering effects were observed with increasing thickness of water (> 0.2 cm) when the water calibration cells were positioned close to the face of the detector (0 and 2.4 cm away, respectively). Accurate quantification of volumetric water contents in calibration cells and porous media using neutron radiography data can be obtained with empirical attenuation coefficients for water determined at some distance from the detector (in this case, 24 cm). These coefficients were obtained by fitting Eq. [7] to experimental water calibration data from rectangular and cylindrical calibration cells by means of non-linear regression. The resulting estimates were successfully applied to quantify changes in the total water volume of packed columns of Flint sand. Changes in cumulative total water volumes determined by neutron radiography showed good agreement with those obtained by the conventional hanging water column method. These results allow extension of the calibration equation to the quantification of high water contents within other samples of porous media positioned at a specific distance from the detector. The parameters (Σ and β) presented in this paper are unique for HFIR CG-1D. Other facilities can determine unknown water contents by obtaining their own unique Σ and β parameters for water at an optimal sample location in a specific beam line. The optimal sample location can be found, depending on the maximum water content of the sample, for a specific detector at each beam line by examination of the measured neutron transmission for water calibration cells positioned at a few selected locations.

Acknowledgements

This Research was supported by the Laboratory Directed Research and Development (LDRD) Program of Oak Ridge National Laboratory and the Joint Directed Research and Development (JDRD) Program of the University of Tennessee UT-ORNL Science

Alliance. The Authors are thankful for contributions from Lakeisha Walker, Keely Willis, and the HFIR support groups, especially the HFIR Machine Shop, Brent Taylor, Gary Lynn, Lisa Fagan, Jaimie Werner, and the Instrument Development Group. The detector set-up was developed in collaboration with Prof. Dayakar Penumadu in the Department of Civil and Environmental Engineering at the University of Tennessee - Knoxville. This Research at Oak Ridge National Laboratory's High Flux Isotope Reactor was sponsored by the Scientific User Facilities Division, Office of Basic Energy Sciences, U. S. Department of Energy, which is managed by UT-Battelle, LLC.

References

Anderson I.S., R. McGreevy, and H. Bilheux, Neutron Imaging and Applications: A Reference for the Imaging Community, Springer, New York, 2009.

Arif M., D. L. Jacobson, and D. S. Hussey, Neutron Imaging Study of the Water Transport in Operating Fuel Cells; DOE Hydrogen Program FY 2009 Annual Progress Report, http://www.hydrogen.energy.gov/pdfs/progress09/v_a_8_arif.pdf

Basavaraj M.G. and G.S. Gupta, New calibration technique for X-ray absorption in single and multiphase flow in packed beds, ISIJ Int. (Iron Steel Inst. Jpn.) 44 (2004) 50.

Bayer A., H.-J. Vogel, and K. Roth, Direct measurement of the soil water retention curve using X-ray absorption, Hydrol. Earth Syst. Sc. 8 (2004) 2.

Bilheux H., K. Crawford, L. Walker, S. Voisin, M. Kang, M. Harvey, B. Bailey, M. Phillips, J-C. Bilheux, K. Berry, J. Ankner, J. Warren, J. Nanda, S. Pannala, M. Lance, Neutron imaging at the Oak Ridge National Laboratory: Present and Future Capabilities, 7th International Topical Meeting on Neutron Radiography, 2012 (in press)

Cheng C.-L., M. Kang, E. Perfect, S. Voisin, J. Horita, H.Z. Bilheux, J.M. Warren, D.L. Jacobson, and D.S. Hussey, Average soil water retention curves measured by neutron radiography, Soil Sci. Soc. Am. J. 76 (2012) 1164.

Cnudde V., M. Dierick, J. Vlassenbroeck, B. Masschaele, E. Lehmann, P. Jacobs, and L. Van Hoorebeke, High-speed neutron radiography for monitoring the water absorption by capillarity in porous materials, Nucl. Instrum. Methods Phys. Res. B 266 (2008) 155.

Hall L.D., G.M.H. Amin, E. Dougherty, M. Sanda, J. Votrubova, K.S. Richards, R.J. Chorley, and M. Cislerova, MR properties of water in saturated soils and resulting loss of MRI signal in water content detection at 2 Tesla, Geoderma 80 (1997) 431.

Hassanein R., E. Lehmann, and P. Vontobel, Methods of scattering corrections for quantitative neutron radiography, Nucl. Instrum. Methods Phys. Res. A 542 (2005) 353.

Hassanein R., F. de Beer, N. Kardjilov, and E. Lehmann, Scattering correction algorithm for neutron radiography and tomography tested at facilities with different beam characteristics. Physica B, 385-386 (2006) 1194.

Hincapié I.and P. Germann, Gravity-driven viscous flow in sand boxes assessed with neutron radiography, Vadose Zone J. 8 (2009) 891.

Hincapié I.and P. Germann, Water content wave approach applied to neutron radiographs of finger flow, Vadose Zone J. 9 (2010) 278.

http://www.mathworks.com

Hussey D.S., D.L. Jacobson, K.J. Coakley, D.F. Vecchia, and M. Arif, In situ fuel cell water metrology at the NIST-NCNR neutron imaging facility, J. Fuel. Cell Sci. Tech. 7 (2010) 22.

Hussey D.S., D.L. Jacobson, "Neutron radiography for PEMFCs: High resolution studies", in: C. Hartnig, C. Roth (Eds.) Polymer electrolyte membrane and direct methanol fuel cell technology, Vol. 2 in situ characterization of PEMFCs and DMFCs, Woodhead, Cambridge, U.K., 2012.

Kardjilov N., F.C. De Beer, R. Hassanein, E. Lehmann, and P. Vontobel, Scattering corrections in neutron radiography using point scattered functions, Nucl. Instrum. Methods Phys. Res. A 542 (2005) 336.

Kardjilov N., S. Baechler, M. Bastürk, M. Dierick, J. Jolie, E. Lehmann, T. Materna, B. Schillinger, P. Vontobel, New features in cold neutron radiography and tomography Part II: applied energy-selective neutron radiography and tomography, Nucl. Instrum. Methods Phys. Res. A 501 (2003) 536.

Kardjilov N., B. Schillinger, E. Steichele, Energy-selective neutron radiography and tomography at FRM, Appl. Radiat. Isot. 61 (2004) 455.

Kim F., D. Penumadu, and D.S. Hussey, Water distribution variation in partially saturated granular materials using neutron imaging, J. Geotech. Geoenviron. Eng. 138 (2011) 147

Lehmann E.H., P. Vontobel, and N. Kardjilov, Hydrogen distribution measurements by neutrons, Appl. Radiation Isotopes 61 (2004) 503.

Moradi A.B., H.M. Conesa, B.H. Robinson, E. Lehmann, G. Kühne, A. Kaestner, and R. Schulin, Neutron radiography as a tool for revealing root development in soil: capabilities and limitations, Plant Soil 318 (2009) 243.

Oswald S., W. Kinzelbach, A. Greiner, and G. Brix, Observation of flow and transport processes in artificial porous media via magnetic resonance imaging in three dimensions, Geoderma 80 (1997) 417.

Oswald S.E., M. Menon, A. Carminati, P. Vontobel, E. Lehmann, and R. Schulin, Quantitative imaging of infiltration, root growth, and root water uptake via neutron radiography, Vadose Zone J. 7 (2008) 1035.

Rasband W.S., ImageJ, U. S. National Institutes of Health, Bethesda, Maryland, USA, http://rsb.info.nih.gov/ij/, 1997−2008.

SAS/STAT 9.2 User's Guide: The NLIN Procedure (Book Excerpt).

Strobl M., I. Manke, N. Kardjilov, A. Hilger, M. Dawson, and J. Banhart, Advances in neutron radiography and tomography, J. Phys D Appl. Phys. 42 (2009) 243001.

Trabold T.A., J.P. Owejan, J.J. Gagliardo, D.L. Jacobson, D.S. Hussey, and M. Arif, Use of neutron imaging for proton exchange membrane fuel cell (PEMFC) performance analysis and design, Handbook of Fuel Cells-Fundamentals, Technology and Applications, Chapter 44, Wiley and Sons, 2009.

Treimer W., M. Strobl, N. Kardjilov, A. Hilger, and I. Manke, Wavelength tunable device for neutron radiography and tomography, Appl. Phys. Lett. 89 (2006) 203504

Tremsin A. S., W. B. Feller, R. G. Downing, Neutron Collimation With Microchannel Plates: Calibration of Existing Technology and Near Future Possibilities. Nucl. Instrum. Methods Phys. Res. A 539 (2005) 278.

Tumlinson L.G., H. Liu, W.K. Silk, and J.W. Hopmans, Thermal neutron computed tomography of soil water and plant roots, Soil Sci. Soc. Am. J. 72 (2008) 1234.

Turhan A., K. Heller, J.S. Brenizer, and M.M. Mench, Quantification of liquid water accumulation and distribution in a polymer electrolyte fuel cell using neutron imaging, J. Power Sources 160 (2006) 1195.

Appendix B

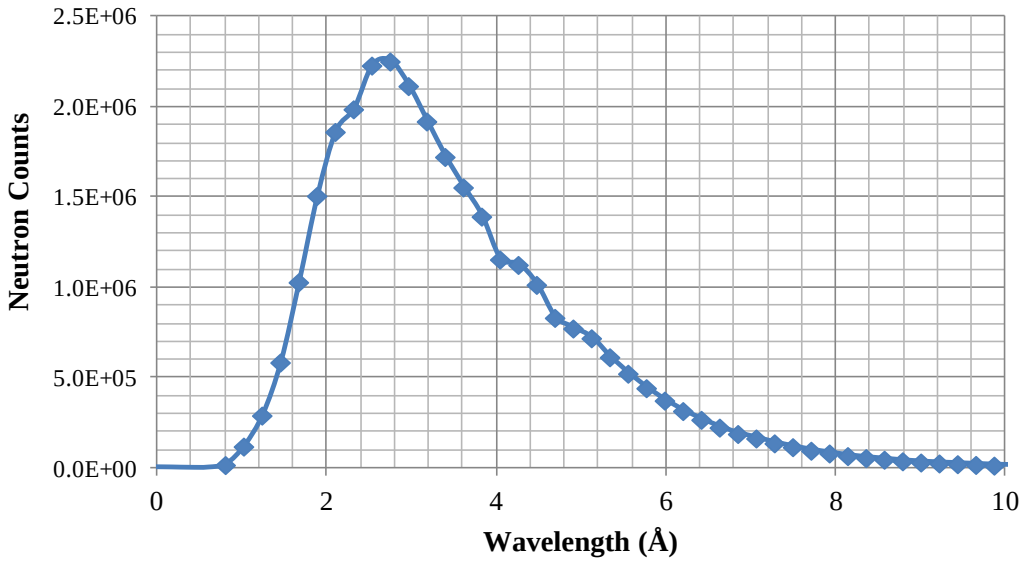

Figure 2- 1 The CG-1D spectrum measured with an MCP detector at a flight path distance of approximately 5.5 m, with the chopper running at a frequency 40 Hz.

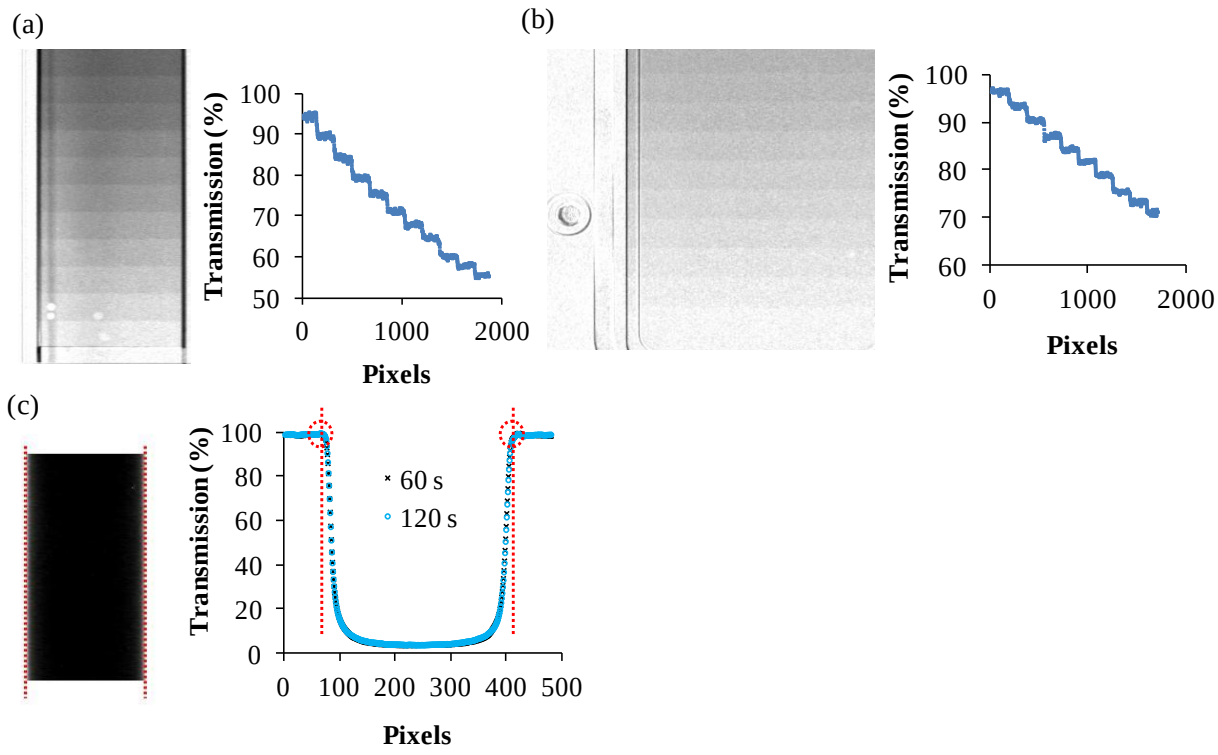

Figure 2- 2 Examples of wet transmission images for each calibration cell type after division by the dry cell and their corresponding transmission profiles: (a) rectangular calibration cell #1 with 11 steps of water thickness from 0.005 to 0.105 cm (0.01 cm increment) with 600 s exposure time, (b) rectangular calibration cell #2 with 10 steps of water thickness from 0.005 to 0.05 cm (0.005 cm increment) with 300 s exposure time, and (c) cylindrical calibration cell with water thickness ranging from 0 − 0.909 cm with 120 s exposure time (note: the transmission profile for the cell also includes results for 60 s exposure time). All examples are for the 24 cm sample position.

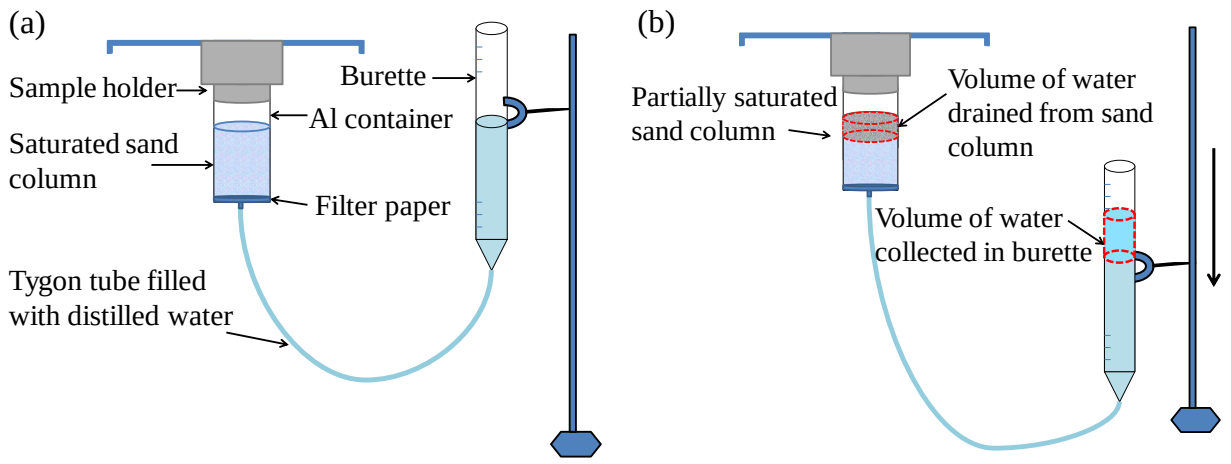

Figure 2- 3 Schematic diagram of the hanging water column set up: (a) initially saturated sand column and (b) drainage process achieved by lowering the burette. Note that the volume of water drained from the sand column is equal to the volume of water collected in the burette.

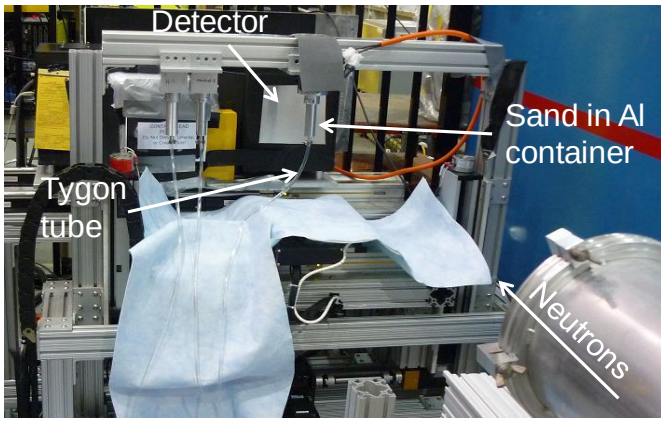

Figure 2- 4 Hanging water column set-up at HFIR CG-1D neutron imaging facility.

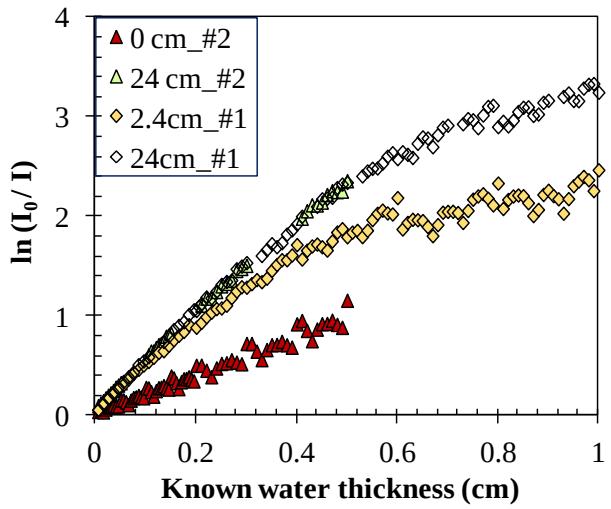

Figure 2- 5 Comparison of $\ln(I_0/I)$ values for rectangular water calibration cells (#1 and #2) at three different positions (0, 2.4, and 24 cm) from detector at the HFIR CG-1D neutron imaging facility. Note that images for cell #2 at 0 and 24 cm were normalized with respect to the open beam rather than the dry cell. The aluminum thickness for cell #2 was thinner than that for cell #1, and that normalization relative to the open beam was sufficient for cell #2 but not for cell #1 which required normalization by the dry image. Error bars (95% confidence intervals) for all the data are smaller than the symbols (error ≤ ± 0.0064 cm).

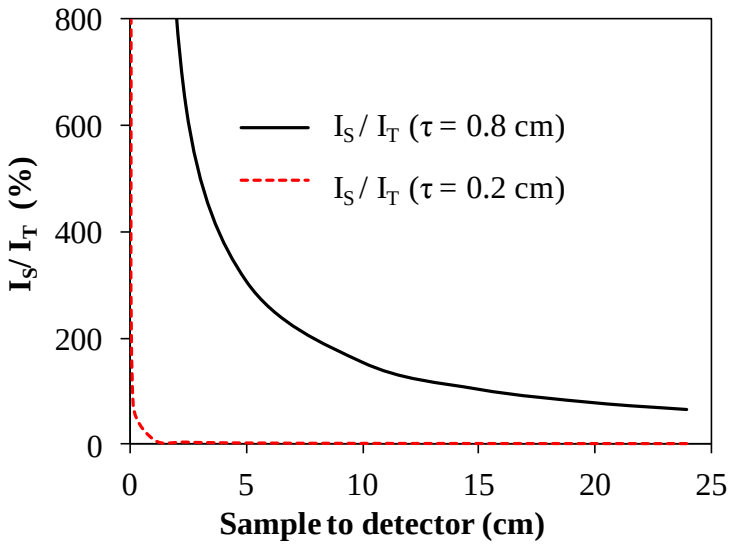

Figure 2- 6 The ratio of scattering intensity to the transmitted intensity as a function of sample to detector distance is predicted assuming Σ = 6 cm^{-1} using Eq. [6].

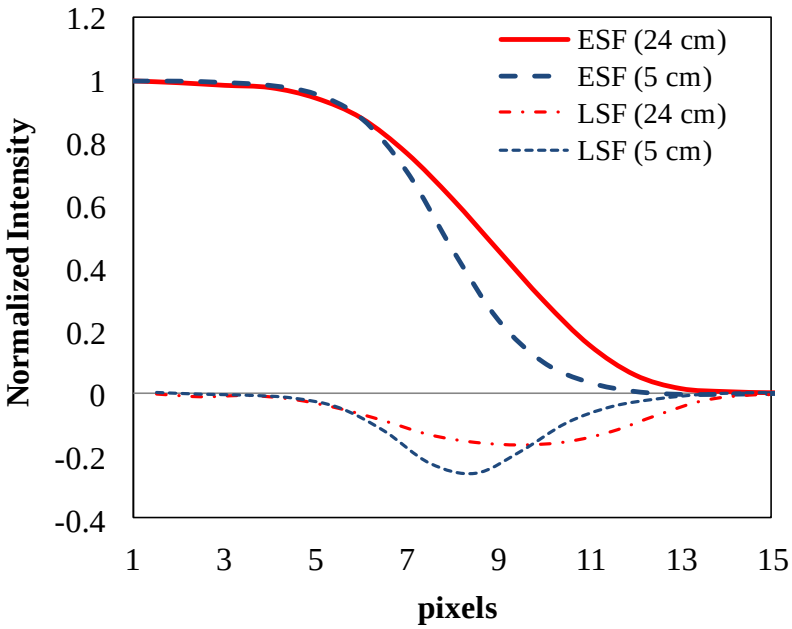

Figure 2- 7 Measured ESF's and LSF's for a Gd straight edge from the Paul Scherrer Institute resolution mask at 5 cm and 24 cm sample to detector distances.

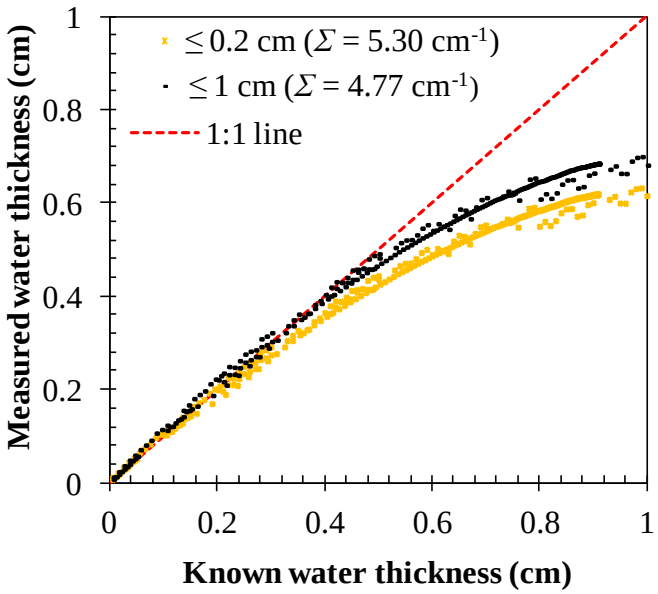

Figure 2- 8 Deviation of measured water thickness from the known water thickness when using attenuation coefficients obtained from the Beer-Lambert law for two different selected data ranges: ≤ 0.2 and ≤ 1 cm of water thickness.

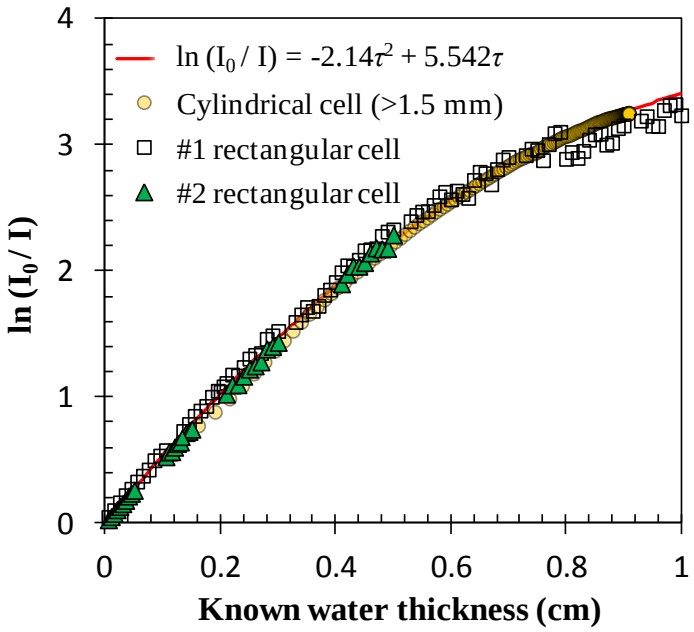

Figure 2- 9 Best fit of Eq. [7] to the measured neutron data versus known water thickness (τ) for all three calibration cell types located 24 cm away from the detector.

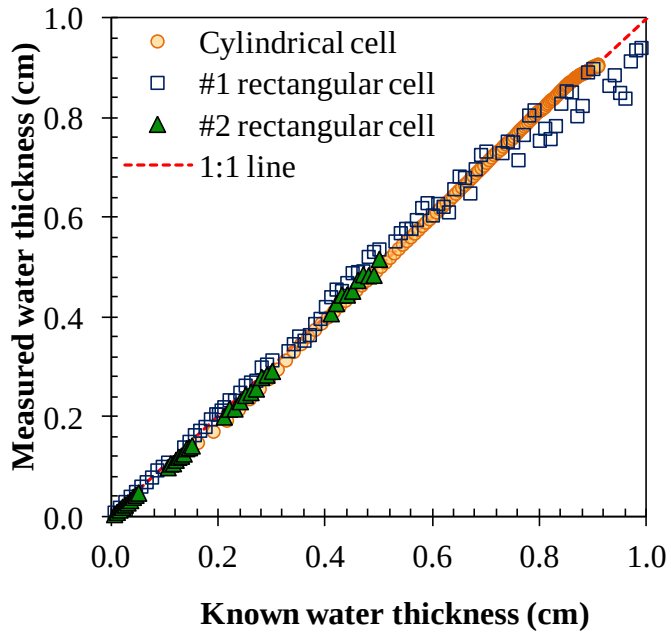

Figure 2- 10 Comparison of the measured average water thickness values using attenuation coefficients determined from calibration cell data and known water thickness values for the cylindrical and rectangular water calibration cells.

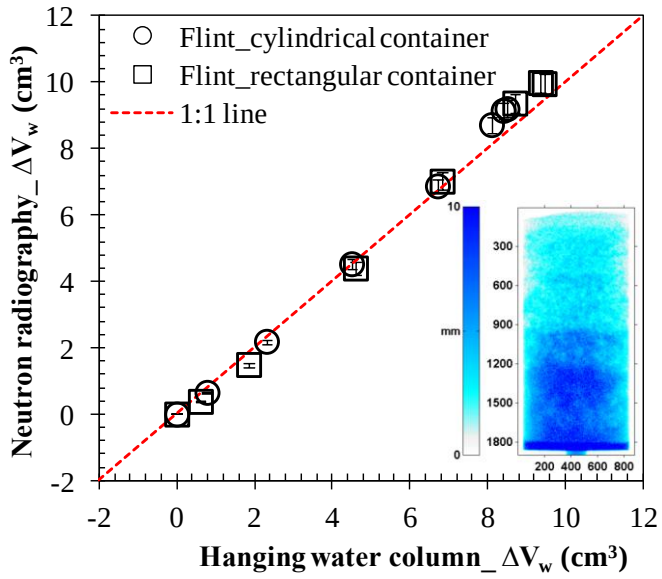

Figure 2- 11 Comparison of cumulative total water volume changes in Flint sand in rectangular (squares) and cylindrical (circles) containers measured by neutron radiography and the conventional hanging water column method at quasi-equilibrium during monotonic drying. The error bars represent the 95% confidence intervals (note: some of the confidence intervals are too small to be seen). Inset shows the water thickness distribution within the sample at ΔV_w = 4.5 cm^3 for the cylindrical sand column.

CHAPTER III

AVERAGE SOIL WATER RETENTION CURVES MEASURED BY NEUTRON RADIOGRAPHY

This chapter is a reformatted version of a paper originally published in Soil Science Society of America Journal in 2012 by Cheng et al. Misun Kang contributed to the data acquisition, data analyses, and writing and revision of the manuscript.

Cheng C.-L., M. Kang, E. Perfect, S. Voisin, J. Horita, H.Z. Bilheux, J.M. Warren, D.L. Jacobson, and D.S. Hussey, 2012. Average soil water retention curves measured by neutron radiography, Soil Sci. Soc. Am. J. 76(4): 1184-1191

Abstract

Water retention curves are essential for understanding the hydrologic behavior of partially saturated porous media and modeling flow and transport processes within the vadose zone. We directly measured the main drying and wetting branches of the average water retention function obtained using two dimensional neutron radiography. Flint sand columns were saturated with water and then drained and rewetted under quasi-equilibrium conditions using a hanging water column setup. Digital images (2048 by 2048 pixels) of the transmitted flux of neutrons were acquired at each imposed matric potential (~10–15 matric potential values per experiment) at the National Institute of Standards and Technology Center for Neutron Research BT-2 neutron imaging beam line. Volumetric water contents were calculated on a pixel-by-pixel basis using Beer-Lambert's law after taking into account beam hardening and geometric corrections. To account for silica attenuation and remove scattering effects at high water contents, the volumetric water contents were normalized (to give relative saturations) by dividing the drying and wetting sequences of images by the images obtained at saturation and satiation, respectively. The resulting pixel values were then averaged and combined with information on the imposed basal matric potentials to give average water retention curves. The average relative saturations obtained by neutron radiography showed an approximate one-to-one relationship with the average values measured volumetrically using the hanging water column setup. There were no significant differences (at $p < 0.05$) between the parameters of the van Genuchten equation fitted to the average

neutron radiography data and those estimated from replicated hanging water column data. Our results indicate that neutron imaging is a very effective tool for quantifying the average water retention curve.

1. Introduction

Because of the strong attenuation of neutrons by hydrogen in water and their relatively small attenuation by air and mineral solids (Anderson et al., 2009; Strobl et al., 2009), neutrons have long been used to measure the soil water content. The neutron probe was first developed >60 yr ago, and it continues to be a common and reliable field instrument for measuring water content in the vadose zone (Belcher et al., 1950; Gardner and Kirkham, 1952; Schmugge et al., 1980; Chanasyk and Naeth, 1996). When combined with paired tensiometer measurements, the neutron probe can also be used to determine the soil water retention curve (e.g., Andreu et al., 1997; Al-Yahyai et al., 2006). Like the hanging water column and pressure cell laboratory techniques (Dane and Hopmans, 2002), however, this is essentially a “black box” approach that provides an “average” water retention curve associated with a given sampling volume. During the past two decades, the use of nondestructive testing to study flow and transport processes in porous media has grown significantly (Chaouki et al., 1997). Nondestructive testing offers the possibility of seeing into the “black box” and determining the point water retention function. Gamma beam attenuation (Dane et al., 1992), magnetic resonance imaging (Chen and Balcom, 2005), and x-ray computed tomography (Bayer et al., 2004) have all been used to determine point water retention curves for air displacing water in porous media. Neutron imaging is a nondestructive testing method based on measuring the transmitted intensity of neutrons, either in two or three dimensions (referred to as radiography and tomography, respectively). Neutron imaging is a particularly powerful tool with respect to soil water due to its high spatial and temporal resolutions and relatively large imaging area (up to 500 cm2) (Chaouki et al., 1997; Deinert et al., 2004; Trabold et al., 2009; Heller et al., 2009).

Since it was first applied to visualize the spatial distribution of soil water in the 1970s (Lewis and Krinitzsky, 1976), the number of studies using neutron imaging to monitor fluids in porous media has grown rapidly. Deinert et al. (2004) used real-time neutron radiography to measure fluid contents and wetting front profiles in homogeneous silica sand. They were able to estimate the hydraulic conductivity and diffusivity from the flow field images with satisfying results. They also concluded that neutron imaging is an ideal

tool for detailed laboratory studies because of its sensitivity to variations in moisture content and its ability to image nontranslucent media. Heller et al. (2009) measured the water volume in fuel cells by neutron computed tomography and indicated that the quantification technique yielded a value of the water column mass within 2% of the theoretical. Recent studies have focused on capillary-driven imbibition (Hassanein et al., 2006b; Cnudde et al., 2008; El Abd et al., 2009), root water uptake (Oswald et al., 2008), and gravity-driven fingering (Hincapié and Germann, 2009, 2010).

Because of its capability for high resolution spatial and temporal measurements of water in porous media, neutron imaging is an ideal technique for investigating hysteresis of the soil water retention function. Tumlinson et al. (2008) applied neutron tomography to construct a small portion of the main drying curve based on a single applied pressure. Vasin et al. (2008) measured average drainage curves for heterogeneous sand columns comprised of coarse and fine sands packed into random and periodic cellular structures using neutron tomography performed under quasi equilibrium conditions. To the best of our knowledge, neutron radiography has not been previously employed to measure hysteretic soil water functions.

The main thrust of our research is to apply the neutron imaging technique to directly measure point soil water retention functions. The specific objective of this paper is to compare hysteresis in drying and wetting measurements obtained by neutron radiography with those from the traditional hanging water column method. Because the traditional hanging water column method produces an average water retention curve (for the entire soil volume investigated) we will compare the two data sets by averaging the neutron radiographic point (or pixel by pixel) measurements of relative saturation over the imaged soil area. Both sets of average water retention curves will then be fitted to the van Genuchten equation (van Genuchten, 1980) and their resulting parameter estimates compared statistically.

2. Materials and Methods

Sample Properties and Column Preparation

Coarse-grained, homogeneous sand (Flint no.13, U.S. Silica Company, Berkeley Springs, WV[2]) was selected for study because it can be completely drained by a hanging water column within the height constraints of the neutron beamline setup at NIST and because it is free of any organic materials that could complicate the quantification of water content by neutron imaging. Flint no.13 sand is mainly composed of quartz (99.8%); grain diameters range from 0.11 mm to 0.60 mm; the median grain diameter is 0.56 mm; the grain density is 2.65 g cm^{-3} (U.S. Silica Company, 2009). The saturated hydraulic conductivity, determined using the constant-head method implemented without a water tank is 1.66 x 10^{-4} m s^{-1} ± 0.32 x 10^{-4} m s^{-1} (Reynolds and Elrick, 2002).

Sand samples were washed with distilled water and oven dried before use. They were then moistened with de-aired, distilled water and packed into custom-made Al cylinders (Al alloy 6062) with a height of 12.56 cm and a diameter of 2.65 cm. The top of the Al cylinder was open to the atmosphere. A hanging water column made out of Tygon® tubing (R3603, 3.175 mm (1/8 in) ID x 6.35 mm (1/4 in) OD, Fisher Scientific, Hampton, NH) and a glass burette of 25 ml volume (Fisher Scientific, Hampton, NH), filled with de-aired, distilled water, was connected to an outlet at the base of the Al cylinder. The bottom of the cylinder was covered with several layers of moist Whatman no. 4 filter paper (150 mm diameter, 25 µm) (Whatman, Maidstone, UK). Any air bubbles in the hanging water column were removed by suction prior to placing the filter paper. The sand was then incrementally moist-packed into the cylinder to minimize particle segregation and air entrapment. The average height of the packed sand

[2] Certain trade names and company products are mentioned in the text or identified in an illustration in order to adequately specify the experimental procedure and equipment used. In no case does such identification imply recommendation or endorsement by the National Institute of Standards and Technology, nor does it imply that the products are necessarily the best available for the purpose.

columns was 4.25 cm ± 0.05 cm with an average bulk density of 1.74 g cm^{-3} ± 0.02 g cm^{-3}. The burette and sand column setups were clamped to a steel stand. Prior to each experiment the burette at the end of the hanging water column was raised to the top of the sand pack and allowed to equilibrate overnight to fully saturate the column. The top of the aluminum column was loosely covered with aluminum foil to minimize evaporation from the saturated sample.

Neutron Imaging Experiments

Neutron radiography was performed at the NIST Center for Neutron Research (NCNR) BT-2 imaging beam line. The BT-2 imaging facility was equipped with a Gadox scintillator (Lexel Imaging) and a charge coupled device (CCD) camera (Andor). The field of view was 4.5 x 4.5 cm^2, with a resolution of 50 µm. The ratio of the collimator tube length to its aperture diameter (the L/D ratio) was 600 and the neutron flux was 4.97 x 10^6 cm^{-2} s^{-1}. It should be emphasized that the NIST-NCNR BT-2 facility uses a thermal neutron source. In contrast to cold neutrons, thermal neutrons have higher transmission through relatively thick sections of scattering material (Riley et al., 2009; Mukundan and Borup, 2009). The BT-2 beam line has previously been used to image water in granular materials by Kim et al. (2011).

Radiography data sets for air displacing water and vice versa in a Flint sand column were acquired at NCNR during March, 2010 (4 days of total beam time). A pre-saturated Flint sand column sample, connected to a hanging water column, was set up in the BT-2 beamline. The distance between the column and the detector screen was ~1.6 cm. A schematic diagram of the experimental set up is shown in Fig. 3-1[3]. The column was drained and rewetted under quasi-equilibrium conditions by adjusting the height of the hanging water column outside of the beamline to give between 10 and 15 basal matric potential values per drying/wetting cycle. The mid-point of the sand pack was considered to be the level of zero matric potential at complete saturation. Radiographs were taken at each quasi-equilibrium state during the drying and wetting

[3] Note: All tables and figures are located in Appendix C.

cycles with an exposure time of 60 s. Each image was comprised of 2048 x 2048 pixels. The water level in the burette at each equilibrium state was recorded simultaneously and later used to construct the main drainage and wetting branches of the water retention curve. Replicate experiments were not possible because of the limited amount of beam time available for the experiment.

An oven-dry sample was prepared by placing a Flint sand column at residual saturation in an oven with the temperature set at 105°C for 32 h. The oven-dry sample was then imaged following the procedure described above for later analysis to estimate the attenuation of the dry silica sand and Al container. The ovendry sample was immediately placed in the beam line when it was removed from the oven. The top of the Al container was loosely covered with Al tape. The likelihood of water adsorbing onto particle surfaces from the atmosphere was considered negligible due to the short exposure time, covering material used, and the coarse grain size of the Flint sand.

Image Analysis

All image processing and quantitative analyses were performed using the MATLAB (Version 7.11, R2010b-SP1, Mathworks, Inc., 2011) and ImageJ (Version 1.43m, National Institutes of Health, 2009) software packages. The raw neutron radiographs were analyzed to obtain the distribution of volumetric water contents within the sandl column on a pixel by pixel basis. The transmission of neutrons through the sand column can be described using the Lambert-Beer law (Berger, 1971):

$$I/I_0 = \exp(-\tau\mu) \qquad [1]$$

where I is the transmitted intensity, I_0 is the original intensity, τ is the water thickness, and μ is the attenuation coefficient for the porous medium, which includes water, air, silica sand, and the aluminum wall of the sample container. The attenuation coefficient for air is very small and can be neglected. Measurements of the attenuation coefficients for aluminum and silica sand indicate they are small compared to that for the hydrogen in water (see RESULTS and DISCUSSION). The collected raw images were first gamma filtered and then normalized with respect to reference images of the open beam

(shutter opened without a sample) and dark field (shutter closed, no neutron illumination) using:

$$I/I_0 = \frac{I_{(Raw\ Image)} - I_{(Dark\ Field)}}{I_{(Open\ Beam)} - I_{(Dark\ Field)}} \quad [2]$$

The water thickness τ_{ij} (cm) was then calculated on a pixel-by pixel basis (i,j) using Eq. [2] combined with the following expression derived from Eq. [1] by assuming $\mu_w = \mu + \beta\tau$:

$$\tau_{ij} = -\frac{\mu}{2\beta} - \sqrt{(\frac{\mu}{2\beta})^2 - \frac{1}{\beta}\ln(I/I_{0_{(i,j)}})} \quad [3]$$

where μ = 0.326 mm^{-1} is the linear attenuation coefficient for water and β = -0.0121 mm^{-2} is a beam hardening correction coefficient for the detector used. Note that both constants vary with the specific imaging facility and detector system and due to the sensitivity to the energy spectrum of the neutron beam when the experiments were conducted.

Because of the cylindrical geometry of the packed sand column, the measured water thicknesses were corrected for variations in the transmitted path length of neutrons based on the chord length, C_{ij}, for a circle:

$$C_{ij} = 2\sqrt{r^2 - a_{(i,j)}^2} \quad [4]$$

where r is the radius of the sand column (cm) and $a_{(i,j)}$ is the distance from the center of the column to the pixel (i,j) (cm). The volumetric water content at the pixel (i,j), θ_{ij} (cm^3 cm^{-3}), is then simply the ratio of the measured water thickness to the chord length, i.e.

$$\theta_{ij} = \frac{\tau_{ij}}{C_{ij}} \times \frac{pixel\ area}{pixel\ area} = \frac{\tau_{ij}}{C_{ij}} \quad [5]$$

The drying and wetting θ_{ij} values were normalized (to give relative saturations, S_{ij}) by dividing each image field, on a pixel by pixel basis, by the image fields of θ_{ij} values obtained at saturation (drying curve) and satiation (wetting curve), respectively. In order to compare the water retention curves obtained by neutron radiography with those from the hanging water column method, the individual θ_{ij} and S_{ij} values from the neutron radiographs were averaged over the imaged soil area for each matric potential, i.e., $\theta = < \theta_{ij} >$ and $S = < S_{ij} >$.

Hanging Water Column Experiments

In addition to the neutron imaging experiments, replicated conventional hanging water column experiments were performed at NIST and in the Vadose Zone Laboratory of the Department of Earth and Planetary Sciences at the University of Tennessee-Knoxville, TN. These experiments were conducted as described above and using the same experimental setup as in Fig. 3-1 except that the average water contents were determined volumetrically by recording water level changes in the burette. Two of the five columns, however, were not rewetted. Thus, five replicate drying curves and three replicate wetting curves were obtained for comparison with the average drying and wetting curves obtained by neutron radiography. Relative saturations, *S*, were again calculated by dividing the measured $<\theta>$ values by the saturated (drying) and satiated (wetting) $<\theta>$ values for the drying and wetting curves, respectively.

Parameterization of Water Retention Curves

The average neutron radiography and conventional hanging water column data sets were both parameterized by fitting the van Genuchten, VG, equation (van Genuchten, 1980). The VG equation was fitted in the following form:

$$S = S_r + (1 - S_r)[1 + (\alpha|\psi|)^n]^{-\left(1-\frac{1}{n}\right)} \quad [6]$$

where S_r is the residual saturation, α is a parameter inversely related to the air or water entry values, and *n* is a shape parameter influenced by the pore-size distribution. For

the conventional water retention curves, the fitting was done using the pooled data from all of the replicate hanging water column experiments. Equation [6] was fitted to the drying and wetting curves simultaneously using segmented non-linear regression (Marquardt method) in SAS 9.2 (SAS Institute Inc., Cary, NC). This fitting procedure produces a single estimate of S_r for each method while different estimates of α and *n* are obtained depending upon the method and if air is displacing water (drying) or vice versa (wetting). The goodness of fit was assessed based on the root mean square error (RMSE) and by linear regression of the observed and predicted *S* values to give a coefficient of determination (R^2).

For statistical testing, Eq. [6] was also fitted separately to each of the five replicate hanging water column data sets. The wetting and drying curves were fitted simultaneously as described above, except for the two experiments that were not rewetted; in those cases, Eq. [6] was only fitted to the main drying curve. The R^2 values for the individual fits ranged from 0.996 to 0.999. The mean values of the resulting VG parameters were then compared with the single VG parameter estimates from the neutron imaging data using one-sample *t*-tests in SAS.

3. Results and Discussion

The average volumetric water contents computed from the neutron radiography measurements are plotted against those from the volumetric hanging water column measurements in Fig. 3-2a for the complete range of imposed basal matric potentials. As can be seen, the volumetric water contents from the neutron images were significantly overestimated for both the drying and wetting cycles. Average water content values at saturation and satiation for the two different methods are summarized in Table 3-1.

An oven dry sample was also imaged and the attenuation coefficient for silica sand and the aluminum container was determined to be 0.023 mm^{-1}. Separate measurements for aluminum indicate an attenuation coefficient of 0.009 mm^{-1}. Compared to the attenuation coefficient of 0.326 mm^{-1} for water, these values are

relatively small. As shown in Figure 3-3, the effect of the aluminum walls of the sample container on the transmission of neutrons is minimal. The attenuation due to the presence of silica sand, however, has a noticeable effect on relative intensity (Fig. 3-3). Analysis of the oven-dry sample image showed that the neutron attenuation due to the aluminum container and silica sand was equivalent to a volumetric water content of 0.050 ± 0.001 $m^3 m^{-3}$. This attenuation of the dry components was accounted for in the wet samples.

Because of the effect of the attenuation of silica sand in the oven dry sample, the neutron imaging water content values were corrected on a pixel by pixel basis by subtracting the oven dry pixel field from the water content fields for each drying/wetting matric potential. The corrected volumetric water contents, $\theta_{corrected}$, showed much better agreement with the volumetric water contents measured by the hanging water column method (Fig. 3-2b). However, the wet ends of the drying and wetting curves were slightly underestimated (Fig. 3-2b and Table 3-1). There was also an anomalous central zone of underestimated water contents within the corrected water content field for the fully-saturated sample (Fig. 3-4). We believe this phenomenon is due to both scattering effects (Hassenein et al., 2005, 2006a, 2006b, Hussey, 2010) and not correcting the images for the point spread function of the detector. Until a better solution is developed we decided to effectively remove this phenomenon by working with relative saturations instead of volumetric water contents. This approach limits the ability of neutron imaging to quantify soil hydraulic properties, but only slightly since it is relatively easy to obtain accurate estimates of the saturated water content using traditional methods such as calculation from the bulk and particle densities.

Relative saturations were calculated on a pixel by pixel basis as described in the Methods section. Inspection of the resulting *S* fields for the saturated and satiated states revealed homogeneous values of unity as expected (data not shown). The *S* fields became increasing heterogeneous once the matric potential decreased below the air entry value during drainage, with air progressively displacing pore water from the top of the column downwards (Fig. 3-5). Local variations in the position of the drying front are clearly visible at each matric potential. Eventually the images became relatively homogenous again as the entire sand pack was completely drained. It can be clearly

seen in Fig. 3-5 that the filter paper phase barrier at the bottom of the sand column always remained fully saturated regardless of the imposed matric potential. Similar results (not shown) were obtained for water displacing air from the bottom of the column during rewetting.

Average relative saturations for the neutron radiography images were computed by averaging all of the S_{ij} values within the region of interest (ROI) indicated by the rectangle in Fig. 3-4. This ROI was selected to maximize the column area available for averaging while excluding any edge effects and surface variations. The resulting average relative saturations showed very good agreement with those obtained volumetrically from the hanging water column experimental data (Figure 3-2c). Notice, however, that there is a slight tendency for the neutron imaging to overestimate at low relative saturations.

The VG equation was fitted to the drying and wetting *S* curves simultaneously for both the neutron imaging data (average values) and the hanging water content data (all replicate measurements pooled). In both cases rapid convergence was achieved according to the SAS default criterion. The RMSEs for the neutron radiography and hanging water column fits were 0.027 and 0.063, respectively. The R^2 values obtained between the predicted and observed data points (shown in Fig. 3-6) were 0.994 and 0.973 for the neutron radiography and hanging water column data sets, respectively. The resulting VG parameter estimates are given in Table 3-2 along with their approximate 95% confidence intervals. Both datasets revealed significant differences in the α and n parameters due to hysteresis; α was lower and n was higher for drying than for wetting. Statistically, there were no significant differences between any of the VG parameter estimates between the neutron radiography and hanging water column methods. The worst correspondence was observed between the S_r estimates for the two different methods (0.019 versus 0.057 for the hanging water column and neutron radiography methods, respectively). The relatively large confidence band around the radiography estimate of S_r can be attributed to the sparsity of data at very negative matric potentials in the unreplicated neutron imaging experiment compared with the replicated hanging water column experiments (Fig. 3-6). Additional measurements at

the dry end in future neutron imaging experiments will probably resolve this discrepancy.

Based on statistical comparison of the mean VG parameter values from the individual fits with the single VG parameter estimates from the neutron imaging data using one-sample *t*-tests, there were no significant differences at $P < 0.05$ between the neutron radiography and hanging water column methods for any of the VG parameter estimates. Our results indicate that the neutron imaging technique fully reproduces the hysteretic characteristics of this material and can be confidently utilized to quantify average relative saturations. The real benefit of using neutron imaging, however, is its ability to see into the “black box” of the mineral matrix and to quantify soil hydraulic properties on a point (or pixel-by-pixel) basis. Neutron imaging of a range of natural soils would also be beneficial to the soil science community; such an application, however, will require additional detailed calibrations to account for the presence of H in organic matter.

4. Conclusions

We have presented a methodology for using neutron radiography to quantify relative saturations in a coarse-grained silica sand (Flint no. 13). Extension of this nondestructive testing method to porous media with significant organic matter will require additional calibrations to account for the presence of H in the organic matter. The method was applied to measure soil water retention curves under quasi-equilibrium drying and wetting conditions. Normalizing the acquired neutron images relative to the open beam pixel field tended to systematically overestimate water contents due to the small attenuation produced by the silica sand. These overestimations were removed by subtracting the oven-dry pixel field from the water content fields. In addition, scattering anomalies at high water contents were eliminated by dividing the corrected drying and wetting water content fields by the corrected fields at saturation and satiation, respectively. Averaging the resulting relative saturation values for each imposed matric

potential produced an approximate 1:1 relationship with average relative saturations measured volumetrically using the hanging water column method.

The van Genuchten equation provided an excellent fit to both of the average relative saturation data sets. The Flint no. 13 sand exhibited pronounced hysteresis, with values of the α and *n* VG parameters for the main drying branch approximately half and twice the magnitude, respectively, of those for the main wetting branch. There were no statistical differences between the VG parameters estimated by the two different methods, indicating that neutron imaging is a reliable method for determining the average soil water retention curve. Additionally, neutron imaging can be used to investigate small-scale local variations in hydraulic properties within a soil column. This topic will be the subject of a future study.

Acknowledgements

This Research was financially supported by the Laboratory Directed Research and Development (LDRD) Program of Oak Ridge National Laboratory and the Joint Directed Research and Development (JDRD) Program of the University of Tennessee UT-ORNL Science Alliance. The authors thank Keely Willis of the University of Wisconsin-Madison for her contributions made at the early stage of the image analyses. The authors acknowledge the support of the National Institute of Standards and Technology, U.S. Department of Commerce, in providing the neutron research facilities used in this work.

References

Al-Yahyai, R., B. Schaffer, F.S. Davies, and R. Muñoz-Carpena. 2006. Characterization of soil water retention of a very gravelly loam soil varied with determination method. Soil Science. Lippincott Williams & Wilkins, Inc. 85-93.

Anderson, I.S., R. McGreevy, and H. Bilheux. 2009. Neutron Imaging and Applications: A Reference for the Imaging Community. Springer, New York.

Andreu, L., J.W. Hopmans, and L.J. Schwankl. 1997. Spatial and temporal distribution of soil water balance for a drip-irrigated almond tree. Agricultural Water Management, 35: 123-146.

Bayer, A., H.-J. Vogel, and K. Roth. 2004. Direct measurement of the soil water retention curve using X-ray absorption. Hydrolog and Earth System Sciences, 8(1): 2-7.

Bazylak A. 2009. Liquid water visualization in PEM fuel cells: A review. International Journal of Hydrogen Energy, 34(9):3845-3857.

Belcher, D.J., T.R. Cuykendall, and H.S. Sack. 1950. The measurement of soil moisture and density by neutron and gamma-ray scattering. Civil Aero. Adm. Tech. Dev. Rept. 127. Washtington D.C.

Berger, H. 1971. Neutron Radiography. Annual Review of Nuclear Science, 21:335-364.

Chanasyk, D.S. and M.A. Naeth. 1996. Field measurement of soil moisture using neutron probes. Canadian Journal of Soil Science, 76(3): 317-323.

Chaouki J., Larachi F., Dudukovic M.P. 1997. Noninvasive tomographic and velocimetric monitoring of multiphase flow. Industrial & Engineering Chemistry Research, 36 (11): 4476-4503.

Chen, Q. and B.J. Balcom. 2005. Measurement of rock-core capillary pressure curves using a single-speed centrifuge and one-dimensional magnetic-resonance imaging. Journal of Chemical Physics, 122 (21): 214720-214727.

Cnudde, V., M. Dierick, J. Vlassenbroeck, B. Masschaele, E. Lehmann, P. Jacobs, and L. Van Hoorebeke. 2008. High-speed neutron radiography for monitoring the water absorption by capillarity in porous materials: Nuclear Instruments and Methods in

Physics Research, Section B: Beam Interactions with Materials and Atoms, 266(1): 155–163. doi: 10.1016/ j.nimb.2007.10.030.

Dane, J.H., and J.W. Hopmans. 2002. Hanging water column, in Methods of Soil Analysis, part 4, Physical Methods, edited by J. H. Dane and G. C. Topp, pp. 680–683, Soil Science Society of America, Madison, Wis.

Dane, J.H., M. Oostrom, and B.C. Missildine. 1992. An improved method for the determination of capillary pressure-saturation curves involving TCE, water and air, Journal of Contaminant Hydrology, 11: 69–81.

Deinert, M.R., J.-Y. Parlange, T. Steenhuis, J. Throop, K. Ünlü, and K.B. Cady. 2004. Measurement of fluid contents and wetting front profiles by real-time neutron radiography, Journal of Hydrology, 290 (): 192-201.

El Abd, A., A. Czachor, and J. Milczarek. 2009. Neutron radiography determination of water diffusivity in fired clay brick. Applied Radiation and Isotopes, 67(4): 556-559.

Gardner, W. and D. Kirkham. 1952. Determination of soil moisture by neutron Scattering. Soil Science 73(5): 391-402.

Hassanein, R., E. Lehmann, and P. Vontobel. 2005. Methods of scattering corrections for quantitative neutron radiography. Nuclear instruments and methods in physics research section A. 542: 353-360.

Hassanein, R., H.O. Meyer, A. Carminati, M. Estermann, E. Lehmann, and P. Vontobel. 2006a. Investigation of water imbibitions in porous stone by thermal neutron radiography. Journal of Physics D: Applied Physics, 39: 4284-4291.

Hassanein, R., F. de Beer, N. Kardjilov, and E. Lehmann. 2006b. Scattering correction algorithm for neutron radiography and tomography tested at facilities with different beam characteristics. Physica B, 385-386 (2): 1194-1196.

Heller, A.K., L. Shi, J.S. Brenizer, and M.M. Mench. 2009. Initial water quantification results using neutron computed tomography. Nucl. Instrum.Methods Phys. Res. A 605:99–102. doi:10.1016/j.nima.2009.01.166

Hincapié, I. and P. Germann. 2009. Gravity-driven viscous flow in sand boxes assessed with neutron radiography. Vadose Zone Journal, 8(4): 891-901.

Hincapié, I. and P. Germann. 2010. Water content wave approach applied to neutron radiographs of finger flow. Vadose Zone Journal, 9(2): 278-284.

Hussey, D.S., D.L. Jacobson, K.J. Coakley, D.F. Vecchia and M. Arif. 2010. In situ fuel cell water metrology at the NIST-NCNR neutron imaging facility. Journal of Fuel Cell Science and Technology, 7(2): 22-22.

Kim, F., D. Penumadu and D.S. Hussey. 2011. Water distribution variation in partially saturated granular materials using neutron imaging. Journal of Geotechnical & Geoenvironmental Engineering, doi:10.1061/(ASCE)GT.1943-5606.0000583.

Lewis, J.T., and E.L. Krinitzsky. 1976. Neutron radiation in the study of soil and rock. In: H. Berger (editor) Practicial applications of neutron radiography and gaging. ASTM STP 586. Am. Soc. Testing Mat., W. Conshohocken, PA. p. 241–251.

Mukundan, R. and R.L. Borup. 2009. Visualizing liquid water in PEM fuel cells using neutron imaging. Fuel Cells, 9(5): 499-505.

Oswald, S.E., M. Menon, A. Carminati, P. Vontobel, E. Lehmann, and R. Schulin. 2008. Quantitative imaging of infiltration, root growth, and root water uptake via neutron radiography. Vadose Zone Journal. 7(3): 1035-1047. doi: 10.2136/vzj2007.0156.

Reynolds, W.D., and D.E. Elrick. 2002. Constant head soil core (tank) method. p. 804-808 in J.H. Dane and G. Clarke Topp (eds.), Methods of Soil Analysis, Part 4: Physical Methods. Soil SSSAJ Book Series 5, Science Society of America, Inc. Madison, WI.

Riley, G.V. and D.S. Hussey. 2010. In situ neutron imaging of alkaline and lithium batteries. Electrochemical Society Transactions, 25(35): 75-83.

Schmugge, T.J., T.J. Jackson, andH.L, McKim. l980. Survey of methods for soil moisture determination. Water Resources Research 16: 961-919.

Strobl, M., I. Manke, N. Kardjilov, A. Hilger, M. Dawson, and J. Banhart. 2009. Topical Review: Advances in neutron radiography and tomography. Journal of Physics D: Applied Physics, 42(24): 243001.

Trabold, T.A., J.P. Owejan, J.J. Gagliardo, D.L. Jacobson, D.S. Hussey, and M. Arif. 2009. Use of neutron imaging for proton exchange membrane fule cell (PEMFC) performance analysis and design. Handbook of Fuel Cells-Fundamentals, Technology and Applications, Chapter 44, Wiley and Sons.

Tumlinson, L.G., H. Liu, W.K. Silk, and J.W. Hopmans. 2008. Thermal neutron computed tomography of soil water and plant roots. Soil Science Society of America Journal. 72: 1234-1242.

U.S. Silica Company. 2009. Product Data Sheet: Whole Grain Silica. Berkeley Springs, WV.

Vasin, M., P. Lehmann, A. Kaestner, R. Hassanein, W. Nowak, R. Helmig, and I. Neuweiler. 2008. Drainage in heterogeneous sand columns with diff erent geometric structures. Adv. Water Resour. 31: 1205–1220. doi:10.1016/j. advwatres.2008.01.004

van Genuchten, M. T. 1980. A closed form equation for predicting the hydraulic conductivity of unsaturated soils. Soil Science Society of America Journal, 44: 892-898.

Appendix C

Table 3- 1 Saturated (drying) and satiated (wetting) volumetric water contents measured by the hanging water column and neutron imaging methods.

Method	Saturated θ				Satiated θ			
	n	L95%	$\bar{X}$	U95%	n	L95%	$\bar{X}$	U95 %
Hanging Water Column	5	0.332	0.341	0.351	3	0.269	0.312	0.355
Neutron Imaging	$1.7x10^6$	0.365	0.366	0.366	$1.7x10^6$	0.321	0.321	0.322
Neutron Imaging (Corrected)	$1.7x10^6$	0.311	0.312	0.313	$1.7x10^6$	0.269	0.270	0.271

Note: n=number of observations, L95%=lower 95% confidence internal, $\bar{X}$ =mean, U95%=upper 95% confidence internal.

Table 3- 2 van Genuchten (1980) equation parameter estimates for the two methods.

Parameter Estimates	Hanging Water Column	95% C.I.		Neutron Imaging	95% C.I.	
		Lower	Upper		Lower	Upper
S_r	0.019	-0.027	0.065	0.057	-0.018	0.131
α (wetting), cm^{-1}	0.097	0.089	0.105	0.089	0.082	0.096
n (wetting)	4.366	3.535	5.197	4.276	3.440	5.111
α (drying), cm^{-1}	0.053	0.051	0.054	0.050	0.048	0.051
n (drying)	8.127	6.829	9.426	9.010	7.283	10.737

Note: S_r, residual saturation; α, parameter inversely related to the air- or water-entry values; *n*, shape parameter influenced by the pore-size distribution; C.I., Confidence Interval

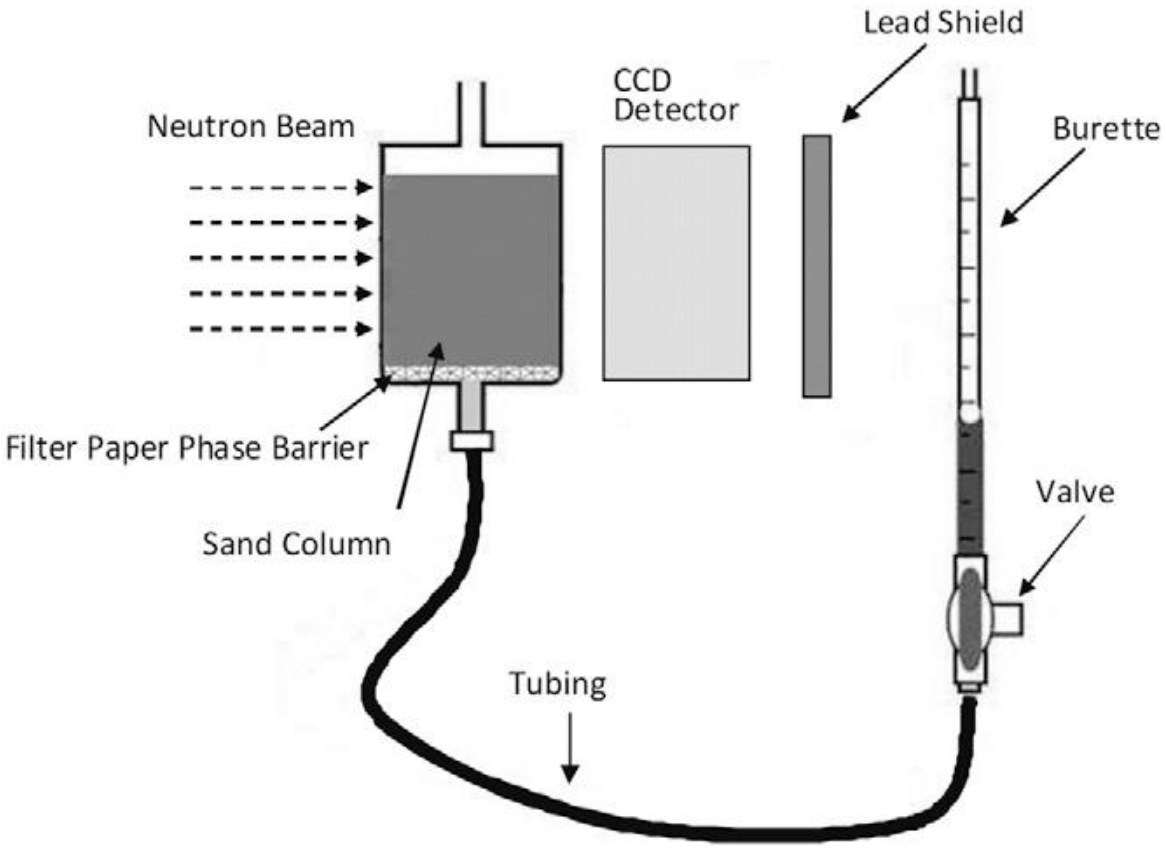

Figure 3- 1 Schematic diagram in cross-section of the experimental setup at the NIST-NCNR beamline (not to scale).

Figure 3- 2 Comparison of data from the neutron imaging and hanging water column experiments: (a) average water contents <θ>, (b) average water contents with neutron data corrected based on oven-dried sample, and (c) average relative saturations <*S*>. In all three cases, the 95% confidence intervals for individual points are not shown because they were smaller than the symbols used. Dashed line is the 1:1 relationship (closed circle: drying, open circle: wetting).

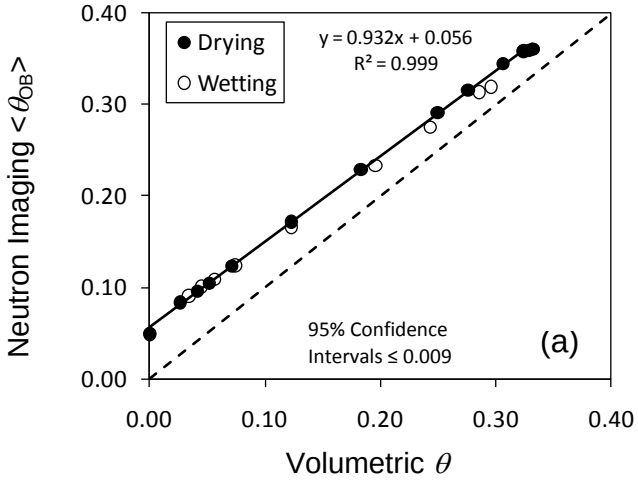
Drying
Wetting
y = 0.932x + 0.056
R² = 0.999
95% Confidence
Intervals ≤ 0.009
(a)
Neutron Imaging <θOB>
Volumetric θ
0.00
0.10
0.20
0.30
0.40

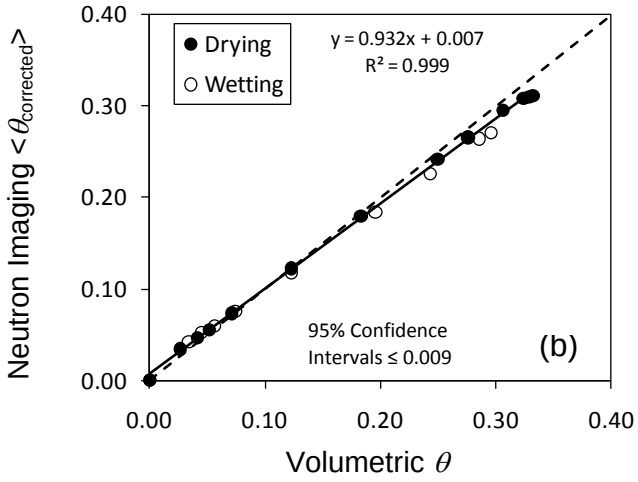
Drying
Wetting
y = 0.932x + 0.007
R² = 0.999
95% Confidence
Intervals ≤ 0.009
(b)
Neutron Imaging <θcorrected>
Volumetric θ
0.00
0.10
0.20
0.30
0.40

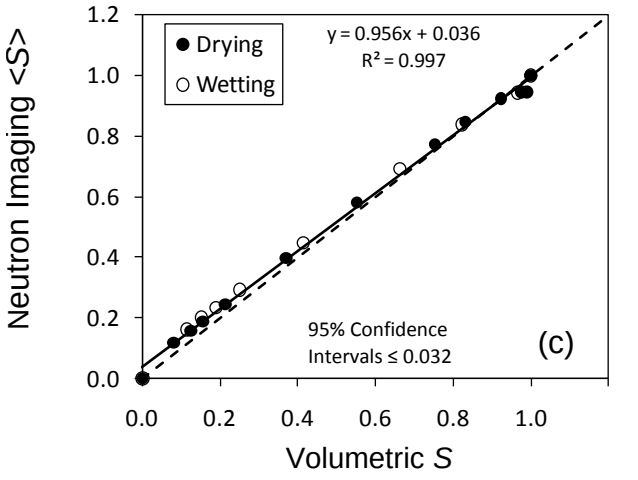
Drying
Wetting
y = 0.956x + 0.036
R² = 0.997
95% Confidence
Intervals ≤ 0.032
(c)
Neutron Imaging <S>
Volumetric S
0.0
0.2
0.4
0.6
0.8
1.0
1.2

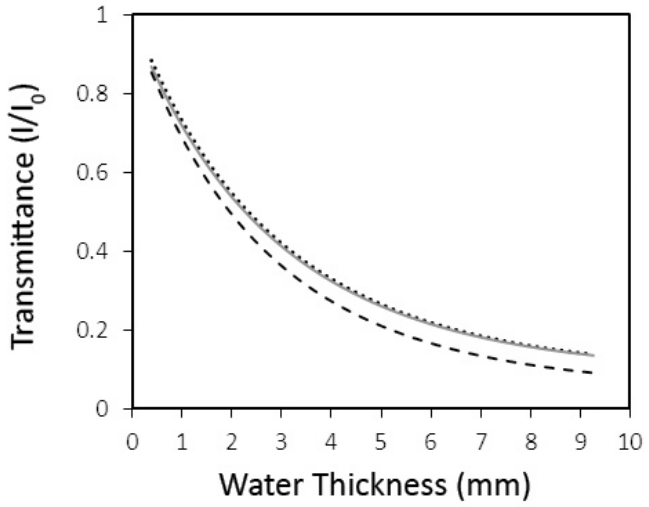

Figure 3- 3 Transmittance as a function of column thickness predicted using the attenuation coefficients for water, silica sand, and aluminum in Eqs. [1] and [3]. (dotted line: water; gray line: water and Al; dashed line: water, Al, and silica sand).

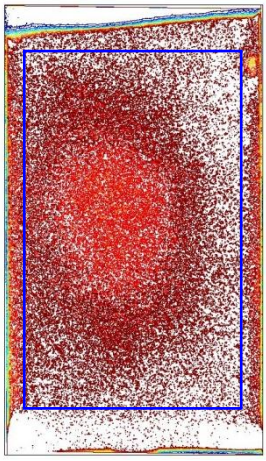

Figure 3- 4 Contour map of corrected volumetric water contents at saturation showing the effects of scattering in the center of the column. The superimposed rectangle designates the region of interest (ROI) used for averaging each image at different matric potentials.

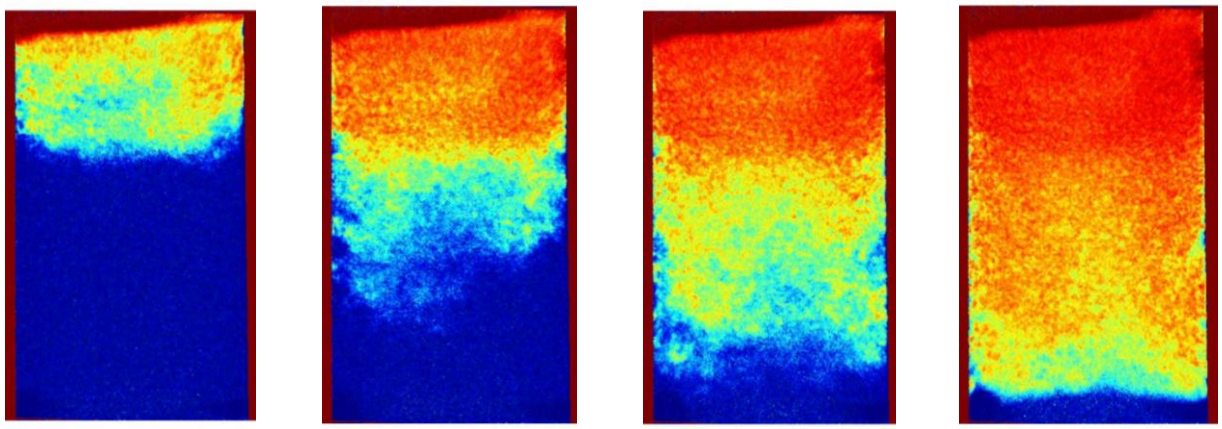

(a) (b) (c) (d)

Figure 3- 5 Relative saturation images (1 = blue, 0 = red) for basal matric potentials of (a) -15.61 cm, (b) -18.47 cm, (c) -20.37 cm, and (d) -21.80 cm in a drying sequence. Note that the filter paper phase barrier at the bottom of sand column remains fully saturated throughout the drainage process.

Figure 3- 6 Measured average relative saturation values (closed circle: drying, open circle: wetting) and fitted van Genuchten (1980) functions (solid line: drying, dashed line: wetting) for (a) the hanging water column experiments (data for all replicates pooled) and (b) the unreplicated neutron imaging experiments. The 95% confidence intervals for individual points are not shown because they were smaller (≤ 0.032) than the symbols used.

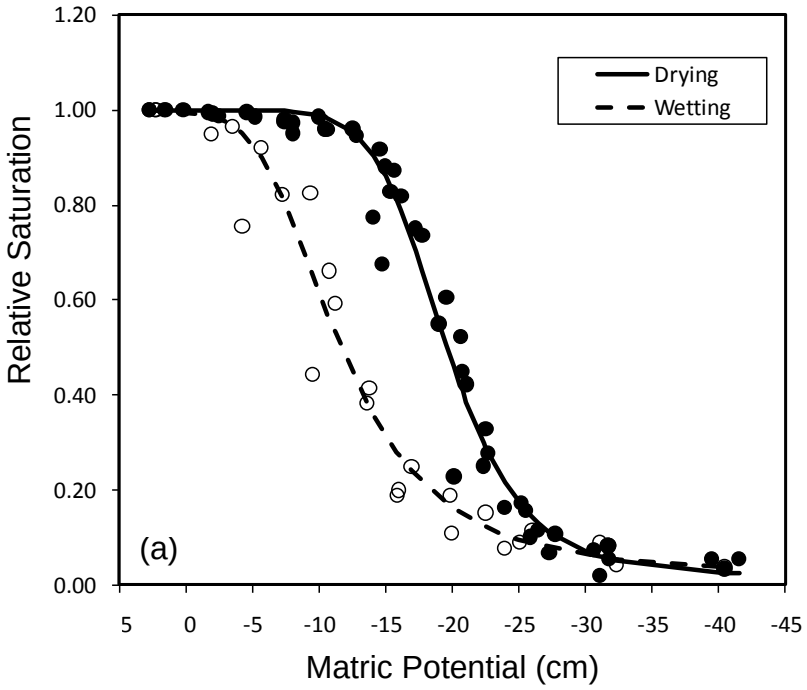
Drying
Wetting
Relative Saturation
1.20
1.00
0.80
0.60
0.40
0.20
0.00
(a)
5
0
-5
-10
-15
-20
-25
-30
-35
-40
-45
Matric Potential (cm)

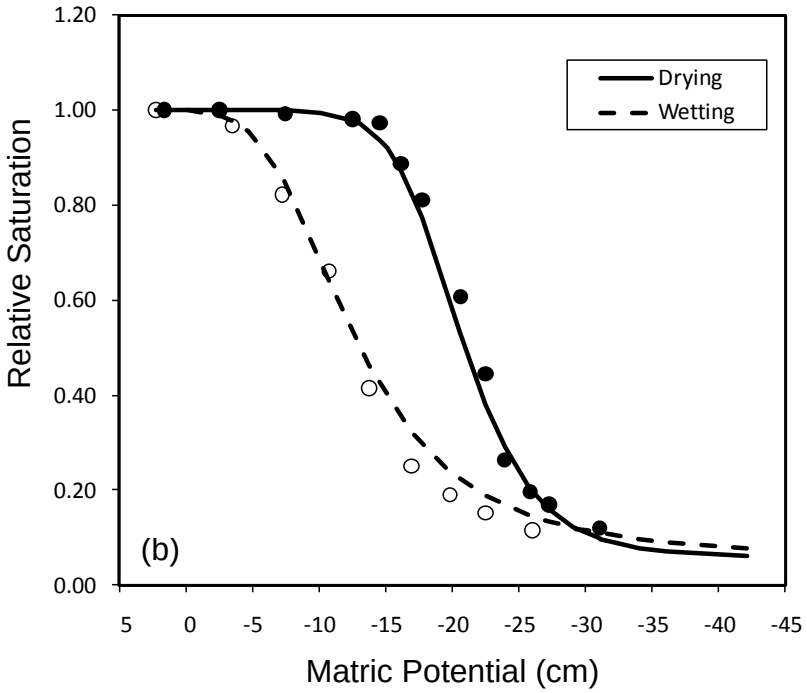
Drying
Wetting
Relative Saturation
1.20
1.00
0.80
0.60
0.40
0.20
0.00
(b)
5
0
-5
-10
-15
-20
-25
-30
-35
-40
-45
Matric Potential (cm)

CHAPTER IV

POINT WATER RETENTION CURVES QUANTIFIED BY NEUTRON RADIOGRAPHY

This chapter is a reformatted version of a paper that will be submitted to Advances in Water Resources in 2013 by Kang et al. Misun Kang participated in the experiments, performed the data analyses, and wrote the paper. Other co-authors contributed to the data acquisition, data analyses, and revision of the manuscript.

Kang M., E. Perfect, C.L. Cheng, H. Z. Billheux, J. Lee, J. Horita, and J.M. Warren. Point Water Retention Curves Quantified by Neutron Radiography, Advances in Water Resources (in preparation).

Abstract

The water retention function is needed for modeling multiphase flow in porous media. Traditional techniques for measuring this function, such as the hanging water column method or pressure cell, yield average water retention curve data which have to be modeled using inverse procedures to extract relevant point parameters. We have developed a technique for directly measuring point water retention curves for a homogeneous porous medium using 2-D neutron radiography. Neutron radiographic images of quasi-equilibrium volumetric water contents at nine imposed basal matric potentials were obtained during monotonic drying of Flint sand at the High Flux Isotope Reactor (HFIR) Cold Guide (CG) 1D beamline at Oak Ridge National Laboratory. All of the images were normalized with respect to the oven dry image. Volumetric water contents were computed on a pixel by pixel basis using an empirical calibration equation after taking into account beam hardening and geometric corrections. Corresponding matric potentials were calculated from the imposed basal matric potential and pixel elevations. Volumetric water content and matric potential data pairs corresponding to 120 selected pixels were used to construct 120 point water retention curves. Each curve was fitted to the Brooks and Corey equation using segmented non-linear regression in SAS. A 98.5% convergence rate was achieved and the four unknown Brooks-Corey parameters were estimated for 115 pixels. A single Brooks and Corey point water retention function was constructed for Flint sand using the median

values of the parameter estimates. This curve corresponded closely with the point Brooks and Corey function inversely extracted from average water retention data using TrueCell. Forward numerical simulations performed using HYDRUS 1-D showed that the cumulative outflows predicted using the point Brooks and Corey functions from both the direct (neutron radiography) and inverse (TrueCell) methods were in good agreement with independent measurements of cumulative outflow measured with a transducer. Our results indicate that neutron radiography can be used to quantify the point water retention of homogeneous materials. Further research will be needed to extend this approach to more heterogeneous materials.

1. Introduction

Experimental techniques such as the hanging water column (Dane and Hopmans, 2002a) and pressure cell apparatus (Dane and Hopmans, 2002b) have been used to measure the soil water retention curve. The data obtained with these methods correspond to the average volumetric water content for the entire soil column rather than the water content at a physical point. This average water retention function has been assumed to be applicable to any physical point in a homogeneous porous medium when the column height is less than 2 cm (Perfect et al., 2004). However, this assumption can be highly inaccurate for coarse-grained materials with low air entry value, tall columns, and fluids with low interfacial tensions because the capillary pressure varies with height within the porous medium. As a result the volumetric water content at any point can deviate significantly from the measured average water content (Dane et al., 1992; Liu and Dane, 1995a; Sakaki and Illangasekare, 2007). Thus, the use of average water retention data without correction can lead to inaccurate estimation of the hydraulic properties of unsaturated porous media (Bottero et al., 2011).

To improve prediction of the hydraulic properties of unsaturated porous media, various computational procedures have been developed to extract the point water retention function from the measured average water retention function. Liu and Dane (1995a,b) developed a computational procedure and a FORTRAN program to account for variations of matric potential and the volumetric fluid content with column height. TrueCell (Jalbert et al., 1999), a Windows interface based on Liu and Dane's (1995b) FORTRAN program, was made available by this group and is widely used to extract Brooks and Corey (1964) point function parameters from the average water retention curve. Schroth et al (1996) developed a numerical correction procedure to obtain corrected parameters of the van Genuchten (1980) equation to account for column height. Peters and Durner (2006) also used the numerical integration approach to take into account the nonlinearity of the vertical water content distribution in a column. Cropper et al. (2011) presented the numerical integral method for determining the point function with a centrifuge for a range of porous media (Berea sandstone, glass beads,

and Hanford sediments) using both the Brooks and Corey (1964) and van Genuchten (1980) equations.

It should be noted that the above “extraction” methods are only as good as the underlying models used to represent the water retention curve and drainage process. Direct measurements of the point water retention curve are needed to provide model inputs and to evaluate the performance of these inverse procedures. Sakaki and Illangasekare (2007) successfully compared the Brooks and Corey parameters obtained by TrueCell with those from data obtained by time domain reflectometry (TDR) at the midpoint of sample height in nine columns of sandy materials. Gamma beam attenuation (Dane et al., 1992), magnetic resonance imaging (MRI) (Chen and Balcom, 2005), and X-ray computed tomography (CT) (Bayer et al., 2004) have also been used to determine point water retention curves for air displacing water in porous media.

Neutron imaging is a particularly powerful tool with respect to soil water due to its transparency to heavy elements and high sensitivity to the hydrogen in water. Neutron imaging was first applied to visualize water in soil in two dimensions by Lewis and Krinitzsky (1976). Since then neutron imaging has been employed to study both the statics (Lopes et al., 1999; Lehmann et al. 2006; Tumlinson et al., 2008; Kim et al., 2011; Cheng et al. 2012) and dynamics (Clarke et al., 1987; Tullis, 1994; Hincapie and Germann, 2010; Deinert et al., 2004; Carminati et al., 2009; Shokri et al., 2008; Lehmann and Or, 2009) of soil water, either in two dimensions (radiography) or three dimensions (tomography), mostly using thermal neutrons. Papafotiou et al. (2008) quantified the 3-D distribution of water in structured porous media after two successive drainage steps and tested the ability of neutron and synchrotron tomography to determine average hydraulic properties using numerical simulations. Schaap et al. (2008) carried out neutron tomography to map temporal changes in the water content distribution using an artificial heterogeneous medium to analyze the effect of connectivity on water flow during two drainage-wetting cycles. Vasin et al. (2008) tested the influence of packing structures on the movement of water in two heterogeneously packed sand columns during multi-step drainage and assessed the quality of an upscaled model. However, neutron radiography does not appear to have been previously applied to directly measure point water retention functions.

In previous studies (Cheng et al., 2012; Kang et al., 2013), we have demonstrated that neutron imaging is a very effective tool for quantifying water in porous media and determining the average water retention curve. The water content estimates from neutron imaging showed good agreement with experimental data measured independently by the hanging water column method. The van Genuchten equation provided a good fit to the average water retention data sets from neutron imaging and the hanging water column method. We propose that neutron radiography can also be an effective tool to show the spatial distribution of water in a soil column and to determine point water retention functions. The main objectives of this study were to: directly determine the point water retention curve using neutron radiography; compare the measured point water retention curve with the point retention curve obtained by inverse modeling of the average water retention curve data using TrueCell; compare the cumulative outflow numerically simulated by HYDRUS 1-D (Šimůnek et al., 1998) using Brooks and Corey parameters obtained from both direct measurement and inverse modeling with independent transducer data.

2. Materials and Methods

Hanging Water Column Set-Up

Flint sand (Flint #13, U.S. Silica Company, Berkeley Springs, WV) was used as the homogeneous porous medium. Flint sand is mainly composed of quartz (99.8 %) with grain diameters ranging from 0.11 mm to 0.60 mm, a median grain diameter of 0.56 mm, and the particle density of 2.65 g cm^{-3} (U.S. Silica Company, 2009). The saturated hydraulic conductivity, determined using the constant-head method implemented without a water tank is 1.66×10^{-4} m s^{-1} ± 0.32×10^{-4} m s^{-1} (Reynolds and Elrick, 2002).

To set up the hanging water column an outlet at the base of a cylindrical Al container (inner diameter: 2.56 cm, height: 10 cm) was connected via Tygon tubing to a burette filled with distilled water. A pressure transducer (PX409USB, Omega®, Manchester, UK) was attached to the burette to record water level changes in the burette every second. The bottom of the Al container was covered with several layers of

moist Whatman #4 filter paper after removing any air bubbles in the hanging water column by suction. The 50 g of oven-dried sand was then incrementally moist-packed into the Al container up to 5.6 (± 0.1) cm and the sand columns were fully-saturated overnight prior to the experiment. The bulk density (= mass of dry sand/total volume of packed sand column) was 1.74 (± 0.03) g/cm^3 and the porosity (=1-bulk density/particle density), of the packed sand column was 0.34 (± 0.01). A pre-saturated Flint sand column sample, connected to a hanging water column, was set up at the HFIR CG 1-D beamline. At the facility, the top of the Al container was attached to the sample holder while allowing air to flow into the Al container through small holes. The sample was placed 24 cm away from the detector to minimize the scattering effect due to the initial high water content of the sample.

Neutron Radiography

Neutron imaging was performed using cold neutrons at the High Flux Isotope Reactor (HFIR) Cold Guide (CG) 1-D beam line at Oak Ridge National Laboratory. Neutron attenuation by the sample was detected with a 25 μm LiF/ZnS scintillator and a charge coupled device (CCD) camera system (iKon-L 936, Andor Technology plc. Belfast, UK). The resulting field of view was ~ 7 × 7 cm with image resolution ~75 μm per pixel. The ratio of the distance between the aperture and the detector to its aperture diameter (the L/D ratio) was 625 and the neutron flux was 5×10^5 cm^{-2}s^{-1}.

The sand column was subsequently drained stepwise under quasi-equilibrium conditions by adjusting the height of the hanging water column outside of the beamline to give various basal matric potential values of -2.1 cm, -8.0 cm, -11.8 cm, -15.0 cm, -16.6 cm, -18.3 cm, -20.8 cm, -25.3 cm, and -46.7 cm. Radiographic images were acquired at each quasi-equilibrium state during the drainage process with an exposure time of 60 s. Photographs of the experimental set up are shown in Fig. 4-1[4]. The oven-dry Flint sand sample in the Al container was also imaged later for normalization.

[4] Note: All tables and figures are located in Appendix D.

Replicate experiments were not possible because of the limited amount of beam time available for the experiment.

Image Analysis

All image processing and quantitative analyses were performed using the MATLAB (Version 7.11, R2010b-SP1, Mathworks, Inc., 2011) and ImageJ (Version 1.43m, National Institutes of Health, 2009) software packages. The collected raw images were normalized with respect to reference images of the open beam and dark field to correct for background noises, inhomogeneities in the beam and detector, and fluctuations in the neutron flux. The normalized images were despeckled using a median filter (5 pixels × 5 pixels) to remove bright pixels mainly due to scattered γ-rays. All of the normalized wet images were then divided by the normalized oven dry image to measure the water thickness of the sample. Details of image processing procedures for neutron radiography are given by Kang et al. (2013).

The water thickness of each pixel in the neutron radiographs of the sample was calculated using following empirical equation:

$$\tau_{(i,j)} = -\frac{\Sigma}{2\beta} - \sqrt{\left(\frac{\Sigma}{2\beta}\right)^2 - \frac{1}{\beta}\ln\left(\frac{I_{wet}}{I_{dry}}\right)_{(i,j)}} \quad [1]$$

where, $\tau_{(i,j)}$ is water thickness in cm, Σ = 5.542 cm^{-1}, β = -2.140 cm^{-2}, and I_{wet} and I_{dry} are the normalized wet and dry images, respectively. The attenuation coefficient Σ and correction coefficient β were previously obtained at HFIR CG 1-D and the water thicknesses of all the calibration data were predicted with an accuracy of $\pm$ 0.022 cm (Kang et al., 2013).

To compute the volumetric water content (θ_{ij}, cm^3cm^{-3}) at a pixel(i,j) from neutron radiography of a cylindrical container, the measured water thickness was divided by the beam path length (C_{ij}) , which is the chord length for a circle:

$$\theta_{ij} = \frac{\tau_{ij}}{C_{ij}} \times \frac{pixel\ area}{pixel\ area} = \frac{\tau_{ij}}{C_{ij}} \quad [2]$$

where $C_{ij} = 2\sqrt{r^2 - a_{(i,j)}^2}$, r is the radius of the sand column (cm), and $a_{(i,j)}$ is the distance from the center of the column to the pixel (i, j) (cm).

Construction of Point and Average Water Retention Curves

A grid of 120 points (pixels) was superimposed on the images (Fig. 4-2), and the individual volumetric water content values (θ_{ij}) at these locations were combined with information on the known distribution of matric potential (ψ) within the sample to give point water retention curves for 120 selected locations. Figure 4-3 shows selected volumetric water content images (882 x 1898 pixels) during drainage of Flint sand at basal matric potentials of -8 cm, -11.8 cm, -15.0 cm, -16.6 cm, -18.3 cm, -20.8 cm, and -46.7 cm for 4 example pixel locations, (100,400), (100, 800), (100, 1200), and (100, 1600), out of the 120 points analyzed. To construct the point water retention curve, the volumetric water content was measured for each point using equation [2]. The absolute value of matric potential of each point was calculated by adding the height of the pixel to the absolute value of basal matric potential as shown in Fig. 4-3a. Volumetric water contents for the different pixel locations were then plotted as functions of their matric potentials to construct 120 point water retention curves. Figure 4-3b shows point water retention data for the four example locations (4.3 cm, 3.1 cm, 1.8 cm, and 0.6 cm height above the phase barrier).

In order to obtain the average volumetric water content ($< \theta >$) for each matric potential applied, the individual θ_{ij} values from the neutron radiographs were arithmetically averaged over the imaged area:

$$< \theta > = \frac{\sum_1^n \theta_{ij}}{n} \qquad [3]$$

where n is the total number of pixels within the region of interest (ROI) indicated by the rectangle in Fig. 4-2. This ROI was selected to maximize the column area available for averaging while excluding any edge effects and surface variations.

Parameterization of Point Water Retention Data

The point water retention data were parameterized by fitting the Brooks and Corey, BC, equation (Brooks and Corey, 1964). The Brooks and Corey (1964) equation is particularly applicable to point data because it includes a distinct air entry value (Cropper et al., 2011). The Brooks and Corey equation is given by:

$$\theta = \theta_s \qquad 0 > \psi \geq \psi_a$$
$$\theta = \theta_r + (\theta_s - \theta_r) \times \left[\frac{\psi_a}{\psi}\right]^{\lambda} \qquad \psi < \psi_a \qquad [4]$$

where θ (cm^3cm^{-3}) is volumetric water content, θ_s (cm^3cm^{-3}) is the saturated volumetric water content, θ_r (cm^3cm^{-3}) is the residual volumetric water content, and ψ_a (cm) is the air-entry value, and λ (dimensionless) is the pore-size distribution index.

Equation [4] was fitted to the 120 point water retention data sets using segmented non-linear regression (Marquardt method) in SAS 9.2 (SAS Institute Inc., Cary, NC). An example fit for parameterization using directly measured point water retention data at a physical point, (100, 800), is shown in Fig. 4-4. The estimated values of θ_s, θ_r, ψ_a, and λ from this fit were 0.33, 0.02, 17.95, and 9.76, respectively. The R^2 value for this fit was 0.993. All of the fits converged successfully except for 5 pixels which were excluded from the remaining analyses. The goodness of fit was assessed based on the root mean square error (RMSE) and by linear regression of the observed and predicted θ values to give a coefficient of determination (R^2). The Brooks-Corey parameters for the 115 converged fits were summarized using histograms, and their median and mean values were computed. Hereafter the median and mean values of the directly obtained point Brooks-Corey parameters are referred to as “median_DP” and “mean_DP”, respectively.

A point water retention function was also extracted by inverse modeling the average water retention curve data. TrueCell (Jalbert et al., 1999), a Windows interface based on Liu and Dane’s (1995b) FORTRAN program, was employed to inversely extract Brooks-Corey point parameters from the average water retention data. TrueCell uses inputs of column configuration and the density of the non-wetting and wetting fluids

to take into consideration the vertical variation in matric potential and volumetric water content within a column in order to establish the relationship between the average and point retention functions, i.e.

$$|\psi| = |<\psi>| + z_n \frac{\rho_n}{\rho_w} - z_w + \left(1 - \frac{\rho_n}{\rho_w}\right) z$$
$$|<\theta>| = \frac{1}{z_c} \int_0^{z_c} \theta(|\psi|) dz \quad [5]$$

where $<\psi>$ (cm) is the average matric potential, $<\theta>$ ($cm^3 cm^{-3}$) is the height averaged volumetric water content, ψ (cm) is the point matric potential, θ ($cm^3 cm^{-3}$) is the point volumetric water content, z_n (cm) and z_w (cm) are the heights where the pressures of the non-wetting (i.e., air) and wetting (i.e., water) fluids are measured, respectively, z (cm) is the height at a point, z_c (cm) is the column height, and ρ_n (gcm^{-3}) and ρ_w (gcm^{-3}) are the densities of the non-wetting and wetting fluids, respectively. For this particular fitting, z_c = 5.4 cm, z_w = 2.7 cm, z_n = 5.4 cm, ρ_n =1 gcm^{-3}, and ρ_n = 0 gcm^{-3}. TrueCell produced one set of point Brooks and Corey parameter estimates using the average water retention data.

HYDRUS 1-D Numerical Simulation

HYDRUS 1-D (Šimůnek et al., 1998), a Windows-based software for simulating water flow and solute transport in one-dimensional variably saturated soils using numerical solutions, was used for the forward numerical simulation of the cumulative outflow of water from Flint sand in response to step changes in applied pressure. The mean and median values of the 115 Brooks-Corey parameters were used as inputs to the numerical model. The point parameters extracted by TrueCell were also used to simulate the cumulative outflow of Flint sand. The predicted cumulative outflows using the three sets of point parameters were then compared with the cumulative outflow independently measured with the pressure transducer.

3. Results and Discussion

2-D neutron radiographic images of quasi-equilibrium volumetric water contents at nine imposed basal matric potential were obtained during monotonic drying of Flint sand at the HFIR CG1-D beamline. 120 point water retention data sets were obtained from these images as described earlier. The Brooks and Corey (1964) equation was fitted to each data set using segmented non-linear regression in SAS. 98.5% of the fits converged successfully yielding 115 sets of the four Brooks and Corey parameters. The RMSE of the fits ranged from 0.005 to 0.078 cm^3cm^{-3} while the R^2 values were between 0.860 and 0.999. The median (and mean) RMSE and R^2 values were 0.019 (0.024) and 0.985 (0.975), respectively. The parameter estimates from the converged fits were summarized using histograms (Fig.4-5). The histograms show considerable meso-scale variability within this homogenous sand column possibly due to differences in local porosity, connectivity of pores, and pore-size distribution caused by the packing procedure employed. The θ_s parameter exhibited the greatest variation. The frequency distribution for θ_s is clearly positively skewed, with a few very high estimates of θ_s. This is perhaps not surprising since θ_s is likely to be quite sensitive to packing and surface and edge effects. Furthermore, it represents an estimate of the water content at saturation, which is the condition that is least accurately measured by the neutron imaging method (Cheng et al., 2012; Kang et al., 2013). The fitted values of θ_s, θ_r, ψ_a, and λ ranged between 0.303-0.550 cm^3cm^{-3}, 0.000-0.061 cm^3cm^{-3}, 14.501-19.099 cm, and 3.549-7.586, respectively. The median and mean values of the 115 sets of point Brooks-Corey parameters were calculated, and are given in Table 4-1.

Another set of fitted BC point parameters was obtained from the average water retention data using TrueCell (Liu and Dane, 1995; Jalbert et al., 1999). Fig. 4-6 shows the observed and best fit points for the average water retention curve, as well as the extracted point water retention curve. The RMSE and R^2 values for this fit were 0.013 and 0.997, respectively. The resulting point Brooks-Corey parameters were 0.364 cm^3cm^{-3}, 0.025 cm^3cm^{-3}, 17.250 cm, and 6.649 for θ_s, θ_r, ψ_a, and λ, respectively (Table 3-1).

Table 4-1 summarizes the point Brooks and Cory parameter estimates determined by both direct neutron radiographic measurement (mean and median values) and by TrueCell inverse modeling. Because of the skewed frequency distributions, particularly for θ_s, the median value parameters were closer to the TrueCell estimates than the mean values. This effect can be seen in Fig. 4-7 in which the point retention curve constructed using the median_DP showed excellent agreement with the point retention curve of TrueCell, while the mean_DP curve resulted in an overestimation of θ prior to air entry.

The HYDRUS1-D forward numerical simulations of drainage in Flint sand due to step changes in applied pressure using the three sets of Brooks-Corey parameters, TrueCell, median_DP, and mean_DP, are shown in Fig. 4-8. The cumulative outflow predicted by HYDRUS using these different parameters were compared with the independent transducer data. RMSE values for TrueCell, median_DP, and mean_DP relative to the transducer data were 0.091, 0.091, and 0.126 cm, respectively. The number of observations for cumulative outflow was 18,379 in each case. Although there were some systematic discrepancies between the results predicted using the point parameters and the transducer data, in general, the predicted steps in outflow responsed similarly to those measured by the transducer. It is also clear that that the median_DP result is closer to the transducer data than that of the mean_DP prediction due to the skewed nature of some of the histograms for the point Brooks-Corey parameters (Fig. 4-5).

4. Conclusions

Point water retention functions for Flint sand were directly determined using quantitative neutron radiography. The Brooks and Corey model provided a good fit to the point water retention data obtained by neutron radiography.

The median Brooks-Corey parameters, estimated by fitting the directly measured 115 point water retention curves, compared favorably with those extracted from the average water retention curve using TrueCell. HYDRUS 1-D forward numerical

simulations showed that the predicted cumulative outflows using point parameters obtained by both direct and inverse methods were in good agreement with independently measured transducer data.

Neutron imaging shows considerable promise as a non-destructive method for investigating small scale variations in hydraulic properties within a soil column. The advantage of using neutron radiography for measuring the point retention function is that multiple point curves are obtained for a single sample. Our results suggest that meso-scale variations occur in this hydraulic property, even for a homogenous material. Further research is needed for integrating these variations in order to predict an average water retention curve at the column scale, especially in the case of layered and heterogeneous materials.

Acknowledgements

This Research was supported by the Laboratory Directed Research and Development (LDRD) Program of Oak Ridge National Laboratory and the Joint Directed Research and Development (JDRD) Program of the University of Tennessee UT-ORNL Science Alliance. The Authors thank Sophie Voisin at ORNL for her contributions to the development of MATLAB code. The Authors are also thankful for contributions from HFIR support groups, Machine Shop, and the Instrument Development Group, Lakeisha Walker, Jaimie Werner, and Brent Taylor. This Research at Oak Ridge National Laboratory's High Flux Isotope Reactor was sponsored by the Scientific User Facilities Division, Office of Basic Energy Sciences, U. S. Department of Energy, which is managed by UT-Battelle, LLC.

References

Bayer, A., H.-J. Vogel, and K. Roth. 2004. Direct measurement of the soil water retention curve using X-ray absorption. Hydrolog and Earth System Sciences, 8(1): 2-7.

Bottero, S., S.M. Hassanizadeh, and P.J. Kleingeld. 2011. From local measurements to an upscaled capillary pressure-saturation curve. Transp. Porous Media 88:271-291.

Brooks, R. H. and A. T. Corey. 1964. Hydraulic properties of porous media. Hydrology Paper #3, Colorado State Univ., Colorado State Univ., Fort Collins, CO.

Carminati , A., and H. Flühler. 2009. Water infiltration and redistribution in soil aggregate packings. Vadose Zone J. 8:150–157. doi:10.2136/vzj2008.0077

Chen, Q. and B.J. Balcom. 2005. Measurement of rock-core capillary pressure curves using a single-speed centrifuge and one-dimensional magnetic-resonance imaging. Journal of Chemical Physics, 122 (21): 214720-214727.

Cheng C.-L., M. Kang, E. Perfect, S. Voisin, J. Horita, H.Z. Bilheux, J.M. Warren, D.L. Jacobson, and D.S. Hussey, 2012. Average soil water retention curves measured by neutron radiography, Soil Sci. Soc. Am. J. 76(4): 1184-1191.

Clarke M. A., Kettle R. J., D'Souza. 1987. Developments in the use of thermal neutron radiography for studying mass transfer in a partially frozen soil. Proceedings of the Second World Conference on Neutron Radiography, Paris, France, June 16–20, 1986, Barton, G.Farny, J. Person, H.RÖttger, D. Reidel, eds. Pub. Co., Dordrecht, Holland 1987. pp. 271–279.

Cropper, S.C., E. Perfect, E.H. van den Berg, and M.A. Mayes. 2011. Comparison of average and point capillary pressure-saturation functions determined by steady-state centrifugation. Soil Sci. Soc. Am. J. 75:17-25

Dane, J.H., and J.W. Hopmans. 2002a. Hanging water column. p. 680–683. In J.H. Dane and G.C. Topp (ed.). Methods of soil analysis. Part 4. Physical methods. SSSA Book Ser. 5. SSSA, Madison, WI.

Dane, J.H., and J.W. Hopmans. 2002b. Pressure plate extractor. p. 688–690. In J.H. Dane and G.C. Topp (ed.). Methods of soil analysis. Part 4. Physical methods. SSSA Book Ser. 5. SSSA, Madison, WI.

Dane, J.H., M. Oostrom, and B.C. Missildine. 1992. An improved method for the determination of capillary pressure-saturation curves involving TCE, water and air, Journal of Contaminant Hydrology, 11: 69–81.

Deinert, M.R., J.-Y. Parlange, T. Steenhuis, J. Throop, K. Ünlü, and K.B. Cady. 2004. Measurement of fluid contents and wetting front profiles by real-time neutron radiography, Journal of Hydrology, 290: 192-201.

Hincapié, I. and P. Germann. 2010. Water content wave approach applied to neutron radiographs of finger flow. Vadose Zone Journal, 9(2): 278-284.

Jalbert, M., J.H. Dane, and J.H. Liu. 1999. TrueCell: Physical point Brooks–Corey parameters using pressure cell data. Users guide for version 1.2. Spec.Rep. Dep. of Agron. and Soils, Auburn Univ., Auburn, AL.

Kang M., H.Z. Bilheux, S. Voisin, C.L. Cheng, E. Perfect, J. Horita, and J.M. Warren,2013. Water calibration measurements for neutron radiography: application to water content quantification in porous media. Nucl. Instr. Meth. Phys. Res. A. DOI: 10.1016/j.nima.2012.12.112.

Kim F., D. Penumadu, and D.S. Hussey. 2011. Water distribution variation in partially saturated granular materials using neutron imaging. Journal of Geotechnical and Geoenvironmental Engineering, doi:10.1061/(ASCE)GT.1943-5606.0000583

Lehmann P., Wyss P., Flisch A., Lehmann E., Vontobel P., Krafczyk M., 2006. Tomographical imaging and mathematical description of porous media used for the prediction of fluid distribution. Vadose Zone J; 5:80–97.

Lehmann P., D. Or D., 2009. Evaporation and capillary coupling across vertical textural contrasts in porous media, Phys. Rev. E 80 (4) 046318

Lewis, J.T. and Krinitzsky, E.E., 1976. Neutron radiation in the study of soil and rock, Berger, H., Editor, "Practical Applications of Neutron Radiography and Gaging," ASTM STP 586, American Society for Testing and Materials, West Conshohocken, PA, 1976., pp. 241-251

Liu, H.H., and J.H. Dane. 1995a. Improved computational procedure for retention relations of immiscible fluids using pressure cells. Soil Sci. Soc. Am. J. 59:1520–1524.

Liu, H.H., and J.H. Dane. 1995b. Computation of the Brooks–Corey parameters at a physical point based on pressure cell data. Spec. Rep. Dep. of Agron.and Soils, Auburn Univ., Auburn, AL.

Lopes, R.T., Bessa, A.P., Braz, D., de Jesus, E.F.O., 1999. Neutron computerized tomography in compacted soil. Appl. Radiat. Isot. 50: 451–458.

http://www.mathworks.com

Papafotiou A., Helmig R., Schaap J., Lehmann P., Kaestner A., Flühler H. 2008. From the pore scale to the lab scale: 3D lab experiment and numerical simulation of drainage in heterogeneous porous media. Adv. Water Resour 31: 1253-1268

Perfect, E., L. D. McKay, S. C. Cropper, S. G. Driese, G. Kammerer, and J. H. Dane (2004), Capillary pressure-saturation relations for saprolite: Scaling with and without correction for column height, Vadose Zone J. 3, 493– 501

Peters, A., and W. Durner. 2006. Improved estimation of soil water retention characteristics from hydrostatic column experiments. Water Resour. Res. 42:W11401, doi:10.1029/2006WR004952.

Reynolds, W.D., and D.E. Elrick. 2002. Constant head soil core (tank) method. p. 804-808 in J.H. Dane and G. Clarke Topp (eds.), Methods of Soil Analysis, Part 4: Physical Methods. Soil SSSAJ Book Series 5, Science Society of America, Inc. Madison, WI.

Sakaki, T., and T. H. Illangasekare. 2007. Comparison of height-averaged and point-measured capillary pressure – saturation relations for sands using a modified Tempe cell, Water Resour. Res., 43, W12502, doi: 10.1029/2006WR005814.

SAS/STAT 9.2 User's Guide: The NLIN Procedure (Book Excerpt).

Schaap J, Lehmann P, Frei G, Vontobel P, Kaestner A, Hassanein R. 2008. Measuring the effect of structure on water dynamics in heterogeneous porous media using fast neutron tomography. Adv Water Resour 31(9): 1233–41.

Schroth, M.H., S.J. Ahearn, J.S. Selker, and J.D. Istok. 1996. Characterization of Miller-similar silica sands for laboratory hydrologic studies. Soil Sci. Soc. Am. J. 60:1331–1339

Shokri N., Lehmann P., P. Vontobel P., and D. Or D. 2008, Drying front and water content dynamics during evaporation from sand delineated by neutron radiography Water Resour. Res. 44, W06418

Šimůnek, J., K. Huang, M. Šejna, and M. Th. van Genuchten, The Hydrus-1D software package for simulating the one-dimensional movement of water, heat, and multiple solutes in variably-saturated media. Version 1.0, IGWMC - TPS - 70, International Ground Water Modeling Center, Colorado School of Mines, Golden, Colorado, 186 pp., 1998.

Tullis, B.P., J.T. Lindsay, and S.J. Wright. 1994. The imaging of wetting front instabilities in porous media using neutron radioscopy. Nondestructive Testing and Evaluation 11: 97-106

Tumlinson, L.G., H. Liu, W.K. Silk, and J.W. Hopmans. 2008. Thermal neutron computed tomography of soil water and plant roots. Soil Science Society of America Journal. 72: 1234-1242.

U.S. Silica Company. 2009. Product Data Sheet: Whole Grain Silica. Berkeley Springs, WV.

van Genuchten, M. T. 1980. A closed form equation for predicting the hydraulic conductivity of unsaturated soils. Soil Science Society of America Journal, 44: 892-898.

Vasin, M., P. Lehmann, A. Kaestner, R. Hassanein, W. Nowak, R. Helmig, and I. Neuweiler. 2008. Drainage in heterogeneous sand columns with diff erent geometric structures. Adv. Water Resour. 31: 1205–1220. doi:10.1016/j. advwatres.2008.01.004

Appendix D

Table 4- 1 Brooks and Corey parameters for point water retention curves directly measured by neutron radiography and those from TrueCell inverse modeling of average water retention data.

Measurement/ Estimation Method	Brooks-Corey parameter estimates				n
	θ_s	θ_r	ψ_a	λ	
Point radiography data, median values	0.364	0.026	17.497	7.423	115
Point radiography data, mean values	0.374	0.027	17.462	7.744	115
Average radiography data, TrueCell	0.364	0.025	17.250	6.649	1

Note: θ_s is the saturated volumetric water content, θ_r is the residual volumetric water content, ψ_a is the air-entry value, λ is the pore-size distribution index, and n is the number of water retention curves analyzed.

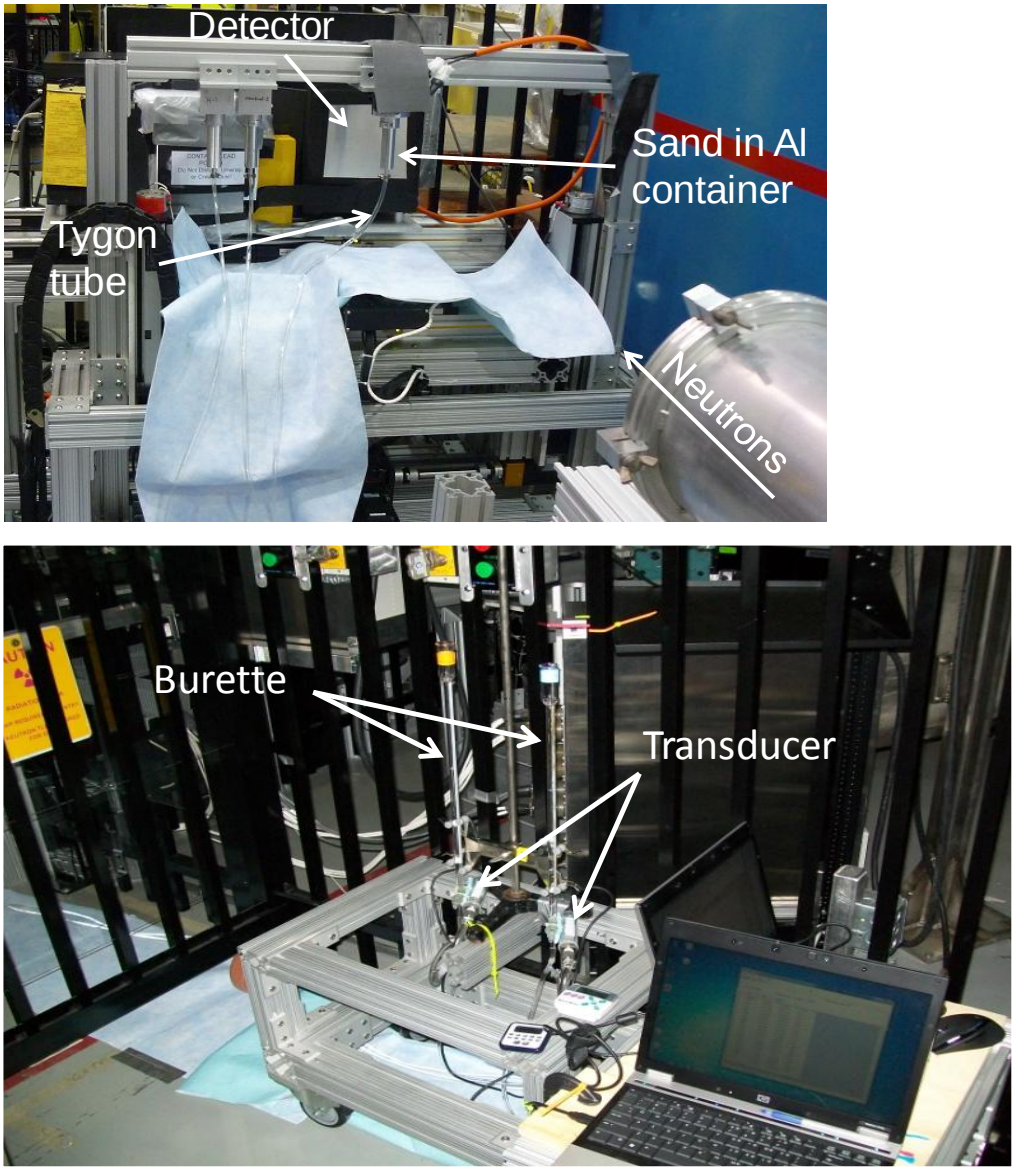

Figure 4- 1 Hanging water column set up for Flint sand at the HFIR CG1-D beamline. Various basal matric potentials were achieved by adjusting the height of the hanging water column outside of the beamline. The transducer attached to the burette recorded water level changes in the burette every second.

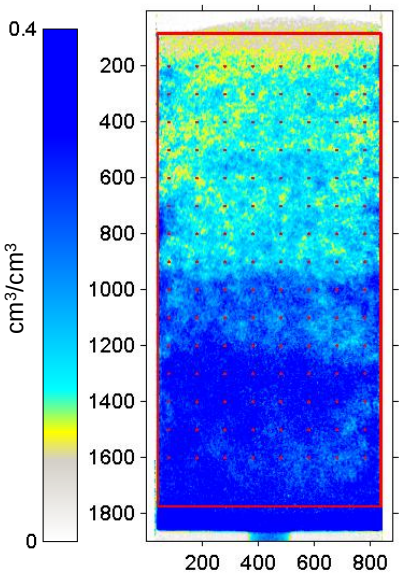

Figure 4- 2 Example of the 8 x 15 grid superimposed on a 2-D radiographic image (882 x 1,898 pixels) of air (white) displacing water (blue) in Flint sand at a given equilibrium basal matric potential used to construct the 120 point water retention curves. The ROI (red rectangle) was used to calculate the average water content.

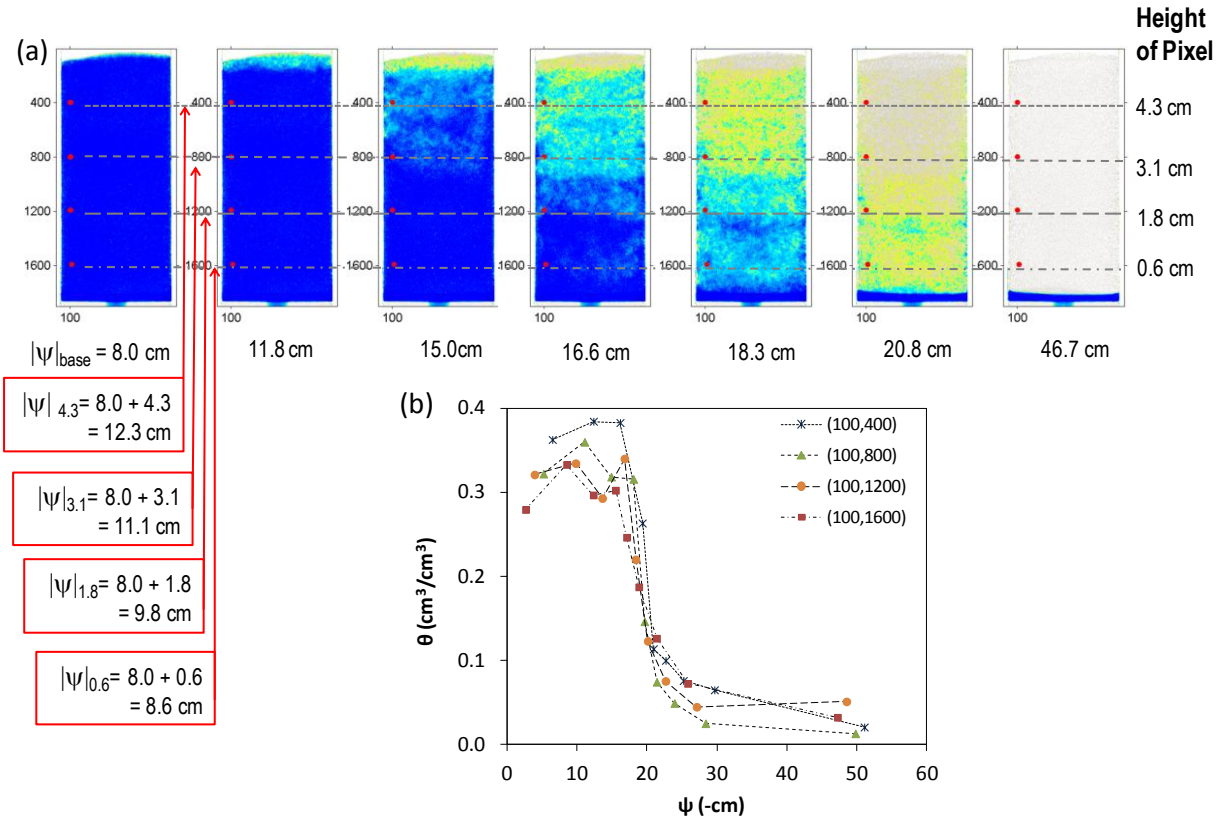

Figure 4- 3 (a) Selected volumetric water content images during drainage of Flint sand at basal matric potentials of -8 cm, -11.8 cm, -15.0 cm, -16.6 cm, -18.3 cm, -20.8 cm, and -46.7 cm. , The blue and white colors correspond to high and low water contents, respectively. The red dots denote 4 example pixel locations, (100,400), (100, 800), (100, 1200), and (100, 1600) on the 8 x 15 grid. The dashed lines correspond to the heights of these pixel locations above the phase barrier, i.e., 4.3 cm, 3.1 cm, 1.8 cm, and 0.6 cm, respectively. The absolute value of matic potential for each point was calculated by adding the pixel elevation above the phase barrier to the absolute value of basal matric potential. (b) The resulting point water retention curves for the 4 example pixel locations: (100,400), (100, 800), (100, 1200), and (100, 1600).

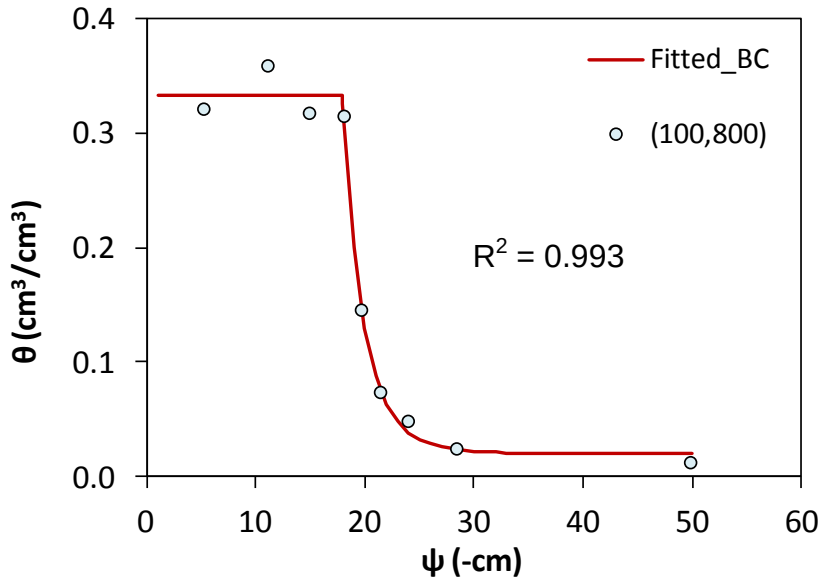

Figure 4- 4 Example fit of the Brooks and Corey equation to the directly measured point water retention data for pixel location (100,800).

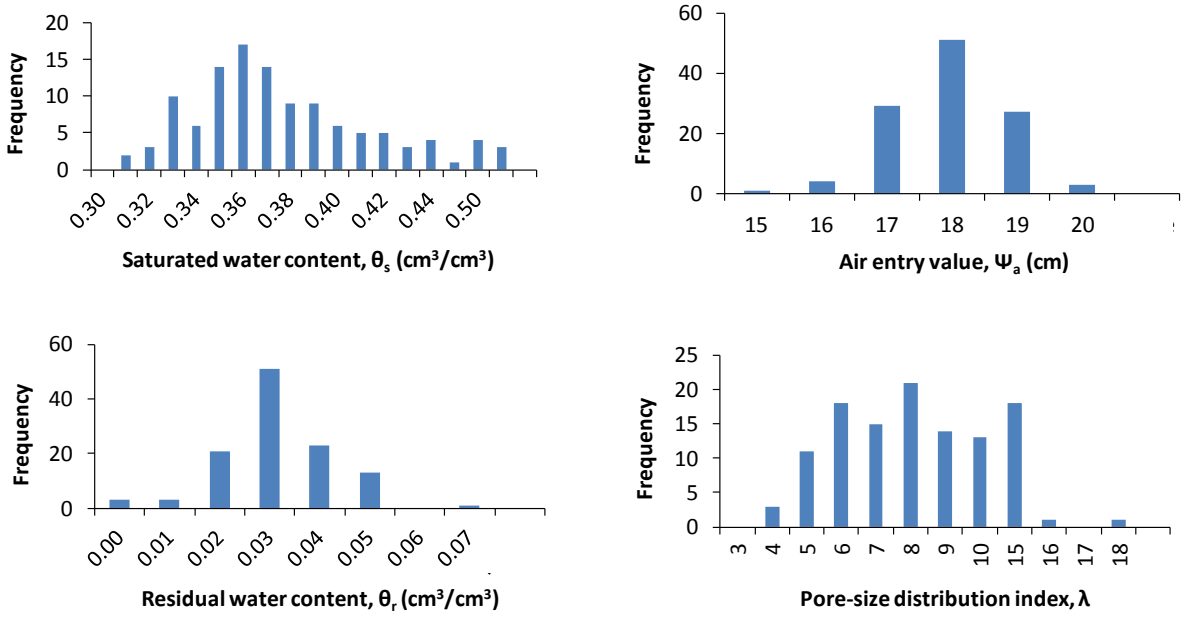

Figure 4- 5 Histograms for the 115 best fit estimates of the Brooks and Corey parameters: θ_s, θ_r, ψ_a, and λ.

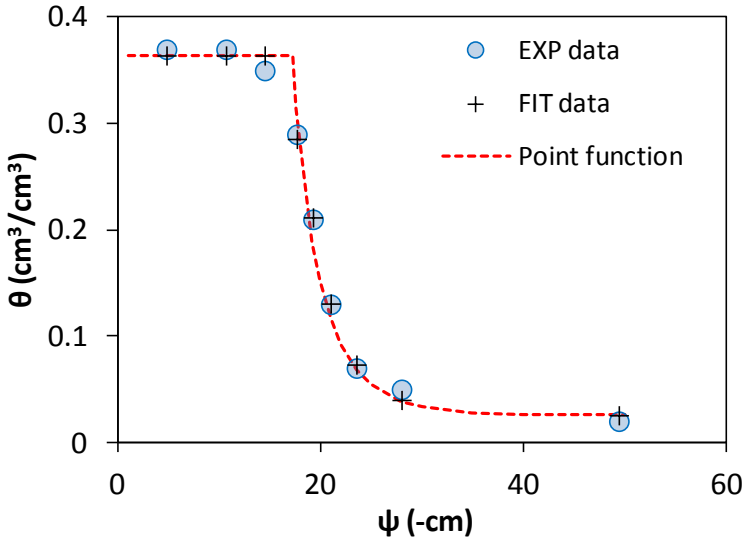

Figure 4- 6 The point Brooks and Corey function (dashed line) obtained using the TrueCell inverse model based on fitting (the crosses, FIT data) to the observed average water retention data (the circles, EXP data). The R^2 for this fit was 0.997.The resulting Brooks and Corey parameter estimates are listed in Table 4-1.

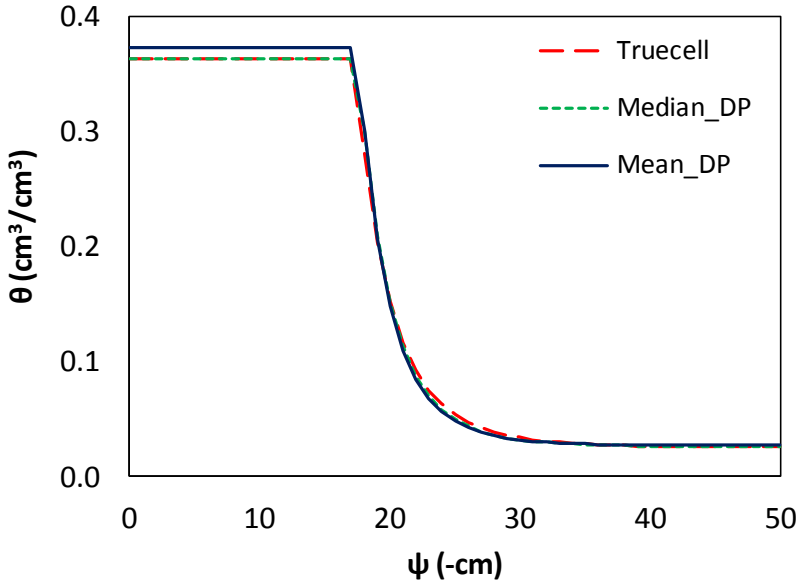

Figure 4- 7 Point water retention functions obtained using the median_DP (short dashed line), mean_DP (solid line) and TrueCell (long dashed line).

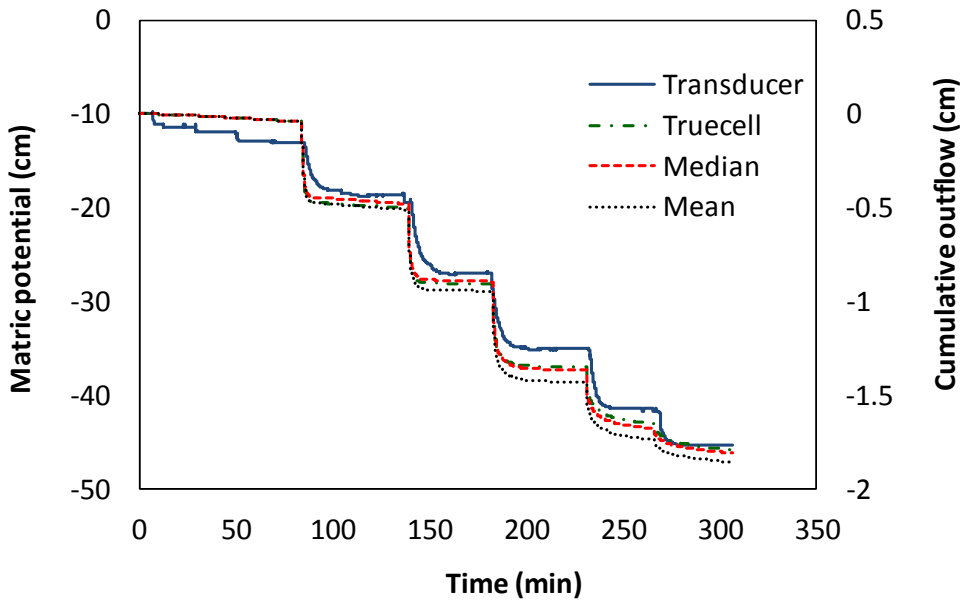

Figure 4- 8 Comparison of cumulative outflow simulated by HYDRUS 1-D using three sets of Brooks-Corey parameters: median_DP (dashed line), mean_DP (dotted line), and TrueCell (dashed-dotted line) as compared to the cumulative outflow measured with the Transducer (solid line). RMSE values for TrueCell, median_DP, and mean_DP relative to the transducer data were 0.091, 0.091, and 0.126 cm, respectively.

CHAPTER V

DIFFUSIVITY AND SORPTIVITY OF BEREA SANDSTONE DETERMINED USING NEUTRON RADIOGRAPHY

This chapter is a reformatted version of a paper originally accepted in Vadose Zone Journal in 2013 by Kang et al. Misun Kang participated in the experiments, performed data analyses, wrote some parts of the paper, and took the lead on the revision. Other co-authors contributed to the data acquisition, data analyses, and writing of the manuscript.

Kang M., E. Perfect, C.L. Cheng, H.Z. Bilheux, M.Gragg, D.M. Wright, J.M. Lamanna, J. Horita, and J.M. Warren, 2013. Diffusivity and sorptivity of Berea sandstone determined using neutron radiography. Vadose Zone Journal (accepted).

.

Abstract

Neutron radiography is increasingly being used to study the dynamics of water movement in variably-saturated porous media. It has been applied to visualize water imbibition in both natural and engineered materials, including soil, rock, brick, concrete, and glass. The sorptivity, *S*, and unsaturated diffusivity, $D(\theta)$, are important parameters for describing water movement under partially-saturated conditions. Estimates of *S* and $D(\theta)$ have been obtained using a variety of techniques, including neutron imaging. However, we could find no previous reports of such measurements for Berea sandstone, regardless of the method employed. Berea sandstone is a widespread, medium- to fine-grained terrestrial sandstone of Mississippian age, that is used extensively as a standard porous medium in the geology and petroleum engineering fields. We used the CG-1D neutron imaging facility at the High Flux Isotope Reactor of Oak Ridge National Laboratory to estimate *S* and $D(\theta)$ from radiographs acquired every 26 s. A 25 μm thick LiF/ZnS scintillator was employed in conjunction with a DW936 IkonL ANDOR^{TM} charge coupled device (CCD) camera system, giving a spatial imaging resolution of ~75 μm. Four replicate cores were investigated. The positions of the observed wetting fronts were linearly regressed against the square root of time. Sorptivity values calculated from the slopes of these relations ranged from 0.89 to 1.46 mm $s^{-1/2}$. Further analysis yielded $D(\theta)$ functions. These functions were very

reproducible and showed good agreement with independent $D(\theta)$ values calculated from relative permeability and capillary pressure -saturation data for Berea sandstone. To the best of our knowledge these are the first published estimates of *S* and $D(\theta)$ for Berea sandstone. Our results clearly demonstrate the effectiveness of neutron imaging in providing high quality, quantitative data for the computation of unsaturated flow parameters.

1. Introduction

Neutron imaging is based on measuring the transmitted intensity of neutrons through a sample, either in two dimensions (radiography) or three dimensions (tomography) (Anderson et al., 2009). Because neutrons are strongly attenuated by hydrogen, but much less attenuated by air in partially-saturated pores and solids that make up the mineral matrix, this technique is increasingly being used to study water movement in porous media. Over the past 25 years, it has been applied to visualize the dynamics of water imbibition in both natural and engineered materials, including brick, concrete, porous glass, rock, and soil.

In an early study, Brenizer and Gilpin (1987) used real time neutron radiography to quantify the advance of wetting fronts into initially dry sand columns. The transient infiltration of water into packed beds of soil aggregates has been visualized using neutron radiography (Carminati et al., 2007a and 2007b; Carminati and Flühler, 2009). Żołądek et al. (2008) employed neutron radiography to investigate water imbibition into granular zeolite beds.

Prazak et al. (1990) used neutron radiography to document water uptake in vacuum-pressed ceramic, limesand brick, and aerated concrete. Pel et al. (1993) applied scanning neutron radiography to determine the unsaturated diffusivity from water content profiles measured on clay brick and kaolin clay. Pleinert et al. (1998) utilized neutron radiography to quantify water uptake in brick samples. Nemec et al. (1999) applied fast, quasi-real-time neutron radiography to study the impregnation of silicone-based hydrophobic agents in clay bricks. Islam et al. (2000) studied the water adsorption characteristics of some Bangladeshi and Slovenian building materials using neutron radiography. More recently, El-Abd, Milczarek, and colleagues have employed neutron radiography in numerous studies on imaging the capillary imbibition of water in bricks (Czachor et al., 2002; El-Abd and Milczarek, 2004; El Abd et al. 2005, 2009; Milczarek et al., 2005).

Working with dry concrete, Hanzic and Ilic (2003) investigated the height of capillary rise versus square root of time relationship using neutron radiography.

de Beer et al. (2004, 2005) compared traditionally measured sorptivity values for concrete with those obtained by neutron radiography and found good agreement between the methods. Brew et al. (2009) provide another example where sorptivity values obtained by neutron radiography agreed well with those obtained by the traditional gravimetric method. The rate of water penetration into dry concrete samples, with capillarity as the driving force, has also been investigated using neutron tomography (McGlinn et al., 2010).

Masschaele et al. (2004) and Dierick et al. (2005) presented neutron tomograms for water and other fluids moving into limestone and sandstone rock samples, some of which had been treated with a water repellent.

Middleton et al. (2005) investigated spontaneous imbibition of water into air-filled Mardie Greensand and Barrow group sandstone samples using the dynamic neutron radiography capabilities of the SAFARI-1 reactor at NECSA, Pelindaba in South Africa.

The observed data were fitted to a simple diffusion equation with a constant diffusion parameter. Hassanein et al. (2006) imaged the capillary imbibition of deionized water and a 20% solution of NaCl into initially-dry rock samples (Mansfield sandstone, Salem limestone, and Hindustan whetstone) of various sample sizes, up to 40 cm. Their results show variations in sorptivity as a function of rock type, sample size, solution type, and mode of imbibition (top down versus bottom up). Cnudde et al. (2008) further explored the usefulness of high-speed neutron radiography for quantifying water uptake in rocks by capillarity. Hameed et al. (2009) and Zawisky et al., 2010) employed neutron radiography and tomography to compare the uptake of different consolidants by porous building stone used in historic buildings (Hameed et al., 2009; Zawisky et al., 2010). Recently, Gruener et al. (2012) have observed (at the micro-scale) capillarity-driven water imbibition into a nanoporous glass (Vycor) using neutron radiography.

We describe replicated dynamic neutron radiography experiments involving water imbibition into initially-dry Berea sandstone cores. Berea sandstone is naturally-occurring sedimentary rock used extensively as a standard porous medium for petrophysical investigations in the geology and petroleum engineering fields (Churcher et al., 1991). It is a medium- to fine-grained terrestrial sandstone of Mississippian age,

found predominantly in Ohio and surrounding states. The mineral matrix is composed primarily of quartz (~93%) (Pepper et al., 1954), and so it is well-suited for imaging water uptake with neutrons.

The neutron radiography data collected in this study are used to calculate the sorptivity, S [$LT^{-0.5}$], and the unsaturated diffusivity function, $D(\theta)$ [L^2T^{-1}], for Berea sandstone. These parameters are well established in soil physics for quantifying the movement of a capillary wetting front into partially-saturated soil. The sorptivity parameter is defined by the following expression (Philip, 1957):

$$S = \frac{x_{wf}}{\sqrt{t}} \quad [1]$$

where x_{wf} is the wetting front position, equivalent to cumulative infiltration per unit area (L), and t (T) is time.

The diffusivity function is given by (Bruce and Klute, 1956):

$$D(\theta) = K(\theta) \times dh/d\theta \quad [2]$$

where $K(\theta)$ [LT^{-1}] is the unsaturated hydraulic conductivity function, and $dh/d\theta$ [L] is the slope of the capillary pressure-saturation function.

Both S and $D(\theta)$ are relevant in the geology and petroleum engineering fields where they have been used evaluate reservoir rock wettability and the production of oil through spontaneous imbibition of water (Handy, 1960; Standnes, 2004).

A variety of experimental techniques, including gravimetric analysis (Reda Taha et al., 2001; Janz, 2002; Carmeliet et al., 2004; Tyner et al., 2006), geomechanical analysis (Kranz et al., 1990), and gamma-ray (Tyner and Brown, 2004) and magnetic resonance imaging (Gombia, 2008) have been employed to measure S and $D(\theta)$. Determinations based on neutron imaging data have been published for soil (Brenizer and Gilpin, 1987), brick (Pel et al., 1993; El-Abd and Milczarek, 2004; El Abd et al., 2009), cement (Brew et al., 2009), and rock - Mansfield sandstone, Salem limestone,

and Hindustan whetstone (Hassanein et al. 2006), but not for Berea sandstone. Only two previous neutron imaging studies involving Berea sandstone were found in the literature, both focusing on core flood experiments. Jasti et al. (1987) flooded an initially mineral oil-saturated Berea sandstone core with water in order to observe the migration of the immiscible front, while Jasti and Fogler (1992) recorded fluid distribution changes due to a miscible tracer pulse in flooding experiments performed on Berea sandstone cores.

The spontaneous imbibition of water by dry Berea sandstone has been documented in numerous oil- and gas-related publications (e.g., Garg et al., 1996; Schembre et al., 1998; Li and Horne, 2001; Kaul et al., 2004). However, we could find no previous reports of *S* or $D(\theta)$ calculations for this material, regardless of the actual measurement method employed. The vast majority of previous studies have focused on alternative theoretical analyses of the measured water uptake. Hammecker and Jeanette (1994) reported the slope of the linear relationship between height of capillary rise and the square root of time (equivalent to *S*) for five different sandstones, but not Berea sandstone. Only Dullien et al. (1977) seem to have reported this value for Berea sandstone, but their data were for the imbibition of a 2% NaCl brine solution, not water.

2. Materials and Methods

Four cylindrical Berea sandstone cores (designated A3, C3, D2, and O3) were selected to observe temporal changes in the spatial distribution of water during imbibition using neutron radiography. The cores were supplied by Coretest Systems, Morgan Hill, CA. Their dimensions are given in Table 5-1[5]. Average porosity and intrinsic permeability values reported by Coretest Systems for these samples were 0.218 and 4.2×10^{-14} m^2, respectively. Relative (unsaturated) hydraulic conductivity versus relative saturation curves were measured using transient flow centrifugation at

[5] Note: all the figures and tables are in Appendix F.

9,000 rpm as described by Hagoort (1980) and van den Berg et al. (2009). These curves were parameterized by fitting Eq. (13) of Brooks and Corey (1964) to the data; average values of the resulting residual saturation and epsilon parameters were 0.062 and 5.20, respectively. Point estimates of Brooks and Corey (1964) capillary–pressure saturation parameters for a different set of Berea cores are given in Cropper et al. (2011).

The water imbibition experiments were performed in the beamline at the High Flux Isotope Reactor (HFIR) CG-1D neutron imaging facility of Oak Ridge National Laboratory (ORNL). This beamline provides cold neutrons between approximately 0.8 and 10 Å (with a peak at ~2.6 Å). For this study a 25 µm thick LiF/ZnS scintillator was used in conjunction with a DW936 IkonL ANDOR^{TM} charge coupled device (CCD) camera system, giving a spatial imaging resolution of ~75 µm. Additional technical details about the CG-1D beamline setup are given in Bilheux et al. (2013) and Kang et al. (2013).

The Berea sandstone cores were oven dried at 105°C for 24 h prior to placing them in the beamline so as to remove any pore water. After oven drying each core was placed in a cylindrical Al container with an inner diameter 2.9 cm and a height of 10 cm. The top and sides of the core within the Al cylinder were open to the atmosphere. A water inlet at the bottom of the cylinder was connected to a Mariotte bottle device (consisting of a sealed 50 ml plastic burette and bubbling tube) by Tygon tubing (R3603, 3.175 mm i.d. by 6.35 mm o.d., Fisher Scientific) filled with distilled water. Initially there was no hydraulic contact between the base of the rock core and the water in the tubing. Once image acquisition began (see below) the bubbling tube in the Mariotte bottle was raised to a height corresponding to the bottom of the Berea sandstone core to supply water at constant head for imbibition. A schematic diagram of the experimental set-up is shown in Fig. 5-1. Images were continuously acquired with a 20 s exposure time and 4 pixels × 4 pixels binning until the water reached the top of the core. Open beam (OB), dark field (DF), and oven dry Berea sandstone images were also acquired for normalization purposes.

All image processing and quantitative analyses were performed using the MATLAB (Version 7.11, R2010b-SP1, MathWorks®, Inc., 2011) and ImageJ (Version

1.43m, National Institutes of Health, 2009) software packages. For each acquired image, the two-dimensional distribution of water within the Berea sandstone core was determined as follows.

First, the raw images, $I_{(Raw\ Image)}$, of the wet and oven dry sandstone cores were normalized with respect to reference images of the OB and DF, $I_{(OB)}$ and $I_{(DF)}$, respectively, using the following expression:

$$I_n = f_k \frac{I_{(Raw\ Image)} - I_{(DF)}}{I_{(OB)} - I_{(DF)}} \quad [3]$$

where f_k is a rescaling factor used to correct for fluctuations in the neutron flux. The f_k was determined for each image based on differences in the mean intensity values between selected empty areas (i.e., no core) in the raw images and the means of the same areas in the open beam images.

The normalized images (I_n) were then despeckled using a median filter (5 pixels × 5 pixels) to remove bright pixels due to scattered γ-rays. Figure 5-2 shows examples of the resulting normalized neutron radiographs for water uptake in Berea core sample C3 at selected times.

Next, the normalized wet images were divided by the normalized oven dry images to remove any attenuation effects associated with minerals in the core and/or the aluminum sample holder. The water thickness, $\tau_{(i,j)}$, for each pixel (i,j) in the neutron radiographs of the Berea cores was calculated using the following expression:

$$\tau_{(i,j)} = -\frac{\mu}{2\beta} - \sqrt{\left[\frac{\mu}{2\beta}\right]^2 - \frac{1}{\beta}\ln\left[\frac{I_{wet}}{I_{dry}}\right]_{(i,j)}} \quad [4]$$

where, $\tau_{(i,j)}$ is water thickness (m), μ (= 5.542 x 10^2 m^{-1}) is the attenuation coefficient for water, β (= -2.140 x 10^4 m^{-2}) is a coefficient that takes into account beam hardening,

and I_{wet} and I_{dry} are the normalized wet and dry images, respectively. The μ and β values were determined by calibration using water-filled Al cells machined to give a range of known water thicknesses (Kang et al., 2013).

To compute the two-dimensional distribution of volumetric water contents in the cores, the measured water thicknesses were corrected for variations in the neutron transmission path length based on the chord length, $C_{(i,j)}$, for a circle:

$$C_{(i,j)} = 2\sqrt{r^2 - a_{(i,j)}^2} \quad [5]$$

where r is the radius of the Berea core and $a_{(i,j)}$ is the distance from the center of the core to the pixel (i,j).

The volumetric water content at pixel (i,j), $\theta_{(i,j)}$ ($m^3\ m^{-3}$), is then simply the ratio of the measured water thickness to the chord length, i.e.

$$\theta_{(ij)} = \frac{\tau_{(i,j)} \times pixel\ area}{C_{(i,j)} \times pixel\ area} = \frac{\tau_{(i,j)}}{C_{(i,j)}} \quad [6]$$

Between 46 and 102 images were analyzed in this way for each sandstone core (see Table 5-2). The time interval between consecutive images was 26 s (i.e., 20 s exposure time plus 6 s for image transmission/storage).

3. Results and Discussion

Sorptivity Analysis

Because the wetting front was not perfectly horizontal (Fig. 5-2), and to eliminate edge and lateral flow effects, we quantified the one-dimensional imbibition of water over time by selecting volumetric water contents, θ, for a vertical column of pixels centered on the water inlet at the base of the sample holder. Figure 5-3 shows the volumetric water content versus distance profiles for all of the 90 neutron radiographs acquired for the Berea core sample C3. Distance corresponds to height above the free water table located at the bottom of the aluminum cylinder. From these profiles the position of the wetting front was determined as a function of time for each core. The location of the wetting front was defined as the distance at which the volumetric water content in the core goes to zero (i.e., the point where a given time profile intercepts the x-axis in Fig. 5-3). Ignoring the contribution of gravity, a common assumption with early time data such as these (each experiment lasted < 40 min and the maximum height of capillary rise was < 5 cm), the resulting wetting front positions were related to time (taken from the image time stamps) using Eq. [1]. The sorptivity parameter was estimated using linear regression. The bond number ($B_o = \rho g k/\sigma$) for Berea sandstone was calculated from the air-water interfacial tension, σ = 0.0728 N/m at 20 °C, the density of water, ρ = 1,000 kg/m^3, gravitational acceleration, g = 9.81 m/s^2, and intrinsic permeability, k = 4.2 $\times$ 10^{-14} m^2. The resulting value of B_o = 5.6 x 10^{-9} was much less than unity, which validates our assumption that capillary forces dominated over gravity in these experiments. Figure 5-4 illustrates the linearity of the wetting front location versus the square root of time for Berea core sample C3. Sorptivity values and the associated coefficients of determination (R^2 values) for all four cores tested are presented Table 5-2. All of the R^2 values were > 0.97, indicating excellent goodness-of-fit, with minimal scatter around the regression lines. The close correspondence between the observed data points and best fit predictions of Eq. [1] further supports the assumption that any effect of gravity on water uptake in these relatively short experiments was negligible. The regression estimates of sorptivity for Berea sandstone ranged from 0.89 to 1.46

mm $s^{-1/2}$ (Table 5-2). The differences in *S* values (equivalent to a coefficient of variation of ~20%) can be attributed to a combination of natural variations in the connectivity and size distribution of pores within the rock cores and experimental error. The average sorptivity for Berea sandstone, calculated from the data in Table 5-2, was 1.17 mm $s^{-1/2}$. This estimate falls centrally within the range of values (0.10 – 1.72 mm $s^{-1/2}$) given by Hammecker and Jeannette (1994) for capillary-driven water uptake in sandstones. It also compares favorably with the value of 1.58 mm $s^{-1/2}$ reported by Dullien et al. (1977) for spontaneous imbibition of a 2% NaCl brine solution by Berea sandstone.

In addition to estimating the sorptivity parameter, we also used the neutron radiographs to calculate unsaturated diffusivity functions for Berea sandstone, as described in the next two sections.

Boltzmann Analysis

To solve the non-linear diffusivity equation, which mathematically describes the transient flow of moisture in an unsaturated porous medium, the Boltzmann transformation, λ, was introduced (Bruce and Klute, 1956):

$$\lambda = {}^{x}/_{\sqrt{t}} \qquad [7]$$

where x is distance traveled by the wetting front.

For each water content versus distance profile λ values were calculated using Eq. [7] and the volumetric water content data were re-plotted as a function of λ. Figure 5-5 shows the volumetric water contents, θ, for Berea core sample C3 as a function of λ. Note that, with the exception of a few data sets generated from the early time images, all of the profiles generally converge into a single function that intercepts the x-axis at ~0.9 λ. The deviations indicate a departure from Boltzmann scaling at early times possibly due to limitations in spatial and/or temporal resolution during acquisition of the early time images and/or sample anisotropy/heterogeneity, resulting in the non-uniform distribution of water within the cores (Pel et al. 1993, Carmeliet et al. 2004). These

deviations could also be caused by an initial surge in positive pressure at the inlet when water flow was first initiated with the Mariotte system.

Meyer and Warwick Diffusivity Analysis

An analytical solution was used to extract unsaturated diffusivity functions from the Boltzmann transformed data sets. Assuming negligible effects due to gravity and zero initial water content, the expression for the normalized water content profile at all times is given by (Meyer and Warrick, 1990):

$$\theta/\theta_s = \frac{\left[1 - \left(\lambda/\lambda_i\right)\right]}{\left[1 - A\left(\lambda/\lambda_i\right)\right]} \qquad [8]$$

where θ_s is the satiated volumetric water content, A is a shape factor, and λ_i is the value of λ where θ = 0.

The Boltzmann analysis profiles were normalized by division by the λ_i values for each core, corresponding to the position of the wetting front. For example, the average λ_i for C3 was 0.89. Equation [8] was then fitted to the normalized Boltzmann profiles in order to estimate θ_s and A using the Marquardt non-linear regression method in SAS 9.2. Figure 5-6 shows an example fit for Berea core sample C3. The fit is very good, with an R^2 value of 0.85. Results for all of the cores tested are listed in Table 5-3, which shows very little variation (coefficients of variation were < 10% in both cases) among the estimated θ_s and A values. It should be noted that because of air entrapment during imbibition, the average satiated water content, θ_s, represents only 56% of total saturation, based on the porosity. This value is quite a bit lower than that for soil materials, in which θ_s is usually about 85% of total saturation (Dane and Hopmans, 2002).

Using the θ_s and A parameters from the non-linear regression along with the average λ_i values, the unsaturated diffusivity function, $D(\theta)$, can be constructed using the method described by Meyer and Warrick (1990):

$$D(\theta) = -0.5 \left[\frac{A_3 - A_1 A_2}{(A_3 - A_2\theta)^2}\right] f(0,\theta)$$

$$f(0,\theta) = -\left(\frac{1}{A_2}\right)\theta + \left[(A_1 A_2 - A_3)/{A_2}^2\right] ln\left[\frac{\theta - \left({A_3}/{A_2}\right)}{-\left({A_3}/{A_2}\right)}\right] \quad [9]$$

where $A_1 = \theta_s$, $A_2 = -A/\lambda_i$, and $A_3 = -\theta_s/\lambda_i$. For example, A_1 = 0.11, A_2 = -1.02, and A_3 = -0.13 for Berea rock core C3. Figure 5-7 shows the calculated log unsaturated diffusivity functions for all four Berea rock cores. There was very good reproducibility, with less than one log unit variation in $D(\theta)$ between samples over the entire range of water contents. The $D(\theta)$ values decreased non-linearly over several orders of magnitude with decreasing water content (Fig. 5-7). There was also reasonable agreement between the calculated $D(\theta)$ values and the function predicted from $K(\theta)$ and $dh/d\theta$ data for Berea sandstone using Eq. [2]. The largest deviations, which were always less than one order of magnitude, occurred at the higher water contents. This is not surprising given the different experimental protocols involved (i.e., wetting up from oven dryness versus drainage from a saturated state). Kranz et al. (1990) published an estimate of the unsaturated diffusivity for a saturated Berea sandstone core, determined using pore water pressure oscillations. However, their estimated value of 3 x 10^4 mm^2 s^{-1} (or 4.48 in log scale units for comparison with Fig. 5-7) was only for a single volumetric water content (of 0.23 m^3m^{-3}), well outside the unsaturated range considered here. Other than the study by Kranz et al. (1990) we could find no other comparable analyses for Berea sandstone in the literature. Thus, our results appear to be the first to describe the functional dependence of diffusivity on water content for this widely-used standard porous medium.

4. Conclusions

The imbibition of water into four replicate core samples of initially dry Berea sandstone was visualized using neutron radiography. The results showed a strong linear relationship between the observed wetting front and the square root of time, indicating that capillary forces dominated over gravity in these experiments. Sorptivity

values were calculated from the imaging data, and appear to be the first reported for this widely-used standard porous medium. Further analysis, based on the Boltzmann transformation and analytical model of Meyer and Warwick (1990), yielded diffusivity versus water content relationships (again, the first to be reported for Berea sandstone), which showed very good agreement between the samples. These results clearly demonstrate the effectiveness of neutron imaging in providing high quality, quantitative data for the computation of unsaturated flow and transport parameters. Furthermore, because the data are spatially resolved, they also provide the option of estimating these parameters by inverse numerical modeling, an application not explored here, but one that certainly merits investigation in the future.

Acknowledgements

This paper is based in part on assignments prepared by graduate students participating in a seminar course on imaging water in porous media (GEOL 685) taught by Ed Perfect at the University of Tennessee -Knoxville (UTK) in the spring semester of 2012. The neutron imaging at Oak Ridge National Laboratory's (ORNL) High Flux Isotope Reactor (HFIR) was sponsored by the Scientific User Facilities Division, Office of Basic Energy Sciences, U.S. Department of Energy, which is managed by UT-Battelle, LLC. Lakeisha Walker provided excellent technical support at HFIR. Portions of the MATLAB code used for the quantitative image analyses were developed by Keely Willis and Sophie Voisin at ORNL. Funding was provided by the Laboratory Directed Research and Development Program of ORNL and the Joint Directed Research and Development Program of the UT-ORNL Science Alliance at UTK.

References

Anderson, I.S., R.L. McGreevy, and H.Z. Bilheux (eds.). 2009. Neutron Imaging and Applications: A Reference for the Imaging Community. Springer, New York, NY., 341 pp.

Bilheux, H., K. Crawford, L. Walker, S. Voisin, M. Kang, M. Harvey, B. Bailey, M. Phillips, J-C. Bilheux, K. Berry, J. Ankner, J. Warren, J. Nanda, S. Pannala, and M. Lance. 2013. Neutron imaging at the Oak Ridge National Laboratory: Present and future capabilities. Physics Procedia (in press).

Brenizer, J.S., and H.E. Gilpin. 1987. Observations of unsaturated water-flow using real-time neutron radiography. Soil Sci. 144: 122-127. doi:10.1097/00010694-198708000-00006

Brew, D. R. M., F.C. de Beer, M.J. Radebe, R. Nshimirimana, P.J. McGlinn, L.P. Aldridge, and T.E. Payne. 2009. Water transport through cement-based barriers – a preliminary study using neutron radiography and tomography. Nucl. Instr. Meth. Phys. Res. A 605: 163-166.

Brooks, R. H., and A.T. Corey. 1964. Hydraulic properties of porous media. Hydrology Paper no. 3, Colorado State University, Fort Collins, CO.

Bruce, R. R. and A. Klute, 1956. The measurement of soil moisture diffusivity. Soil Sci. Soc. Amer. Proc. 20:458-462. doi:10.2136/sssaj1956.03615995002000040004x

Carmeliet, J., H. Hens, S. Roels, O. Adan, H. Brocken, R. Cerny, Z. Pavlik, C. Hall, K. Kumaran and L. Pel. 2004. Determination of the Liquid Water Diffusivity from Transient Moisture Transfer Experiments. J. Bldg. Phys. 27: 277-305.

Carminati A., A. Kaestner, R. Hassanein, P. Vontobel, and H. Flühler. 2007a. Infiltration through series of soil aggregates. Adv. Water Resour. 30:1168–78.

Carminati, A. A. Kaestner, O. Ippisch, A. Koliji, P. Lehmann, R. Hassanein, P. Vontobel. E. Lehmann, L. Laloui, L. Vulliet, and H. Flühler. 2007b. Water flow between soil aggregates. Transp. Porous Media 68: 219–236.

Carminati , A., and H. Flühler. 2009. Water infiltration and redistribution in soil aggregate packings. Vadose Zone J. 8:150–157.

Churcher, P.L., P.R. French, J.C. Shaw, and L.L. Schramm. 1991. Rock properties of Berea Sandstone, Baker Dolomite, and Indiana Limestone. SPE Intl. Symp. on Oilfield Chemistry, 20-22 February 1991, Anaheim, California, SPE 21044, p. 431-446.

Cnudde, V., M. Dierick, J. Vlassenbroeck, B. Masschaele, E. Lehmann, P. Jacob, L. Van Hoorebeke. 2008. High-speed neutron radiography for monitoring the water absorption by capillarity in porous materials. Nucl. Instrum. Methods Phys. Res., Sect. B. 266: 155–163.

Cropper, S.C., E. Perfect, E.H. van den Berg, and M.A. Mayes. 2011. Comparison of average and point capillary pressure-saturation functions determined by steady-state centrifugation. Soil Sci. Soc. Am. J. 75:17-25.

Czachor, A. A.E. El-Abd, and J.J. Milczarek, 2002. Determination of capillary motion of water in bricks using neutron radiography. Acta Physica Polonica A 102: 245–252.

Dane, J.H., and J.W. Hopmans. 2002. Water retention and storage, p. 671– 720, in J.H. Dane and G.C. Topp (eds.), Methods of Soil Analysis, Part 4, Physical Methods, Soil Science Society of America, Madison, WI.

de Beer, F.C., M. F. Middleton, and J. Hilson. 2004. Neutron radiography of porous rocks and iron ore. Appl. Radiat. Isot. 61: 487–495.

de Beer, F. C., le Roux, J. J., and Kearsley, E. P. 2005. Testing the durability of concrete with neutron radiography. Nucl. Instr. Meth. Phys. Res. A 542: 226-231.

de Beer, F.C. and Middleton, M. F. 2006. Neutron radiography imaging, porosity and permeability in porous rocks. South African J. Geol. 109: 541-550.

Dierick M., J. Vlassenbroeck, B. Masschaele, V. Cnudde, L. van Hoorebeke, A. Hillenbach. 2005. High-speed neutron tomography of dynamic processes. Nucl. Instr.. Meth. Phys. Res. A. 542:296-301.

Dullien, F.A.L., and M.S. El-Sayed, and V.K. Batra. 1977. Rate of capillary rise in porous media with nonuniform pores. J. Colloid Interface Sci. 60: 497-506.

El-Abd, A.E. and J.J. Milczarek, 2004. Neutron radiography study of water absorption in porous building materials: anomalous diffusion analysis. J. Phys. D 37: 2305–2313.

El-Abd, A.E., A. Czachor, J.J. Milczarek, and J. Pogorzelski 2005. Neutron radiography studies of water migration in construction porous materials. IEEE Trans. Nucl. Sci. 52: 229-304.

El-Abd, A. Czachor, A., and Milczarek, J. 2009. Neutron radiography determination of water diffusivity in fired clay brick. Appl. Radiation Isotopes. 47: 556-559

Garg, A., E. Zwahlen, and T.W. Patzek. 1996. Experimental and numerical studies of one-dimensional imbibition in Berea sandstone. Paper presented at the 16th Annual American Geophysical Union Hydrology Days, Fort Collins, CO, 15-18 Apr. 1996.

Gombia, M., V. Bortolotti, R.J.S. Brown, M. Camaiti, and P. Fantazzini. 2008. Models of water imbibition in untreated and treated porous media validated by quantitative magnetic resonance imaging. J. Appl. Phys. 103: 094913.

Gruener, S., Z. Sadjadi, H.E. Hermes, A.V. Kityk, K. Knorr, S.U. Egelhaaf, H. Rieger, and P. Huber. 2012. Anomalous front broadening during spontaneous imbibition in a matrix with elongated pores. Proc. Nat. Acad. Sci. 109: 10245-10250.

Hagoort, J. 1980. Oil recovery by gravity drainage. J. Soc. Petrol. Eng., publ. 7424, 20:139-150.

Hanziç, L. and Illic, R. 2003. Relationship between liquid sorptivity and capillarity in concrete. Cement Concrete Res. 33: 1385-1388.

Hameed, F., B. Schillinger, A. Rohatsch, M. Zawisky and H. Rauch. 2009. Investigations of stone consolidants by neutron imaging. Nucl. Instr. Meth. Phys. Res. A. 605: 150–153.

Hammecker, C., and D. Jeannette. 1994. Modelling the capillary imbibition kinetics in sedimentary rocks: Role of petrographical features. Transp. Porous Media 17: 285-303.

Handy, L.L., 1960. Determination of effective capillary pressures for porous media from imbibition data. Petrol. Trans. AIME 219: 75-80.

Hassanein, R., H.O. Meyer, A. Carminati, M. Estermann, E. Lehmann, and P. Vontobel. 2006. Investigation of water imbibitions in porous stone by thermal neutron radiography. J. Phys. D. 39: 4284-4291.

Islam. M.N., M.K. Alam, M.A. Zaman, M.H. Alhsan, and N.I. Molla. 2000. Application of neutron radiography to building industries. Indian J. Pure Appl. Phys. 38: 348-354

Jasti, J. K., Lindsay, J. T., and Fogler, H. S. 1987. Flow imaging of porous media using neutron radiography. SPE Annual Technical Conference and Exhibition, Dallas, Sept. 27−30, 1987, SPE paper #16950.

Jasti, J. K. and Fogler, H. S. 1992. Application of neutron radiography to image flow phenomena in porous media. AIChE J. 38: 481-488.

Janz, M. 2002. Moisture diffusivities evaluated at high moisture levels from a series of water absorption tests. Mater. Struct. 35: 141-148.

Kang, M., H.Z. Bilheux, S. Voisin, C.L. Cheng, E. Perfect, J. Horita, and J.M. Warren. 2013. Water calibration measurements for neutron radiography: application to water content quantification in porous media. Nucl. Instr. Meth. Phys. Res. A. doi:10.1016/j.nima.2012.12.112.

Kaul, S.P., E. Putra, and D.S. Schechter. 2004. Simulation of spontaneous imbibition using Rayleigh-Ritz finite element method— A discrete fracture approach. Petrol. Soc., Paper 2004-228, 16 pp.

Kranz, R.L., J.S. Saltzman, and J.D. Blacis. 1990. Hydraulic diffusivity measurements on laboratory rock samples using an oscillating pore pressure method. Int. J. Rock Mech. Min. Sci. and Geomech. Abstr. 27: 345-352.

Li, K., and R.N. Horne. 2001. Characterization of spontaneous water imbibition into gas-saturated rocks. Soc. Petrol. Eng. J., Paper 74703, p. 375-384.

Masschaele, B., M. Dierick, L. van Hoorebeke, V. Cnudde, and P. Jacobs. 2004. The use of neutrons and monochromatic X-rays for non-destructive testing in geological materials. Environ. Geol. 46: 486-492.

McGlinn, P. J., F.C. de Beer, L.P. Aldridge, M.J. Radebe, R. Nshimirimana, D. Brew, T.E. Payne, and K. Olufson. 2010. Appraisal of a cementitious material for waste disposal: Neutron imaging studies of pore structure and sorptivity. Cement Concrete Res. 40: 1320-1326

Meyer, J. J. and A.W. Warrick. 1990. Analytical Expression for Soil Water Diffusivity Derived from Horizontal Infiltration Experiments Soil Sci. Soc. Am. J. 54: 1547–1552.

Middleton, M.F., K. Li, and F. de Beer. 2005. Spontaneous imbibition studies of Australian reservoir rocks with neutron radiography. Paper presented at the 2005 SPE Western Regional Meeting, Irvine, CA, Mar. 30-Apr. 1, 2005, SPE #93634.

Milczarek, J.J., A. Czachor, A.E. El-Abd, and Z. Wisnieswki. 2005. Dynamic neutron radiography observations of water migration in porous media. Nucl. Instr. Meth. Phys. Res. A 542: 232–236.

Nemec, T., J. Rant, V. Apih, and B. Glumac. 1999. Study of building materials impregnation processes by quasi-real-time neutron radiography. Nucl. Instr. Meth. Phys. Res. A 24: 242-247.

Pel, L., A.A. J Ketelaars, O.C.G. Adan, and A.A. van Well. 1993. Determination of moisture diffusivity in porous media using scanning neutron radiography. Intl. J. Heat Mass Transfer. 36:1261-1267

Pepper, J.F.; Dewitt, W.; and Demarest, D.F. 1954. Geology of the Bedford Shale and Berea Sandstone In the Appalachian Basin. USGS Prof. Paper #259

Philip, J. R. 1957. The theory of infiltration: 4. Sorptivity and algebraic infiltration equations. Soil Sci. 84: 257-264.

Pleinert, H. and C. Degueldre. 1995. Neutron radiographic measurement of porosity of crystalline rock samples, a feasibility study. J. Contam. Hydrol. 19: 29-46.

Pleinert, H., H. Sadouki, and F.H. Wittmann. 1998. Determination of moisture distributions in porous building materials by neutron transmission analysis. Mater. Struct. 31: 218-224.

Prazak, J., Tywoniak, J., Peterka, F., and Slonc, T. 1990. Description of transport of liquid in porous media - a study based on neutron radiography data. Intl. J. Heat Mass Transfer 33: 1105-1120

Reda Taha, M.M., A.S. El-Dieb, and N.G. Shrive. 2001. Sorptivity: a reliable measurement for surface absorption of masonry brick units. Mater. Struct. 34: 438-445.

Schembre, J., S. Akin, and A.R. Kovscek. 1998. Spontaneous imbibition in low permeability media. SUPRI TR 114, Report prepared for the U.S. Department of Energy, 100 pp.

Standnes, D.C. 2004. Analysis of oil recovery rates for spontaneous imbibition of aqueous solutions into preferential oil-wet carbonates by estimation of capillary diffusivity coefficients. Colloids and Surfaces A 251: 93-101.

Tyner, J.S. and G.O. Brown. 2004. Improvements to estimating unsaturated soil properties from horizontal infiltration. Soil Sci. Soc. Am. J. 68: 1-6.

Tyner, J. S., Arya, L. M., and W.C. Wright. 2006. The dual gravimetric hot-air method for measuring soil water diffusivity. Vadose Zone J. 5: 1267-1272.

van den Berg, E.H., E. Perfect, C. Tu, P.S.K. Knappett, T.P. Leao, and R.W. Donat. 2009. Unsaturated hydraulic conductivity measurements with centrifuges: A review. Vadose Zone J. 8:531-547.

Zawisky, M., F. Hameed, E. Dyrnjaja, J. Springer, and A. Rohatsch. 2010. Digitized neutron imaging with high spatial resolution at a low power research reactor: Applications to steel and rock samples. Nucl. Instr. Meth. Phys. Res. B. 268: 2446–2450.

Żołądek J., Milczarek J. J., Fijał-Kirejczyk I. 2008. Dynamic neutron radiography studies of water migration in beds of natural zeolite. Nukleonika 53(Supplement 2): S113−S119.

Appendix E

Table 5- 1 Dimensions of the four Berea sandstone cores.

Sample #	Diameter (mm)	Length (mm)
A3	25.3	50.8
C3	25.8	51.2
D2	25.5	51.7
O3	25.5	50.6

Table 5- 2 Results of sorptivity analyses for the wetting front versus the square root of time, Eq. [1].

Sample #	n	S [mm $s^{-1/2}$]	R^2
A3	102	1.18	0.986
C3	90	0.89	0.997
D2	69	1.14	0.978
O3	46	1.46	0.981

Note: n = number of observations, S = sorptivity, R^2 = coefficient of determination

Table 5- 3 Results of fitting the Meyer and Warrick (1990) model, Eq. [9], to the normalized water content distributions.

Sample #	n	θ_s	*A*	R^2
A3	24,017	0.13	0.87	0.87
C3	22,600	0.11	0.91	0.85
D2	21,580	0.12	0.80	0.83
O3	13,463	0.13	0.89	0.85

Note: n = number of observations, θ_s = satiated water content, *A* = shape factor, R^2 = coefficient of determination

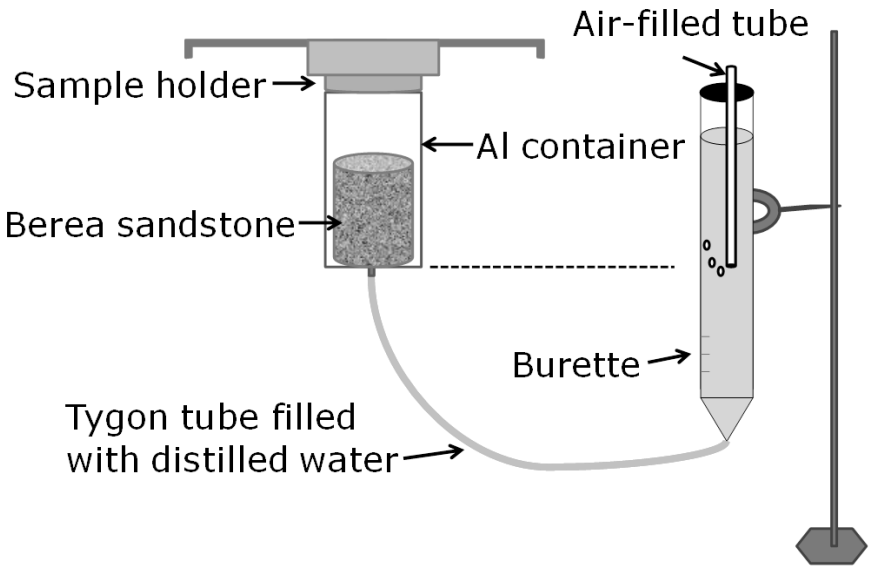

Figure 5- 1 A schematic diagram of the Mariotte bottle setup used to supply water to the base of the sandstone core at constant head.

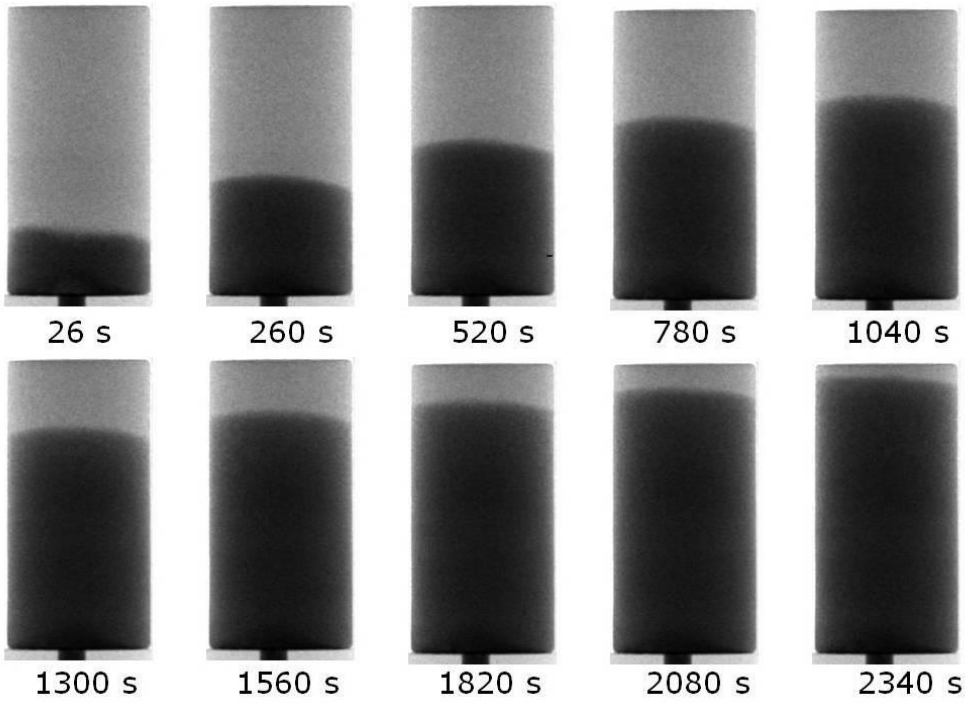

Figure 5- 2 Examples of normalized neutron radiographs at selected times for water imbibition by Berea core sample C3: light grey = oven dry, dark grey = satiation.

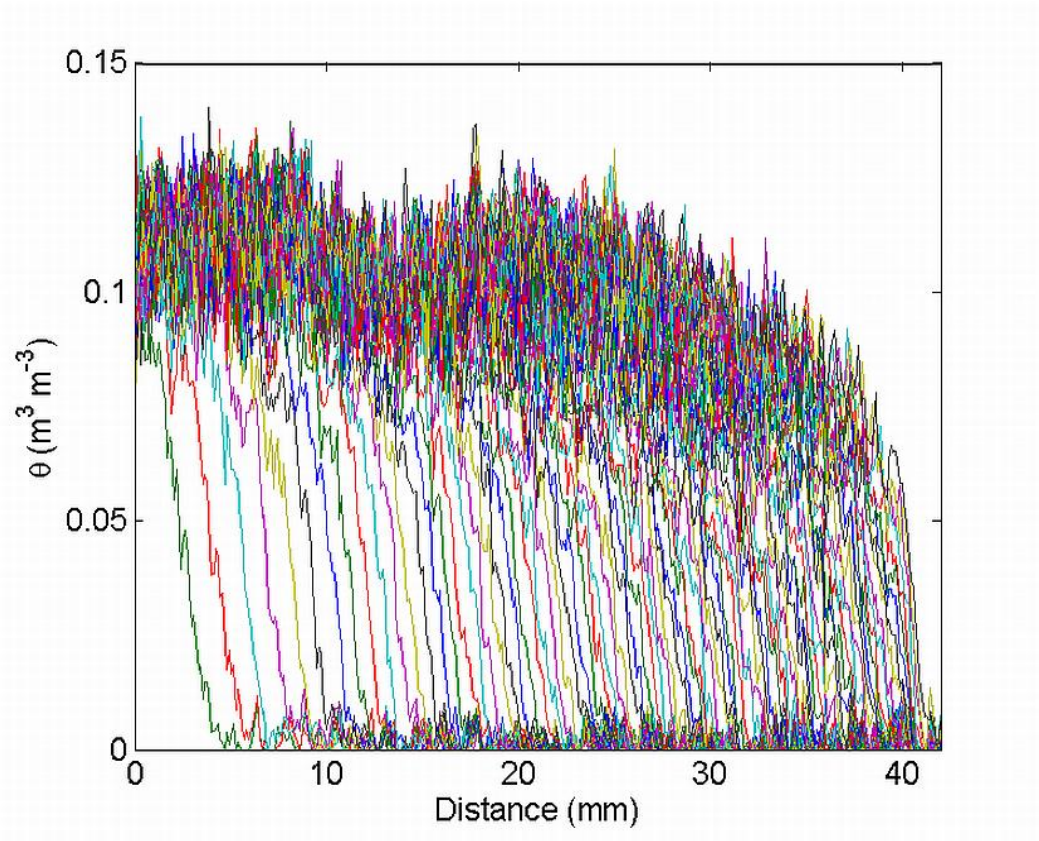

Figure 5- 3 Volumetric water content as a function of distance at different times (identified by different colors) for Berea core sample C3. The volumetric water contents were measured along the central vertical line from a total of 90 images.

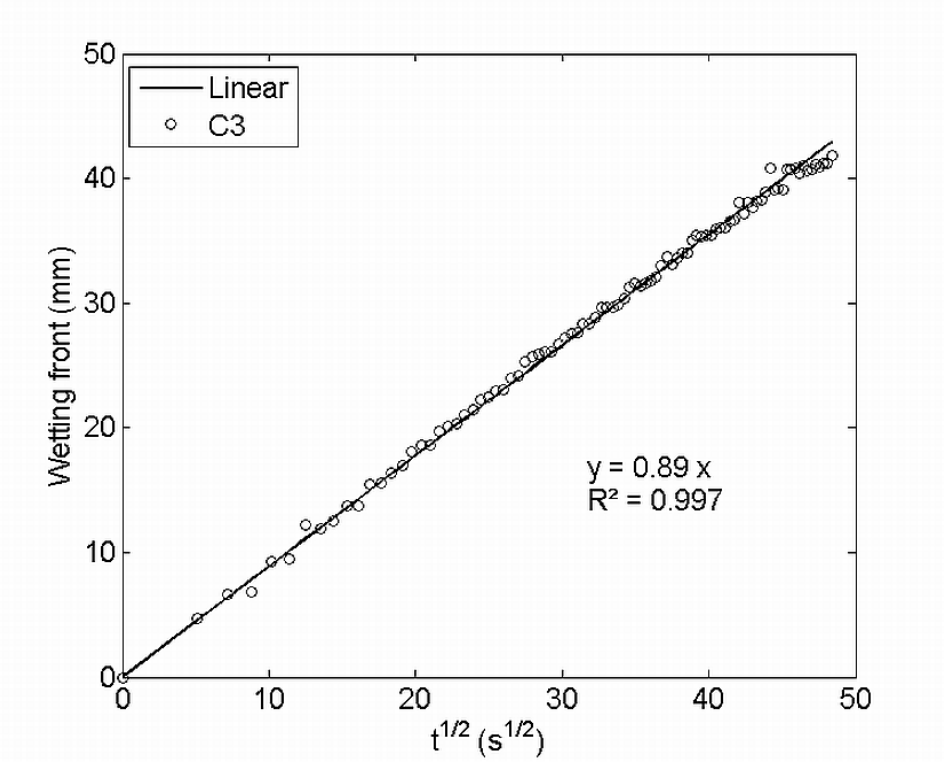

Figure 5- 4 Wetting front position as a function of the square root of time for 1-D vertical flow in Berea core sample C3. The slope of the linear regression is defined as the sorptivity.

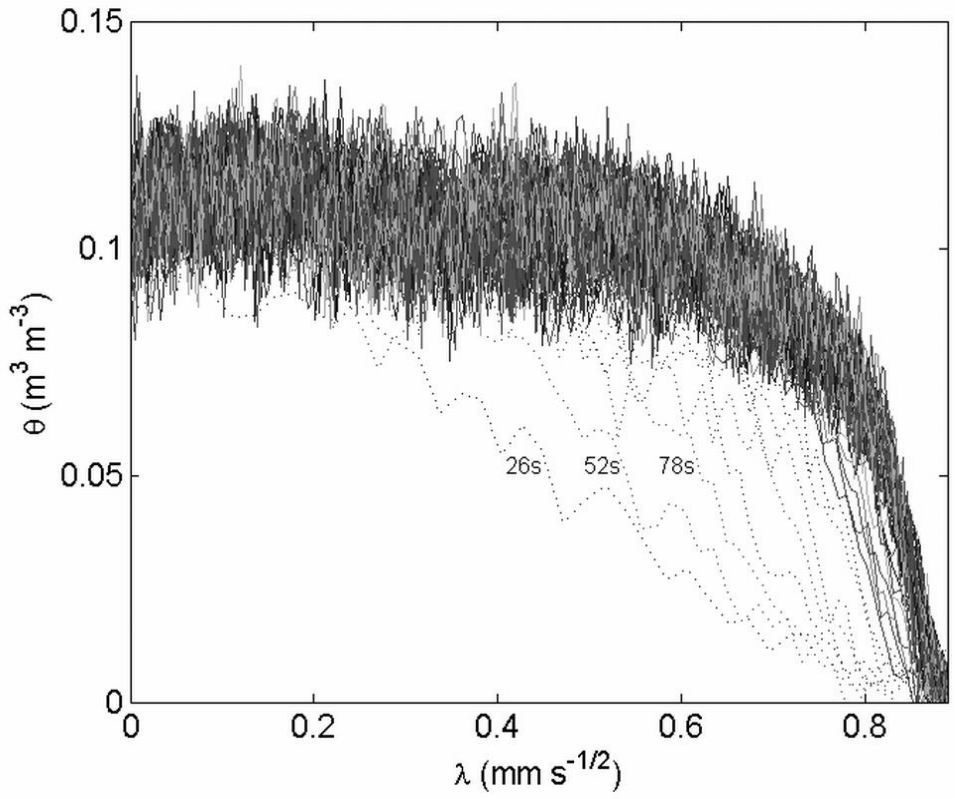

Figure 5- 5 Volumetric water content as a function of the Boltzmann variable, λ at different times (identified by different colors) for Berea core sample C3. Note: several curves (identified by dotted lines) at early times of imbibition deviate from the later stage curves which converge into a single function. First three early times are indicated separately.

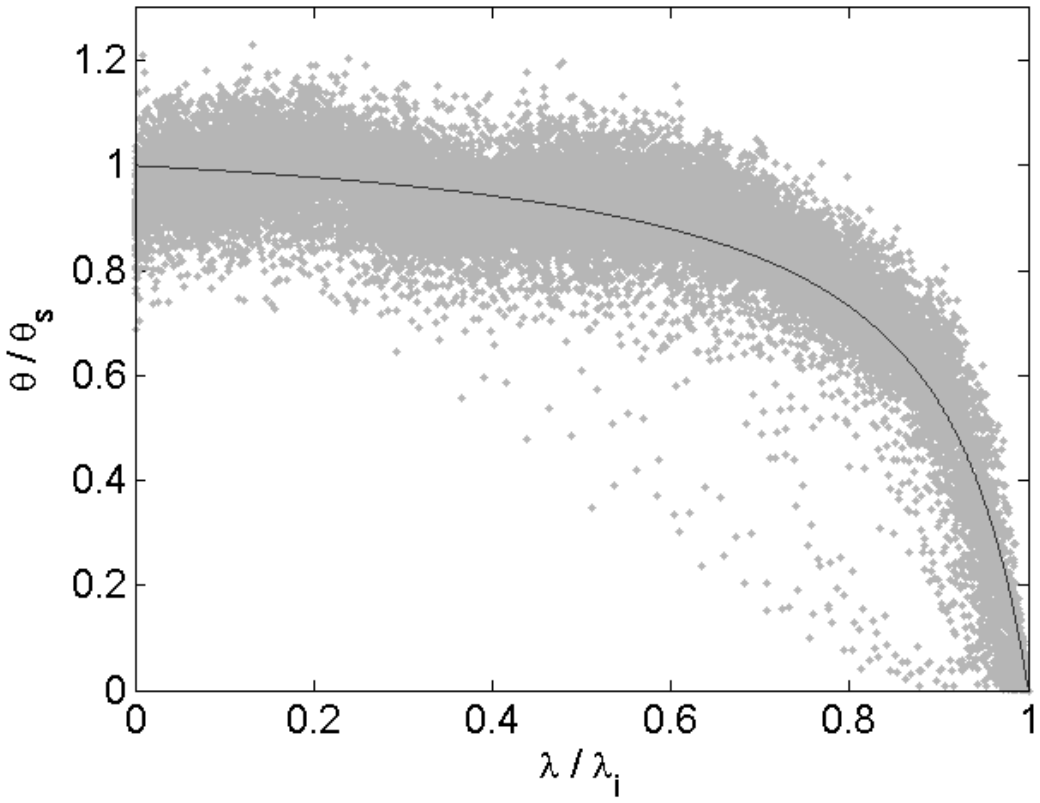

Figure 5- 6 The analytical solution (solid line), proposed by Meyer and Warrick (1990), fitted to the normalized water content versus normalized λ values (grey dots) for Berea core sample C3.

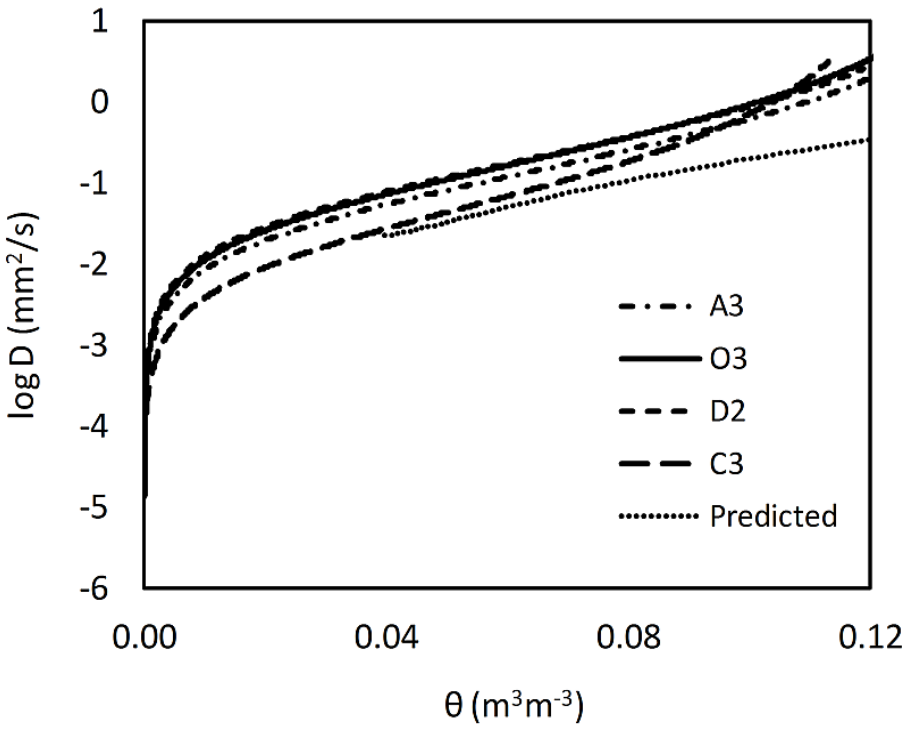

Figure 5- 7 Log diffusivity as a function of volumetric water content for the four replicate Berea core samples: A3, C3, D2, and O3. The predicted function was calculated from $K(\theta)$ and $dh/d\theta$ data for Berea sandstone using Eq. [2].

CHAPTER VI
CONCLUSIONS

Neutron radiographic imaging of calibration cells, Flint sand, and Berea Sandstone has been conducted at two neutron imaging facilities: NIST-NCNR BT-2 and HFIR CG1-D beamlines. In chapters I and II, I demonstrated that neutron radiography is a very effective tool for quantifying water content in porous media and for measuring the average water retention curve. Volumetric water contents determined by neutron radiography were calculated on a pixel by pixel basis using an empirical calibration equation after taking into account beam hardening, scattering, and geometric corrections. The volumetric water content estimates from neutron imaging showed good agreement with experimental data measured independently by the hanging water column method. The van Genuchten model provided a good fit to the average water retention functions from neutron imaging and the hanging water column method.

In chapter III, I directly determined point water retention functions for Flint sand at selected 115 points (pixels) using neutron radiography and parameterized them using the Brooks and Corey (1964) model. The median and mean values of the point Brooks and Corey parameters were compared with parameter estimates from the TrueCell inverse model applied to average water retention curve data. The point water retention function constructed using the median parameter values corresponded more closely with the point function inversely extracted by TrueCell than did the curve produced by the means of the parameter estimates. This was due to skewed nature of the histograms for some of the point Brooks and Corey parameters. The cumulative outflows simulated by the HYDRUS 1-D numerical model using these measured and inversely estimated point parameters were very similar to those measured independently with a pressure transducer.

In chapter IV, four cylindrical Berea sandstone cores were selected to observe temporal changes in the spatial distribution of water during imbibition using neutron radiography. I investigated dynamic water flow in Berea Sandstone and the results showed a linear relationship between the distance of the wetting

front and the square root of time. The first reported sorptivity and diffusivity values for Berea Sandstone were calculated from analyses of the neutron radiographs.

Numerical models are important tools for evaluating, designing, and implementing environmental and energy related problems such as geologic storage of CO_2, shale gas extraction, and enhanced oil recovery. Hydraulic parameters are needed for numerical models to predict the movement of these fluids in both unfractured and fractured porous media. However, only limited experimental data are available for model inputs, especially for those applications with high temperature and pressure settings. Future research using quantitative neutron radiography may provide more accurate estimates of these input parameters. Special aluminum pressure cells will need to be constructed for this application since the hanging water column method is limited to relatively low capillary pressures. Additional work is needed to address the issue of scattering from samples with large water thicknesses and/or placed close to the detector. Experimental determination of the scattering component might be explored as an alternative to sample specific calibration and Monte Carlo modeling of the point scattered function. Neutron imaging of a range of natural soils would also be beneficial to the soil science community; such an application, however, will require additional detailed calibrations to account for the presence of hydrogen in organic matter. Finally, neutron tomography could be very useful for investigating hysteresis of the capillary pressure-saturation function if it were able to discriminate between air-fluid interfaces during wetting and drying.

MAIN APPENDIX

This main appendix contains a paper published by Warren et al in 2013 as a part of ORNL Laboratory Directed Research and Development (LDRD) program to investigate water transport in plant utilizing the HFIR R&D CG-1 beamline. Misun Kang performed 2-D image processing and participated in collection of data and the revision of the manuscript.

Warren J.M., H.Z. Bilheux, M. Kang, S. Voisin, C.L. Cheng, E. Perfect, J. Horita, 2013. Neutron Imaging Reveals Internal Plant Hydraulic Dynamics. Plant and Soil, DOI: 10.1007/s11104-012-1579-7.

Abstract

Background and aims Knowledge of plant water fluxes is critical for assessing mechanistic processes linked to biogeochemical cycles, yet resolving root water transport dynamics has been a particularly daunting task. Our objectives were to demonstrate the ability to non-invasively monitor individual root functionality and water fluxes within Zea mays L. (maize) and Panicum virgatum L. (switchgrass) seedlings using neutron imaging.

Methods Seedlings were propagated for 1–3 weeks in aluminum chambers containing sand. Pulses of water or deuterium oxide were then tracked through the root systems by collecting consecutive radiographs during exposure to a cold-neutron source. Water flux was manipulated by cycling on a growth lamp to alter foliar demand for water.

Results Neutron radiography readily illuminated root structure, root growth, and relative plant and soil water content. After irrigation there was rapid root water uptake from the newly wetted soil, followed by hydraulic redistribution of water through the root system to roots terminating in dry soil. Water flux within individual roots responded differentially to foliar illumination based on supply and demand of water within the root system.

Conclusions Sub-millimeter scale image resolution revealed timing and magnitudes of root water uptake, redistribution within the roots, and root-shoot hydraulic linkages—relationships not well characterized by other techniques.

Introduction

Water flux through the soil-plant-atmosphere continuum is mediated by hydraulic conductivity of soil, plant roots, stems and leaves, which vary widely in their ability to facilitate water transport along this water potential energy gradient (Sperry et al. 1998). Mechanistic knowledge of these soil-plant water flux dynamics is a critical component of modeling land-atmosphere water and carbon exchanges (e.g., Lawrence et al. 2007); however, models require knowledge of root architecture and water uptake for validation and parameterization, data that are scarce and difficult to obtain (Hopmans and Bristow 2002; Javaux et al. 2008). Despite decades of investigation, in situ quantification of soil-plant water fluxes have not been fully successful due to a lack of suitable techniques capable of revealing roots or water fluxes at relevant spatial scales (μm to mm) (Pierret et al. 2005; Rewald et al. 2011). Direct physical sampling of soil water or roots can damage the delicate rhizosphere and xylem, thereby confounding subsequent interpretation of root function. Installations of soil or plant water sensors are similarly invasive, and represent only point measurements that integrate over a large area (multiple cm). Such caveats have led to exploration of non-invasive techniques to assess plant water content and fluxes including isotope (Waring and Roberts 1979; Nakanishi et al. 2003) or dye (Varney and Canny 1993; Querejeta et al. 2003) tracers, 2D light transmission (Garrigues et al. 2006), acoustics (Johnson et al. 2012), heat flow (Baker and van Bavel 1987), nuclear magnetic resonance (Van As 2007), X-ray (Pierret et al. 2003) and more recently, neutron imaging (Matsushima et al. 2008a, 2009; Oswald et al. 2008; Esser et al. 2010). Neutrons are ideally suited for this task since they readily

penetrate most common materials but are strongly attenuated by those containing hydrogen such as water. Root architecture (Moradi et al. 2009), root growth (Menon et al. 2007) and soil and plant water distribution (Nakanishi et al. 1999; Oswald et al. 2008; Tumlinson et al. 2008; Carminati et al. 2010; Moradi et al. 2011; Cheng et al. 2012) are thus readily imaged and quantified through calibration (Tumlinson et al. 2008; Oswald et al. 2008; Moradi et al. 2009; Kang et al. 2013) using neutron radiography. The desire to also track water fluxes through the soil-plant continuum has led to experimentation with positron emission tracers (e.g., 18F; Nakanishi et al. 2003) or deuterium oxide (D_2O) tracers (Matsushima et al. 2008a, 2009; Zarebanadkouki et al. 2012), paired with neutron imaging. D_2O has a much smaller neutron crosssection than H_2O, which allows for pulse-chase experiments that can reveal water uptake or transport through linkage to changes in image contrast. Indeed, prior tracer work does show progressive change in contrast within stems of hibiscus, tomato and rose, major roots of tomato (Matsushima et al. 2008a, b, 2009) and lupine roots (Zarebanadkouki et al. 2012), which illustrates the utility of D_2O to evaluate xylem water flux in situ. Attenuation of the neutron beam by H_2O or D_2O in plant tissues can be imaged using a charge-coupled device (CCD) camera at sufficient resolution to reveal dynamics in the sphere of hydration that exists in the rhizosphere around individual roots and relative hydration of plant tissue (Nakanishi et al. 2005; Moradi et al. 2011). Fine root hydration varies as soils dry (Domec et al. 2004), and the threshold between reversible loss of function and catastrophic failure has not been resolved. Individual root functionality is not readily assessed in situ, and therefore information regarding root capacity for water uptake under varying environmental conditions is largely absent. Data are needed to identify or verify soil hydraulic properties, dynamics of root and rhizosphere water uptake, xylem transport rates, and ultimately to inform models of soil or plant water flux (e.g., HYDRUS 2-D, STOMP, SWAP, SWMS_2D). Our objectives in this study were to use H_2O, D_2O and neutron imaging to assess root distribution in situ; assess the ability of individual fine roots to uptake and

redistribute water; and subsequently track the transport of that water through the soil-plant-atmosphere continuum.

Materials and methods

Neutron imaging

Neutron imaging is a non-invasive non-destructive imaging technique that is complementary to other imaging techniques such as NMR, X-ray or gamma imaging (Strobl et al. 2009; Bilheux et al. 2013). Due to the interaction properties of neutrons with matter, some light nuclei such as H and D greatly scatter neutrons, whereas some heavier elements such as Al, Si (e.g., SiO_2 – sand), Cu or Pb are not strong scatterers or absorbers of neutrons and can therefore be easily penetrated. Neutron radiography measures the attenuation of a neutron beam caused by absorption and scattering within a sample using a two-dimensional position sensitive detector that measures the transmitted neutron flux (Strobl et al. 2009). The beam attenuation caused by a homogeneous uniformly thick sample composed of a single isotope is given by

$$I(\lambda) = I_0(\lambda)e^{-\mu(\lambda)\Delta x}$$

where I_0 and I are, respectively, the incident and transmitted beam intensities, μ is the attenuation coefficient and Δx is the thickness of the sample. The attenuation coefficient μ is given by

$$\mu(\lambda) = \sigma_t(\lambda)\frac{\rho N_A}{M}$$

where $\sigma_t(\lambda)$ is the material's neutron cross section, ρ is density, N_A is Avogadro's number, and M is the molar mass.

Neutron computed tomography (NCT) measures attenuation of a neutron beam in three dimensions by rotating a sample to record attenuation for multiple beam paths through an object. Straightforward extension of these basic formulas underpins the radiography of heterogeneous and irregularly shaped objects.

Computational reconstruction permits visualization and quantification of the sample in three dimensions.

Plant propagation

Zea mays L. (maize) or *Panicum virgatum* L. 'Trailblazer' (switchgrass) seedlings were grown in aluminum chambers, either rectangular (2.38 × 2.58 cm ID × 6.3 cm tall; 0.055 cm Al thickness), cylindrical (2.54 cm ID × 8.0 cm tall; 0.035 cm Al thickness) or constructed from thin, wide plates (1.05 ID × 15 × 17 cm; 0.31 cm Al thickness) containing fine (F) or course (C) grained sand with most particle sizes ranging from 0.1-0.3 mm (94%) or 0.3-0.6 mm (97%), respectively (F70 or Flint #13, U.S. Silica Company, Berkeley Springs, WV). Treated maize seeds (Silver Queen, Mayo Garden Centers, Knoxville, TN) or switchgrass seeds were germinated, then planted just below the sand surface and propagated in an onsite growth chamber adjacent to the beam line. A balanced fertilizer with micronutrients was initially applied to the sand. The growing regime used a 16 h day at 23/20 °C (day/ night), with photosynthetically active radiation (PAR) from 300-550 µmol m^{-2} s^{-1}. Replicate plants were maintained under relatively dry conditions, with daily additions of 1-7 ml of water to replace loss from evapotranspiration based on chamber weight, thus balancing plant viability with minimum soil water content. Imaging improves as the integrated cross-sectional H concentration declines. Water was withheld for 12-24 hours prior to initial imaging to maximize neutron penetration for radiographic assessment of 2D or 3D root architecture, and for radiographic tracking of water or D_2O pulses through the system. Volumetric soil water content (θ) in these cases ranged from 0.02-0.07 cm^3 cm^{-3} (for NCT) or 0.05 to 0.10 cm^3 cm^{-3} (for radiography).

Neutron imaging experiments

Neutron imaging was performed using cold neutrons at the High Flux Isotope Reactor (HFIR) CG1-D beam line at Oak Ridge National Laboratory.

Neutron attenuation by the plant samples was detected with a 25 μm LiF/ZnS scintillator linked to a CCD camera system (iKon-L 936, Andor Technology plc. Belfast, UK). The resulting field of view was ~7×7 cm with image resolution ~100 μm per pixel. The large Al plate chambers were significantly larger than our detector system, thereby requiring multiple images as the chamber was moved left, right, up and down in front of the detector using a robotic stage. Sixteen 300-s composite images were collected across the large plate chambers then spliced together to provide a view of the entire system, which allowed for selection of specific areas for focused radiography during irrigation events. A variety of different plant neutron imaging experiments were conducted to assess root architecture, growth and water flux dynamics using pulses of H_2O or D_2O (99.8 %; Cambridge Isotope Laboratories, Inc., Andover, MA, USA) added to the system—four key experiments are highlighted. The first experiment initially assessed the root structure of 20-d old maize and switchgrass plants growing together in a large plate chamber. A location composed primarily of maize roots in the center of the chamber was then selected for repeated measurements through time following a pulse of water. After initial imaging, 2 ml of H_2O were added with a syringe through an injection hole at the base of the chamber and repeated 300-s images were collected over the next 4 h. The second experiment also used a large plate chamber, in this case containing 15-d old maize seedlings. Five days prior to imaging, the daily incremental additions of H_2O were changed to D_2O in an effort to enhance image contrast. After an initial injection of 7 ml D_2O at the base of the chamber, daily additions ranged from 0 to 3 ml D_2O until imaging. Following initial composite imaging, an area was selected near the top of the chamber which included two germinated and one non-germinated seed hulls, one large sinker root, and multiple lateral roots. Initial 300-s images were collected, and then 9 ml of H_2O was injected at the base of the chamber. Images were collected over the next 12 h. The same focused area was also imaged once daily for the next 6 days to assess longer term fate of the irrigation pulse, as well as root growth. The last two studies focused on single maize seedlings growing

in cylindrical or rectangular Al chambers. Tomography of the two 10-day old maize seedlings was conducted over a 13 h period, with 360 two-minute (120-s) images collected at 0.5° intervals. The seedlings' leaves were covered with aluminum foil to minimize water loss during tomography. Following the tomography, 3 ml of D_2O was injected onto the surface soil of each chamber, and then ~320 consecutive 120-s radiographic images were collected over the next 12 h, during which time a high pressure sodium lamp suspended over the seedlings was cycled on and off; background PAR was <20 µmol m^{-2} s^{-1} when off, and was 350-550 µmol m^{-2} s^{-1} when on, depending on canopy height. The lamp allowed manipulation of photosynthetic rate, thereby regulating plant water loss and the water potential driving forces responsible for root water uptake and transport through the system. Data processing and analysis 2D neutron images were normalized through darkfield and open-beam corrections, and despeckled to remove background gamma ray contamination using ImageJ (Version 1.45 s, National Institutes of Health, Bethesda, MD, USA) or MATLAB (Version 7.11, Mathworks, Natick, MA, USA) software programs (Kang et al. 2013). To assess changes in water flux through time, radiographic image sequences were subtracted or divided by the initial image that was collected prior to irrigation (for the plate chambers), or within the first 3 min following injection of a H_2O or D_2O pulse (for the small cylindrical and rectangular chambers). The division proved most illustrative of changes in the system and was used to assess relative change in water content within soil and plant tissue through time. A subset of repeated radiographs was stacked together to generate a sequential video of water transport for two small maize replicates. For these seedlings, ~30 selected regions of interest (ROI) were delineated around individual root sections, root free soil, stem and leaf segments using the 3D reconstruction of the root structure (Videos S1 and S4) as a guide to assess areas of non-overlapping roots. Changes in each ROI were tracked through time to reveal patterns of water flux through the soil and roots and plant stem. Mixed model repeated

measures analysis (SAS) was used to test for significant differences ($P<0.05$) in rates of change between ROI through time.

Results and discussion

In our study, we utilized neutron imaging to reveal root architecture and water movement through model plants in response to dynamic supply and demand of various tissues. The results demonstrate the ability of this technique to rapidly monitor individual root functionality, root uptake, redistribution and release of water in young (1 to 3 week-old) *Zea maize* L. (corn) seedlings. The data support two novel findings that provide a platform for further investigation of root water dynamics: 1) direct evidence of individual root functionality and response to changing environmental conditions, and 2) direct evidence of root-mediated hydraulic redistribution of soil water to rehydrate drier roots—a process that has previously only been assessed indirectly.

Experiment 1 – Imaging roots following pulse of H_2O – root architecture

In the first experiment, neutron imaging clearly revealed the distribution of maize and switchgrass roots growing in sand within the flat Al chamber (Fig. 1A). Most roots proliferated in the finer textured soil in between layers of coarse soil, as expected, since the finer soil had a much greater surface area, and therefore water and nutrient holding capacity. Fungal hyphae within the soil appeared as fuzzy dark masses, as their diameters are 1–2 orders of magnitude less than the 100 μm resolution of the detector. Even so, a sphere of hydration from the fungi was evident, particularly around the switchgrass roots. There was also a triangular pattern of varying water content evident in the lower center of the composite image that represents varying soil porosity due to a separation of particle sizes as dry sand was initially added to the system. Subsequent experiments used moistened sand during filling to reduce this artifact. There was

no evidence of water flux through the system over a 4 h period of monitoring after injection of 2 ml of H_2O at the base of the chamber. The small amount of water added, limited root access to depth, large water potential gradients within the soil, and minimal change in image contrast likely limited detection of any direct root water uptake in this case.

Experiment 2 – Imaging partially deuterated roots following pulse of H_2O – root rehydration

In an attempt to improve the potential for detecting direct root uptake of water, the soil-plant system was partially deuterated for the second set of experiments. Deuteration improves the image contrast between existing water in soil/roots and added water—the added water is darker; i.e., reduces neutron transmission more than a mixture of H_2O:D_2O in the roots, so root uptake of pure water should be easily detected. Cellular replacement of hydrogen with deuterium has long been used as a contrast agent to examine structural biology of proteins and other molecules; however, full deuteration has not been possible with higher plants whose vigor declines above 40–60 % deuteration (Katz and Crespi 1966). Nonetheless in our study, isolated pulses of pure D_2O had no visible impact on plants previously propagated in H_2O. Root uptake, transport and foliar release of deuterium were visibly evident based on post-irrigation foliar rehydration, continued root and foliar expansion, and declining mass of the plant-soil system to pre-irrigation levels. While D_2O can ultimately impact cellular processes, its movement through plant xylem is equivalent to water such that D2O can be used to assess short-term patterns of mass flow through soil, roots and the transpiration stream. In the second study maize roots were clearly identifiable in this system, and most roots proliferated in the upper fine soil layer (Fig. 2A). The main radical sinker root from the targeted seedling grew through the coarse sand to the bottom of the chamber. After application of a much larger pulse of H_2O than used in the first experiment (9 ml as compared with 2 ml), sequential neutron radiography revealed a substantial rehydration of this root as

evidenced by its strong increase in contrast through time (Fig. 2A-c). The increase in contrast occurs as new water (H_2O) is taken up by the root, mixes with and displaces existing water and D_2O within the root. Root water transport to the kernel, and to new root initials arising from the kernel was also evident by changes in contrast, and indicates new water influx into those structures over the 12 h period. Root tips further away from the hull also became more visible, although much of the contrast change in images of these roots was caused by root tip elongation; new hydrated root tissue occupying previously dry soil. An adjacent kernel and other roots dehydrated over the initial 12 h imaging period, as indicated by the dark areas in the image (Fig. 2A-c). The relative change in contrast after 12 h indicates substantial extraction and flux of existing soil and plant water (dark pixels) or new influx of new soil and plant water (white pixels) (Fig. 2A-d). Repeated imaging of the maize roots over the 6 day period revealed substantial rehydration of previously dehydrated roots, and subsequent growth of those and other roots. Active root tips highlighted in white in Fig. 2A-c grew >2 cm during this period, out of the field of view. The newly emerging roots grew ~4 cm. Dehydrated roots that appeared dark in Fig. 2A-c did eventually rehydrate, and then grew 1.0–2.5 cm. Dynamic changes in root size due to growth or relative hydration complicates quantification of H_2O or D_2O within the system. Root dehydration or rehydration may or may not be accompanied by a change in tissue size, either shrinking or swelling depending on morphology (e.g., degree of suberization) and the dynamics of xylem embolism, cavitation and refilling. Such processes are not easily represented by models, which often assume a constant root size and water content (e.g., Zarebanadkouki et al. 2012). Initial modeling of relatively moist lupine root uptake and internal transport of water and deuterium based on neutron imaging is promising (Zarebanadkouki et al. 2012), but extension to drier soil conditions such as used in this study may require additional consideration of tissue size and hydration.

Experiment 3 – Imaging roots following pulse of D_2O – individual root water uptake in response to PAR

For the last two experiments, water fluxes were tracked through 10-day old *Zea mays* seedlings following surface irrigation with D_2O. Since D has much lower neutron attenuation than H, D_2O displacement of existing H_2O within the plant vascular system, or influx of D_2O into previously dry tissue or soil was readily tracked by changes in image intensity through time. The added D_2O penetrated the chambers rapidly, dispersing fairly uniformly through the soil in the first chamber and pooling at the bottom, but flowing only down one side to the bottom in the second chamber, leaving a large area of dry sand and roots Using the first maize replicate chamber, root-shoot linkages were explored by tracking individual root and stem tissue responses to intensity of photosynthetically active radiation (Parsons and Kramer 1974), which was manipulated by cycling the lamp on and off (Fig. 3A, Videos S1–S2). The relative functional importance of individual roots was highlighted by their response to shoot demand for water (Fig. 4A), which varied with PAR. When the lamp was cycled on, leaf stomata opened and an internal water potential gradient developed which drove water flux through the soil plant-atmosphere continuum. This resulted in a rapid increase in root water uptake following irrigation, but after ~30 min (roots 1&2) or 45 min (root 3) water transport from the roots to the shoot exceeded root water uptake as shown by a decline in root water content, which then recovered when the lamp cycled off. A large pulse of water from root 1 into the stem occurred when the lamp was cycled back on after ~3 h (Fig. 4A); this can be visualized in Video S2. The data indicated quite varied and differential functionality of the highlighted roots. Pulses of water were identified moving concurrently into and out of different roots, stem and even leaf sections as water demand by the various structures changed. Differences in root morphology, uptake capacity, pathway resistances, and water potential gradients certainly contributed to the heterogeneity of root response.

Experiment 4 – Imaging roots following pulse of D_2O – hydraulic redistribution and rehydration of roots in dry soil

Root-root linkages were further explored by tracking individual roots in either dry or wet soil. For the second maize replicate (Fig. 5A, Videos S3–S4), the applied D_2O wetted the surface soil, then infiltrated along the left side of the sample chamber, resulting in areas of distinct moist or dry soils. Roots existed throughout the chamber, including several lateral roots extending off the main radical into an area that remained dry after irrigation. Two of these roots terminated in the dry soil area, while several others grew down the edge of the chamber terminating in the deeper, wetter soil. This created distinct water potential gradients within the chamber that could facilitate internal redistribution of water within the root system (i.e., hydraulic redistribution (HR); Caldwell and Richards 1989). Within 2 min there was evidence of root water uptake from the newly wetted soil, which increased rapidly for those roots in the wet soil, followed by HR of water through the root system to roots terminating in dry soil (Fig. 6A, Video S3). After 18 min water uptake by wet roots and HR to dry roots was the same through time—plateauing after 3 h. Greater than 90 % of root rehydration due to HR was achieved during the first hour after irrigation, when the lamp was on. There was no discernible change in HR in response to the light cycling off. The rehydration of dry roots appears to be root mediated, as the dry soil surrounding the dry roots (above and below) remained dry over a 12 h period suggesting minimal unsaturated liquid or vapor water flow to the roots, or alternately root water efflux to the soil. The impact of PAR on plant water flux was also apparent for this chamber, particularly in the changing hydration of the stem and leaf sections, which intermittently and progressively rehydrated over the 12 h period. This final study provided direct evidence for root-mediated hydraulic redistribution of soil water to rehydrate drier roots—a process that has previously only been assessed indirectly. The performance of neutron imaging was strongly affected by total water content in the system, such that drier samples were preferable. The tradeoff between exposure time and resolution did not affect the

ability to image water flux in 2-D, however 3-D tomography required significant exposure time that constrained the types of experiments conducted. For example, water flux through the system occurs on the order of minutes, whereas even low-resolution tomography would take an hour or longer. Imaging was limited by beam width and detector size such that only small plant/soil systems could be imaged in their entirety; however, targeted water flux within a specific region of larger systems was easily monitored following initial scanning of the entire system. Using larger systems also allows for manipulation of conditions in remote areas of the system, to elicit responses in the localized, imaged areas. In this study, manipulations included pulses of H_2O, D_2O or changing PAR outside the field of view. In the future, improvements in optics and detectors should allow neutron imaging resolution to improve to the point that processes on the order of seconds to minutes at scales of 1–20 μm might be imaged, such as water dynamics within individual cells (e.g., refilling of cavitated xylem), processes currently studied in stems and leaves using MRI or X-ray techniques (e.g.,VanAs et al. 2009; Kimand Lee 2010). However, neutron imaging is likely to be most beneficial for study of myriad mechanistic plant processes at the scale of individual organs, and in context of genotypic and phenotypic response to changing environmental or biological conditions (e.g., aquaporin function, water or nutrient availability, root-mycorrhizae interactions, competition).

Conclusions

The careful use of D_2O in our pulse-chase experiments, but not pulses of water alone, readily allowed monitoring of internal root water flux in situ. This work builds upon recent neutron imaging studies focused on soil and root-rhizosphere water dynamics (Oswald et al. 2008; Carminati et al. 2010; Moradi et al. 2011). Those studies found heterogeneous patterns of root water extraction and soil drying, and identified the rhizosphere as a unique environment that remained

much moister than the bulk soil during drying. Other studies have successfully illustrated internal xylem water transport through stems and leaves using D_2O (Nakanishi et al. 2003; Matsushima et al. 2008a; Zarebanadkouki et al. 2012). In our study, neutron imaging was used to assess high-resolution uptake of soil water by individual maize roots, redistribution of water within the root system, and water transport through the stem to the atmosphere. The dynamic internal demand for water between soil, individual roots, stems and leaves was readily visualized and quantified illustrating the value of this technique to assess root-root and root-shoot responses to changing environmental conditions. Such data can be used to validate prior indirect measurements of water flux, investigate how water uptake is associated with root size and root order and be extended to assess the uptake and transport of soil water by individual roots through the stem and out to the atmosphere.

Acknowledgments

We thank Stan Wullschleger for discussion, Terry Pfeiffer for editorial assistance, Lowell Crow and Lakeisha Walker for beam line assistance and J-C Bilheux and Keely Willis for image reconstruction. Research was sponsored by the Laboratory Directed Research and Development Program of Oak Ridge National Laboratory, managed by UT-Battelle, LLC, for the U.S. Department of Energy under contract DEAC05-00OR22725, and by the Joint Directed Research and Development Program with the University of Tennessee –Knoxville. The High Flux Isotope Reactor is supported by the Division of Scientific User Facilities, Office of Basic Energy Sciences, U.S. Department of Energy.

References

Baker JM, van Bavel CHM (1987) Measurement of mass-flow of water in the stems of herbaceous plants. Plant Cell Environ 10:777–782

Bilheux H, Crawford K, Walker L, Voisin S, Kang M, Harvey M, Bailey B, Phillips M, Bilheux J-C, Berry K, Anknera J, Warren J, Nanda J, Pannala S, Lance M (2013) Neutron imaging at the Oak Ridge National Laboratory: present and future capabilities. Physics Procedia (in press)

Caldwell MM, Richards JH (1989) Hydraulic lift: water efflux from upper roots improves effectiveness of water uptake by deep roots. Oecologia 79:1–5

Carminati A, Moradi AB, Vetterlein D, Vontobel P, Lehmann E, Weller U, Vogel H, Oswald SE (2010) Dynamics of soil water content in the rhizosphere. Plant Soil 332:163–176

Cheng CL, Kang M, Perfect E, Voisin S, Horita J, Bilheux HZ, Warren JM, Jacobson DL, Hussey DS (2012) Average soil water retention curves measured by neutron radiography. Soil Sci Soc Am J 76:1184–1191

Domec JC, Warren JM, Meinzer FC, Brooks JR, Coulombe R (2004) Native root xylem embolism and stomatal closure in stands of Douglas-fir and ponderosa pine: mitigation by hydraulic redistribution. Oecologia 141:7–16

Esser HG, Carminati A, Vontobel P, Lehmann EH, Oswald SE (2010) Neutron radiography and tomography of water distribution in the root zone. J Plant Nutr Soil Sci 173:757–764

Garrigues E, Doussan C, Pierret A (2006) Water uptake by plant roots: I. Formation and propagation of a water extraction front in mature root systems as evidenced by 2D light transmission imaging. Plant Soil 283:83–98

Hopmans JW, Bristow KL (2002) Current capabilities and future needs of root water and nutrient uptake modeling. In: Sparks DL (ed) Advances in agronomy. Academic, San Diego, pp 104–175

Javaux M, Schröder T, Vanderborght J, Vereecken H (2008) Use of a three-dimensional detailed modeling approach for predicting root water uptake. Vadose Zone J 7:1079–1088

Johnson DM, McCulloh KA, Woodruff DR, Meinzer F (2012) Evidence for xylem embolism as a primary factor in dehydration-induced declines in leaf hydraulic conductance. Plant Cell Environ 35:760–769

Kang M, Bilheux HZ, Voisin S, Cheng C, Perfect E, Horita J, Warren JM (2013) Water calibration measurements for neutron radiography: application to water content quantification in porous media. Nucl Instrum Methods A. doi:10.1016/j.nima.2012.12.112

Katz JJ, Crespi HL (1966) Deuterated organisms: cultivation and uses. Science 151:1187–1194

Kim HK, Lee SJ (2010) Synchrotron x-ray imaging for nondestructive monitoring of sap flow dynamics through xylem vessel elements in rice leaves. New Phytol 188:1085–1098

Lawrence DM, Thornton PE, Oleson KW, Bonan GB (2007) The partitioning of evapotranspiration into transpiration, soil evaporation, and canopy evaporation in a GCM: impacts on land–atmosphere interaction. J Hydrometeorol 8:862–880

Matsushima U, Kardjilov N, Hilger A, Graf W, Herppich WB (2008a) Application potential of cold neutron radiography in plant science research. J Appl Bot Food Qual 82:90–98

Matsushima U, Kardjilov N, Hilger A, Ueno M, Kawamitsu Y, Nishizawa T, Herppich WB (2008b) Visualization of water flow in tomato seedlings using neutron imaging. In: Arif M, Downing RG (eds) Neutron radiography. Destech Publications, Inc., Lancaster, pp 358–362

Matsushima U, Herppich WB, Kardjilov N, Graf W, Hilger A, Manke I (2009) Estimation of water flow velocity in small plants using cold neutron imaging with D2O tracer. Nucl Instrum Meth A 605:146–149

Menon M, Robinson B, Oswald SE, Kaestner A, Abbaspour KC, Lehmann E (2007) Visualization of root growth in heterogeneously contaminated soil using neutron radiography. Eur J Soil Sci 58:802–810

Moradi AB, Conesa HM, Robinson B, Lehmann E, Kuehne G, Kaestner A, Oswald S, Schulin R (2009) Neutron radiography as a tool for revealing root development in soil: capabilities and limitations. Plant Soil 318:243–255

Moradi AB, Carminati A, Vetterlein D, Vontobel P, Lehmann E, Weller U, Vogel H, Oswald SE (2011) Three-dimensional visualization and quantification of water content in rhizosphere. New Phytol 192:653–663

Nakanishi TM, Don-Jin K, Kitamura T, Ishii R, Matsubayashi M (1999) Identification of water storage tissue in the stem of cowpea plant (Vigna unguliculata Walp) by neutron radiography. J Radioanal Nucl Ch 242:353–359

Nakanishi TM, Okuni Y, Furukawa J, Tanoi K, Yokota H, Ikeue N, Matsubayashi M, Uchida H, Tsiji A (2003) Water movement in a plant sample by neutron beam analysis as well as positron emission tracer imaging system. J Radioanal Nucl Ch 255:149–153

Nakanishi TM, Okuni Y, Hayashi Y, Nishiyama H (2005) Water gradient profiles at bean plant roots determined by neutron beam analysis. J Radioanal Nucl Ch 264:313–317

Oswald SE, Menon M, Carminati A, Vontobel P, Lehmann E, Schulin R (2008) Quantitative imaging of infiltration, root growth and root water uptake via neutron radiography. Vadose Zone J 7:1035–1047

Parsons LR, Kramer PJ (1974) Diurnal cycling in root resistance to water movement. Physiol Plantarum 30:19–23

Pierret A, Kirby M, Moran C (2003) Simultaneous x-ray imaging of plant root growth and water uptake in thin-slab systems. Plant Soil 255:361–373

Pierret A, Moran CJ, Doussan C (2005) Conventional detection methodology is limiting our ability to understand the roles and functions of fine roots. New Phytol 166:967–980

Querejeta JI, Egerton-Warburton LM, Allen MF (2003) Direct nocturnal water transfer from oaks to their mycorrhizal symbiots during severe soil drying. Oecologia 134:55–64

Rewald B, Ephrath JE, Rachmilevitch S (2011) A root is a root is a root?Water uptake rates of citrus root orders. Plant Cell Environ 34:33–42

Sperry JS, Adler FR, Campbell GS, Comstock JP (1998) Limitation of plant water use by rhizosphere and xylem conductance: results from a model. Plant Cell Environ 21:347–359

Strobl M, Manke I, Kardjilov N, Hilger A, Dawson M, Banhart J (2009) Advances in neutron radiography and tomography. J Phys D Appl Phys 42:243001

Tumlinson LG, Liu H, Silk WK, Hopmans JW (2008) Thermal neutron computed tomography of soil water and plant roots. Soil Sci Soc Am J 72:1234–1242

Van As H (2007) Intact plant MRI for the study of cell water relations, membrane permeability, cell-to-cell and long distance water transport. J Exp Bot 58:743–756

Van As H, Scheenen T, Vergeldt FJ (2009) MRI of intact plants. Photosynth Res 102:213–222

Varney GT, Canny MJ (1993) Rates of water uptake into the mature root system of maize plants. New Phytol 123:775–786

Waring RH, Roberts JM (1979) Estimating water flux through stems of scots pine with tritiated-water and P-32. J Exp Bot 30:459–471

Zarebanadkouki M, Kim YX, Moradi AB, Vogel H-J, Kaestner A, Carminati A (2012) Quantification and modeling of local root water uptake using neutron radiography and deuterated water. Vadose Zone J 11: doi: 10.2136/vzj2011.0196

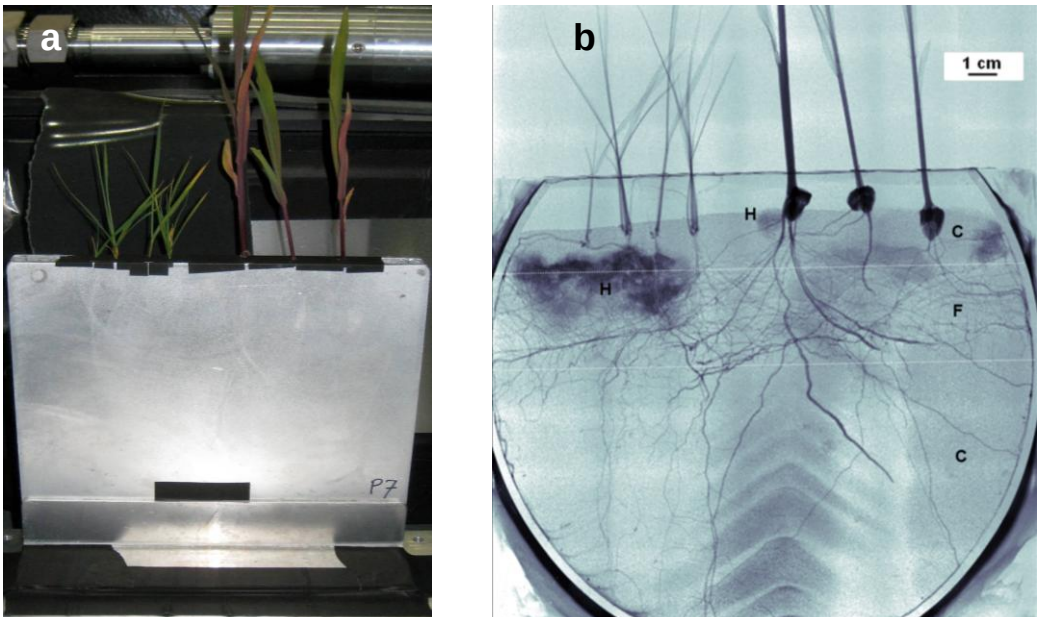

Figure A 1. a) Photograph of *Zea mays (right) and* Panicum virgatum *(left)* seedlings in a flat aluminum chamber in the HFIR CG1-D cold neutron beam line; black tape at base covers a water injection port. b) Composite neutron radiograph of (a) revealing detail of the plant and soil structure based principally on neutron scattering of hydrogen (as H_2O). Layers of course (C) or fine (F) sand within the aluminum chamber are roughly delineated by white horizontal lines. Dark areas (H) around the switchgrass root systems and in several locations near maize roots are likely arbuscular mycorrhizal or saprotrophic fungal hyphal masses. Sixteen, 120 s radiographs were spliced together to produce this image; resolution is ~100 µm.

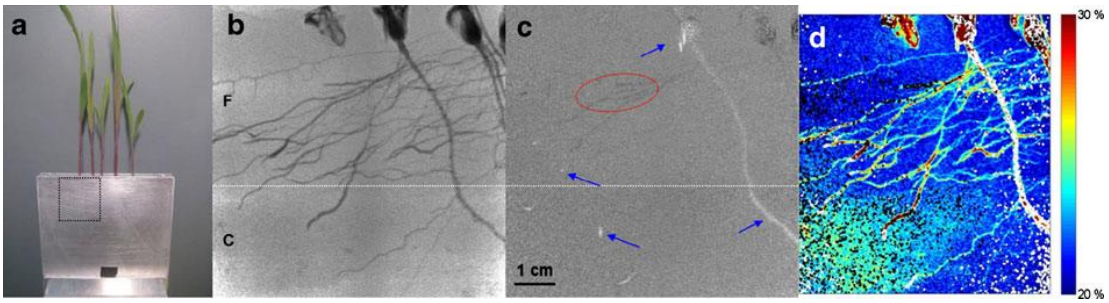

Figure A 2. a) Partially deuterated maize seedlings growing in sand in an aluminum chamber (~15 x 17 x 1 cm); square outline delineates area of focused neutron radiography; black tape at base covers an injection port for D_2O or H_2O; b) neutron radiographic image of root systems growing in course (C) and fine (F) sand; c) the same system 12 h after injection of H_2O at base of container *divided* by the initial image illustrating root water uptake, rehydration and transport to the growing root tips in white (blue arrows). Darker areas of the image indicate drying seed hulls or root systems that have lost water and likely cavitated in black (red oval). Note the non-germinated seed hull is not visible indicating no change in hydration; d) Relative neutron transmittance through the chamber as affected by the sand, moisture and plant tissue (blue indicates greater transmittance, red indicates greater absorbance and scattering). White or black pixelated areas indicate >10 % increase (white) or decrease (black) in water content over the 12 h period

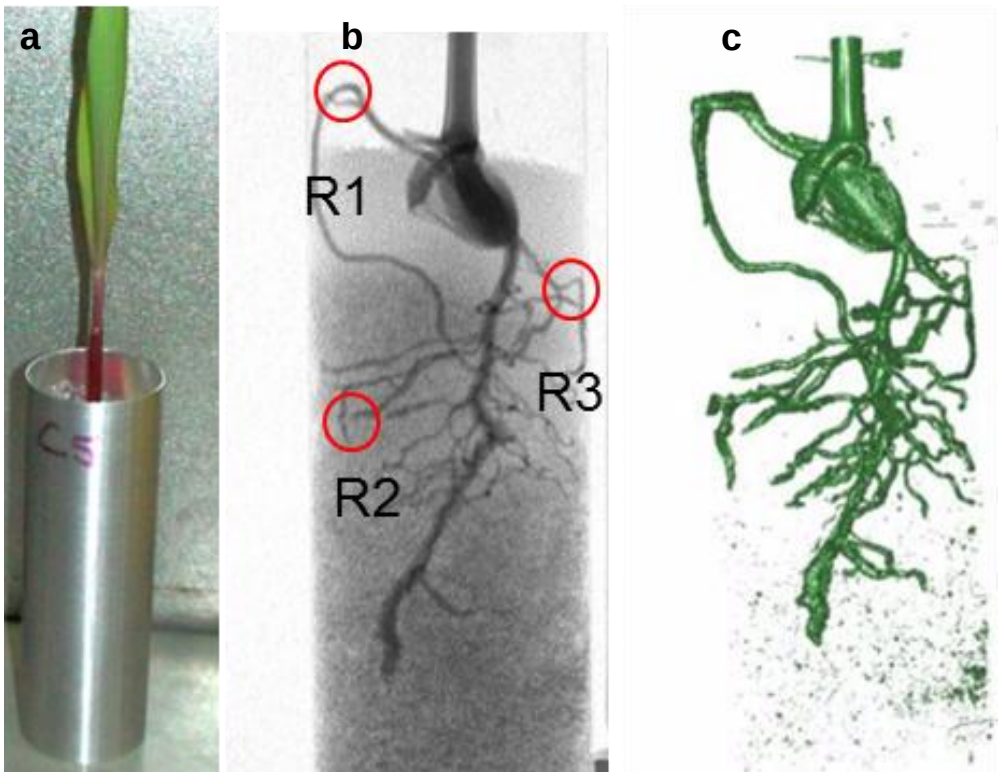

Figure A 3. 10-day old maize seedling growing in coarse sand: a) photograph of sample chamber; b) neutron radiograph at ~100 µm pixel resolution illustrating distribution of 0.2-1.6 mm roots. Three roots are highlighted (R1-R3) and referenced in Fig. A4, c) Corresponding image from the 3D tomographic reconstruction (reference Video S1), displayed from a slightly different aspect.

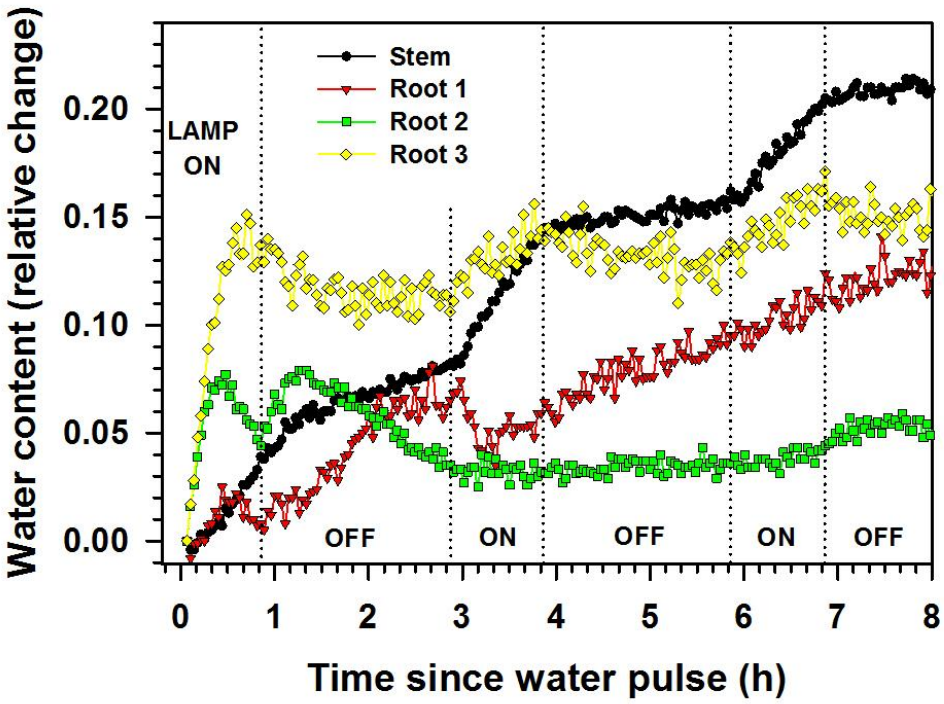

Figure A 4. Timing of water uptake for selected components of the 10-day old maize seedling illustrated in Fig. A3-b, illustrating the impact of changing solar radiation (LAMP ON or OFF) on rate of water flux in stem and ~0.5 mm roots following irrigation with 3 ml of D_2O. 2D radiographs of the system were linked together to visualize changes through time (Video S2). A positive relative change indicates D_2O influx and partial replacement of existing H_2O, as well as potential root swelling. A negative change indicates D_2O efflux or root shrinking.

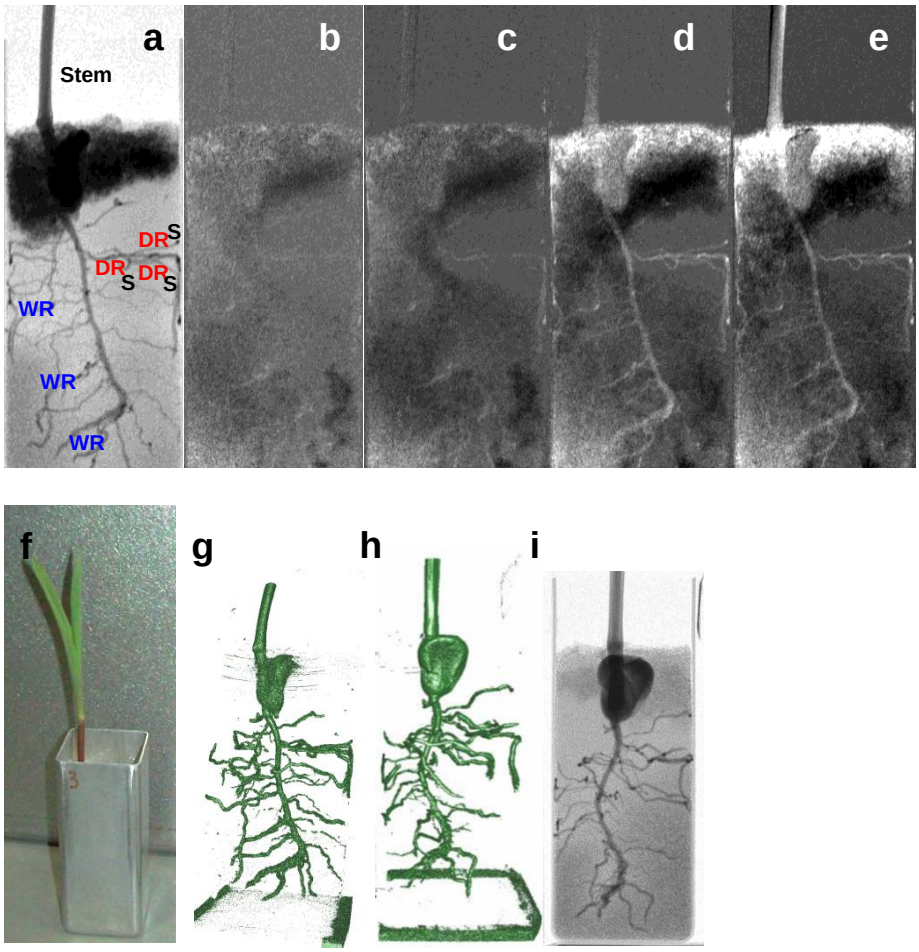

Figure A 5. In situ water uptake and transport in a 10-d old maize seedling. a) Initial neutron radiographic image prior to addition of 3 ml of D_2O to surface – dark areas represent existing H_2O within the soil and plant; b-e) the same system 0.25, 0.5, 6 or 12 h after surface irrigation with D_2O, divided by the initial image – light areas represent displacement of H_2O and uptake and transport of D_2O (reference Video S3); f) photograph of sample chamber; g-h) 3D tomographic reconstruction from two different angles, which confirmed identification of individual roots (reference Video S4); (i) One of the 360 2D neutron radiographs used for tomography.

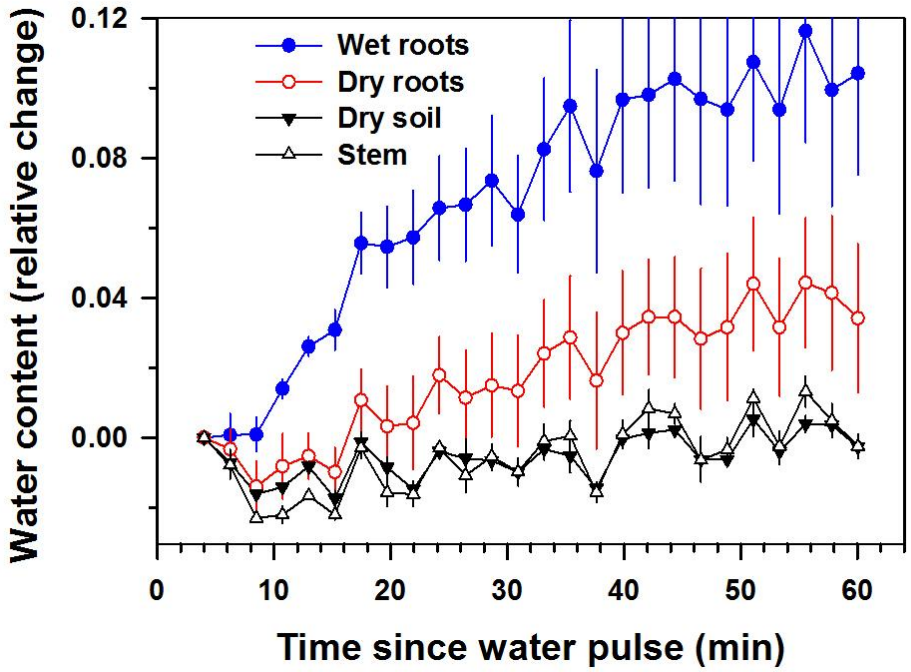

Figure A 6. Mean hydration of locations indicated in Figure A5-a with initial rapid root uptake from moist soil (WR), significantly greater than other locations (*****), followed by gradual rehydration of roots in dry soil (DR), whereas surrounding soil (S) and stem hydration remain unchanged.

VITA

Misun Kang was born and raised in South Korea. She attended the Korea University and received a Bachelors of Science degree in Chemistry in 1993. She then moved to United States with her husband and decided to pursue graduate study in the Department of Geology and Geophysics at Texas A&M University. She received her Master of Science degree in 2002. While at Texas A&M, she worked on quantification of organic carbon as well as geochemical modeling. She entered the PhD program in the department of Earth and Planetary Sciences at University of Tennessee, Knoxville, in 2010. While at UT, she conducted neutron imaging projects at Oak Ridge National Laboratory under the supervision of Drs. Ed Perfect and Hassina Bilheux. She will complete her PhD in Geology from the University of Tennessee in May 2013.